Metaconcrete: Engineered aggregates for enhanced dynamic performance

A Thesis by

Stephanie J. Mitchell

In Partial Fulfillment of the Requirements
for the Degree of

Doctor of Philosophy

For Mum, Dad, and Sarah

iv

Acknowledgments

I would like to thank my advisor, Professor Michael Ortiz, for all his help and guidance throughout my PhD. It has been a great honor to work with such an amazing scientist and engineer and I have thoroughly enjoyed our many conversations about research and life in general. I am so grateful to have had the opportunity to come to Caltech and his enthusiasm for science was a constant source of inspiration.

I would also like to thank Professor Anna Pandolfi, who has been my collaborator and mentor during my PhD. I am very privileged to have had the opportunity to work on this project with someone who has always offered generously their time and expertise whenever I am in need of advice. I truly appreciate the support she has given me and I have very much enjoyed getting to know her over the last few years.

To the other members of my committee, Professor Guruswami Ravichandran and Professor Dennis Kochmann, thank you for teaching me so much about solid mechanics and for providing me with feedback and advice throughout my PhD.

There many other people who have helped me over the last five years, and I would like to extend my warmest thanks for all of their support. To Lydia and Marta who keep everything running smoothly and who have always looked after me, thank you for all your help. To Petros for helping me sort out the more practical side of metaconcrete. Thank you for taking the time to talk with me. And my sincerest thanks to Jackie Gish for always being there to talk over lunch and offering me guidance whenever needed.

I would like to extend my sincerest thanks to Fulbright New Zealand, the North Harbour Club, Zonta International, and GALCIT, who have provided me with so much support over the course of my PhD through fellowships and enrichment programs, which I truly appreciate. I also wish to gratefully acknowledge the support provided by the Air Force Office of Scientific Research through the University Center of Excellence in High-Rate Deformation Physics of Heterogeneous Materials.

Finally, I wish to thank my family, the most important people in my life. To my lovely grandparents, Nana and Gromps, thank you for always being there with love and hugs when I get home. To my Mum and Dad, who are the most incredible parents and who are always there for me no matter when or where. I am so grateful for everything you have done for me. I remember having many long conversations a very long time ago about one day pursuing a PhD, and the unwavering encouragement you have always given me provided the confidence I needed to move across the world and follow my dream. I admire you both in every way. Thank you with all my heart. To Sarah, my amazing little sister, who is my best friend in the whole wide world. It has been so wonderful to explore California and study at Caltech together. Thank you for all your love, support, and for always being my wingwoman.

Abstract

This work presents the development and investigation of a new type of concrete for the attenuation of waves induced by dynamic excitation. Recent progress in the field of metamaterials science has led to a range of novel composites which display unusual properties when interacting with electromagnetic, acoustic, and elastic waves. A new structural metamaterial with enhanced properties for dynamic loading applications is presented, which is named *metaconcrete*. In this new composite material the standard stone and gravel aggregates of regular concrete are replaced with spherical engineered inclusions. Each metaconcrete aggregate has a layered structure, consisting of a heavy core and a thin compliant outer coating. This structure allows for resonance at or near the eigenfrequencies of the inclusions, and the aggregates can be tuned so that resonant oscillations will be activated by particular frequencies of an applied dynamic loading. The activation of resonance within the aggregates causes the overall system to exhibit negative effective mass, which leads to attenuation of the applied wave motion. To investigate the behavior of metaconcrete slabs under a variety of different loading conditions a finite element slab model containing a periodic array of aggregates is utilized. The frequency dependent nature of metaconcrete is investigated by considering the transmission of wave energy through a slab, which indicates the presence of large attenuation bands near the resonant frequencies of the aggregates. Applying a blast wave loading to both an elastic slab and a slab model that incorporates the fracture characteristics of the mortar matrix reveals that a significant portion of the supplied energy can be absorbed by aggregates which are activated by the chosen blast wave profile. The transfer of energy from the mortar matrix to the metaconcrete aggregates leads to a significant reduction in the maximum longitudinal stress, greatly improving the ability of the material to resist damage induced by a propagating shock wave. The various analyses presented in this work provide the theoretical and numerical background necessary for the informed design and development of metaconcrete aggregates for dynamic loading applications, such as blast shielding, impact protection, and seismic mitigation.

Contents

List of Figures

List of Tables

Nomenclature

$\bar{\omega}$	Forcing frequency (rad/s)
$\ddot{u}^j$	Acceleration of the j-th mass in a spring–mass chain
λ	Yield factor
$\mathbb{E}$	Energy
ν	Poisson's ratio
ω	Frequency (rad/s)
ω_0	Resonant frequency (rad/s)
ρ	Density
ρ_c	Density of coating material
ρ_l	Density of the aggregate lead core
ρ_m	Density of mortar material
ε	Regularization parameter for the eigenerosion scheme
ε^*	Eigendeformation field
A_γ	Wave amplitude of mass γ
b	Cross–sectional dimension of slab section
c_L	Longitudinal wave speed
d	Aggregate spacing
E	Elastic modulus
E_c	Elastic modulus of the aggregate coating material
f	Frequency (Hz)
$F(t)$	Blast force
f_a	Filling fraction

f_r Resonant frequency (Hz)

G_c Critical energy release rate

h Aggregate spacing

h Mesh size

h_{avg} Average mesh size

h_{min} Minimum mesh size

k Spring constant

L Length of slab section

m Mass in the one–dimensional spring–mass system

m_{eff} Effective mass

M_{tot} Total slab mass

$p(t)$ Blast pressure

q Wavenumber

q_{max} Maximum wavenumber

R_l Radius of the aggregate heavy core

T Transmission ratio

t Thickness of the aggregate compliant coating

u^j Displacement of mass j-th mass in a spring–mass chain

V_c Volume fraction of the aggregate coating material

v_c Volume of aggregate coating

V_l Volume fraction of the aggregate lead core

v_l Volume of lead core

V_m Volume fraction of mortar

v_m Volume of mortar

v_{tot} Total slab volume

Chapter 1

Introduction

Recently, the design and construction of artificial composite materials with unconventional properties has become an area of active research. These man-made structures can produce unique and desired behavior when they interact with an applied field or loading. One class of these composites is known as *metamaterials*, a term first introduced by Walser (2000) to emphasize their purpose as man-made, heterogeneous devices that display performance beyond the limitations of conventional composites.

Metamaterials research first began in the field of electromagnetics, where researchers were interested in the construction of devices and systems for controlling the propagation of electromagnetic waves and light. This has led to significant progress in developing electromagnetic metamaterials for negative refractive index applications, sub-wavelength imaging, and transformation optics. However, many of these concepts and techniques are not restricted to just electromagnetism and have counterparts in other areas of wave science. This has led to an explosion of research in metamaterial applications for other fields such as acoustics, elastodynamics, and thermodynamics.

Here, we apply the broad definition that a metamaterial is an artificial composite whose overall material properties are dependent on an engineered microstructure rather than solely the material properties of the constituents. Thus, these devices can display new responses that are precluded from traditional materials due to the physical constraints of their constituents. Such complex composites can be specifically designed to manipulate an applied wave or loading, resulting in unusual properties such as negative refractive index, negative shear modulus, or negative effective mass.

The unique properties that metamaterials display are often gained through the use of inclusions or structural features, engineered to interact with a particular type of wave motion. Often, this involves structures whose elements are arranged in a manner so that their size and spacing is smaller than the scale of spatial variation of the exciting field. These structures can also contain other unusual features, such as locally resonant behavior or active elements. Other composites and periodic media of interest include those with structural units of roughly the same size as the wavelength of the incident wave. Often termed photonic or phononic crystals, these materials use periodically spaced elements to create frequency bands of reduced wave transmission. These composites are closely linked to metamaterials, and the same structure may behave as one or the other depending on wavelength of the incident wave.

The structural features of metamaterials and composites can be designed in a multitude of ways to

control and create a number of desired behavior when interacting with electromagnetic, acoustic, elastic, and other incident waves. Therefore, there has been a significant amount of research into a variety of applications for these engineered materials. We begin by introducing the novel composites and metamaterials that fall into two broad categories, photonic crystals and electromagnetic metamaterials, which deal with the manipulation of electromagnetic waves, and mechanical metamaterials, which are designed for waves with lower input frequencies such as acoustic, elastic, or seismic loads. We then provide a brief assessment of other emerging fields in metamaterials science, such as thermodynamic and active metamaterials, and follow with an outline of the current research on blast shielding structures and impact protection. The theoretical and experimental work in these fields provides the background and motivation for the development of a new modified concrete with enhanced performance for dynamic loading applications.

1.1   Electromagnetic waves in metamaterials and composites

There has been a significant amount of research into the development of new artificial materials capable of exhibiting unusual properties when interacting with an electromagnetic field. The two most popular areas of interest are photonic crystals and electromagnetic metamaterials.

1.1.1   Photonic crystals

Photonic crystals are a class of artifical material that derive their properties from an internal structure that is of similar size to the wavelength of the applied wave (Andreone et al., 2011; Banerjee, 2011). They are also known as photonic or electromagnetic band gap structures. These crystals contain a periodic arrangement of macroscopic media with differing dielectric constants and, if absorption is minimal, reflection and refraction of light from the different interfaces can produce phenomena such as forbidden photonic bands. Photonic crystals can be specifically designed to induce these photonic band gaps, where light is prevented from propagating in certain directions with specified frequencies (Joannopoulos et al., 2008). In other words, photonic crystals can prevent the propagation of a specific range of wavelengths, or colors, of light. The band gap is considered 'complete' when it exists for any polarization and any angle of incidence of the light (Andreone et al., 2011).

The periodicity of the of the crystal plays an important role in the formation of the band gap. The width of the gap depends on the geometrical configuration and element spacing of the crystal, the geometry and size of the internal elements, and the dielectric constants of the crystal constituents. In general, a photonic band gap is more likely to occur in crystals where there is significant contrast in the dielectric constants of the constituent materials (Andreone et al., 2011).

The development of photonic crystals began when Yablonovitch (1987) and John (1987) proposed the use of artificial periodic structures to engineer electromagnetic modes at optical frequencies. Yablonovitch

suggested that these structures could alter radiation-matter interactions and therefore improve efficiency by controlling spontaneous emissions, which plays an important role in limiting the performance of optical devices such as semiconductor lasers, heterojunction bipolar transistors, and solar cells. John demonstrated the possibility of strong Anderson localization of light in three–dimensional disordered superlattices.
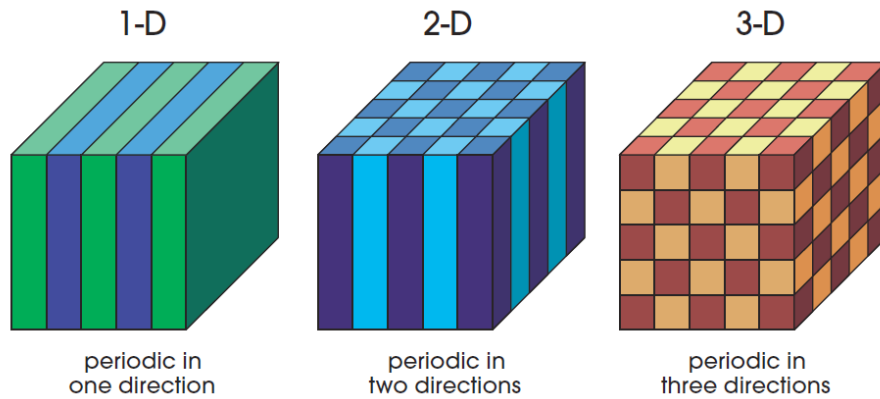
Figure 1.1: Examples of simple of one–, two–, and three–dimensional photonic crystals. Each color represents a material with a different dielectric constant (Joannopoulos et al., 2008).

Since then, there has been a significant amount of research activity in the development of photonic crystals, with a large number of experimental and theoretical investigations into crystals with both dielectric and metallic materials. Photonic crystals have been developed with periodicity in one–, two–, and three–dimensions, as shown in Figure 1.1. The number of axes of periodicity of the dielectric material is the defining feature of a photonic crystal.

One–dimensional photonic crystals contain alternating layers of dielectric material and can exhibit photonic band gaps, however only for specific angles of incidence in the direction of periodicity. Multilayer films have been used in dielectric mirrors and optical filters (Hecht, 2002), along with optoelectronic devices such as feedback lasers (Yeh, 2005).

Two–dimensional photonic crystals are periodic along two axes and homogeneous in the third, and may exhibit a photonic band gap in the plane of periodicity. An example of a two–dimensional photonic crystal is shown in Figure 1.2, where the structure consists of an array of long dielectric cylinders. Experimental and theoretical analyses of two–dimensional band gap systems include studies on different lattice structures, such as arrays of low–loss high–dielectric–constant cylinders (McCall et al., 1991), short dielectric cylinders including lattice defects (Smith et al., 1993), cylinders embedded in a background medium with a different dielectric constant (Plihal and Maradudin, 1991), and comparisons of square and hexagonal lattices of parallel rods (Villeneuve and Piché, 1992). Two–dimensional photonic crystals have also been shown to demonstrate negative refraction behavior. Luo et al. (2002) use a square lattice of air holes
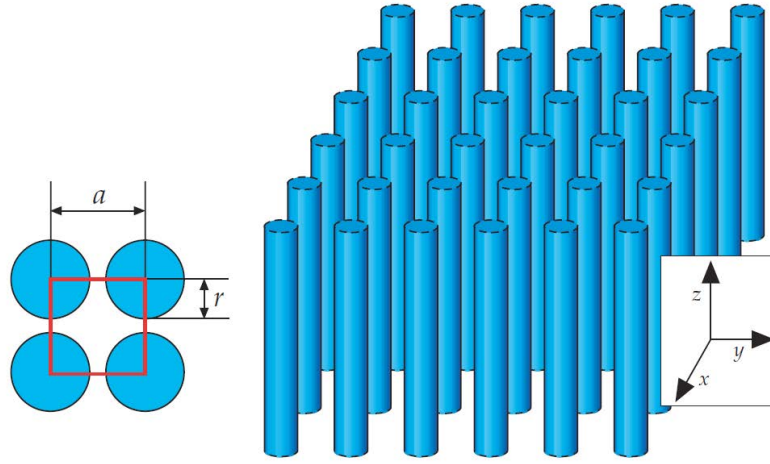
Figure 1.2: Example of a two–dimensional photonic crystal, consisting of a square lattice of dielectric rods of radius r. The material is homogeneous along the z direction and periodic in x and y, with lattice constant a (Joannopoulos et al., 2008).

to demonstrate an all-angle negative refraction effect and, similarly, Foteinopoulou et al. (2003) use an hexagonal lattice of dielectric rods to numerically investigate the wave behavior at an interface with a negative refractive index photonic crystal.
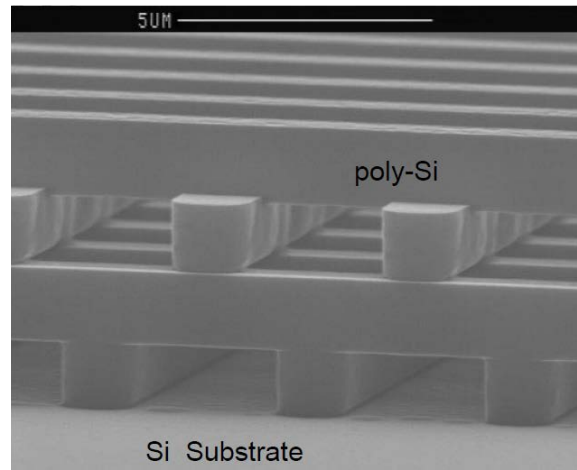
Figure 1.3: A three-dimensional woodpile photonic crystal tested at infrared wavelengths, consisting of rods made of polycrystalline silicon layered on a silicon substrate. The spacing between adjacent rods is $d = 4.2$ μm, rod width $w = 1.2$ μm, and the layer thickness is 1.6 μm. Scale bar 5 μm. Reprinted by permission from Macmillan Publishers Ltd: Nature (Lin et al., 1998), copyright (1998).

Three–dimensional crystals are the most complex of the photonic crystal configurations, being periodic along all three axes. They therefore exhibit a 'complete' photonic band gap, meaning that no propagating states are allowed in any direction within the crystal. Ho et al. (1990) proposed the first three–

dimensional structure that obtained a complete photonic band gap, which consisted of a diamond lattice of spheres. The first laboratory realization of a complete photonic band gap material was developed by Yablonovitch et al. (1991) and was constructed by drilling along the lattice vectors of a dielectric medium. Other three-dimensional photonic crystals include the woodpile crystal for infrared wavelengths (Ho et al., 1994; Sözüer and Dowling, 1994; Lin et al., 1998), an example of which is shown in Figure 1.3, along with inverse opal structures (Sözüer et al., 1992), and stacks of alternating two-dimensional crystals of rods and holes (Johnson and Joannopoulos, 2000).

Applications for photonic crystals include reflection type devices, such as reflectors, wave guides, microcavities, and emitters (Andreone et al., 2011; Joannopoulos et al., 2008). Another promising area is the use of all-dielectric negative refraction in superlenses for subwavelength imaging (Pendry, 2000; Joannopoulos et al., 2008; Luo et al., 2003).

1.1.2 Electromagnetic metamaterials

Electromagnetic metamaterials are another class of composite that utilize a designed internal struture. In photonic crystals, the properties of the composite are derived from diffraction effects and thus the lattice constant is of comparable size to the wavelength of the incident wave. By contrast, electromagnetic metamaterials utilize engineered internal structures that are much smaller than the wavelength. This enables the structure to be regarded as nearly homogeneous and therefore it is possible to describe the response of the composite by only the effective material parameters. In the case of visible light, this means structures that are nanometers in dimension, and for GHz radiation, such as microwaves, this results in structures as large as a few millimeters (Pendry, 2007).

The foundations of electromagnetic metamaterials lie with work conducted by Veselago (1968) on the electrodynamics of isotropic substances. Veselago stated that media with simultaneously negative values of dielectric constant and magnetic permeability could produce interesting phenomena. While at the time substances of this type did not yet exist, these materials could be imagined as possible composites of the future. It wasn't until much later that Pendry (2000) first took the principles outlined by Veselago and developed the initial theory for modern electromagnetic metamaterials, proposing the idea of superlenses with spatial resolution below that of the wavelength of light. Ordinary lenses are restricted by their diffraction limit, which means that the best resolution possible corresponds to about half of the incident wavelength of the light that is used to produce the image. However, by utilizing a medium with both negative permittivity and permeability, this new perfect lens material can have a negative refractive index, allowing imaging of objects only nanometers in size.

Negative refractive index electromagnetic metamaterials, termed 'left-handed' materials, were first realized experimentally by Smith et al. (2000). Simultaneously negative values of effective permeability and permittivity were created using a composite medium based on a periodic array of interspaced conducting nonmagnetic split ring resonators and continuous wires. The split ring resonator design used in the
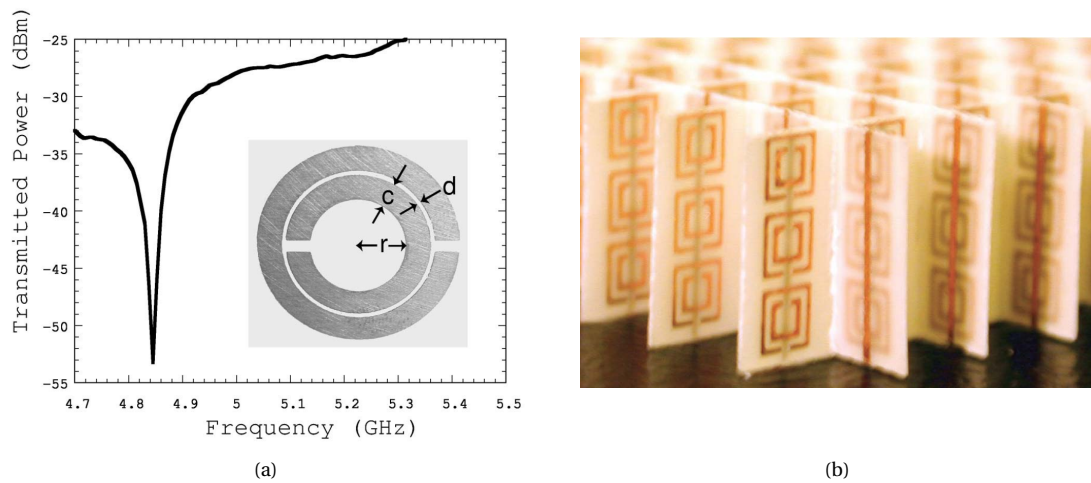
Figure 1.4: Split ring resonator electromagnetic metamaterials: (a) Resonance curve for the copper split ring resonator used in the experiments of Smith et al. (2000); $c = 0.8$ mm, $d = 0.2$ mm, and $r = 1.5$ mm. Reprinted figure with permission from Smith et al. (2000) Copyright (2000) by the American Physical Society, http://dx.doi.org/10.1103/PhysRevLett.84.4184. (b) Left-handed metamaterial consisting of square copper split ring resonators and copper wire strips on fiber glass circuit board material, which have been assembled into an interlocking lattice with a lattice constant of 5 mm. From (Shelby et al., 2001b). Reprinted with permission from AAAS.

experiment is shown in Figure 1.4(a). Split ring resonators, introduced by Pendry et al. (1999), are concentric cylinders with capacitive splits that respond resonantly to radiation applied so that the magnetic field is parallel to the axis of the ring. The splits in the rings enable the unit to be resonant at wavelengths much greater than the diameter of the rings, i.e., avoiding the half-wavelength requirement that would be the case if the rings were closed. The second split ring inside the first allows the unit to generate large capacitance in the small gap region between the ring, lowering the resonant frequency and concentrating the electric field.

A negative effective index of refraction for microwave frequencies was also demonstrated by Shelby et al. (2001b), and they present experimental data for a two–dimensional array of repeated unit cells of copper strips and split ring resonators, shown in Figure 1.4(b). Numerical simulations and analytical calculations for the same structure are presented in Shelby et al. (2001a). Control over the refractive index can also be used to create a new type of metamaterial lens using transformation optics for imaging applications. Kundtz and Smith (2010) use a varying refractive index to control ray trajectories, demonstrating a form of invisibility over a narrow wave band with gradient-index materials.

Another exciting area of research is electromagnetic cloaking. Electromagnetic metamaterials offer the ability to control both the permittivity and permeability, which may be designed to vary independently and arbitrarily throughout the material. This control allows for unusual material properties that can be exploited in applications such as cloaking and invisibility. A carefully designed metamaterial cloak can bend an electromagnetic field around an object, recombining the field lines back together so that they

emerge in the same direction as they entered. In terms of light, an observer would not see the difference between rays passing though the metamaterial medium or propagating in a uniform medium, so as a result, the object is invisible. Leonhardt (2006) presented a general design guide for the creation of perfect invisibility within the accuracy of geometrical optics using a dielectric metamaterial medium with man-made resonances. The paper also indicates that the same principles can be applied to cloaking devices for other electromagnetic waves or even sound. Simultaneously, an independent study by Pendry et al. (2006) proposed another design strategy for the redirection of electromagnetic fields, using an electromagnetic cloak to deflect the radiation. The authors demonstrate concealment of an object by cloaking a spherical volume in a metamaterial which guides the rays around the hidden object so that it remains untouched by external radiation, which leads to a perfect electromagnetic shield.

(a) (b)
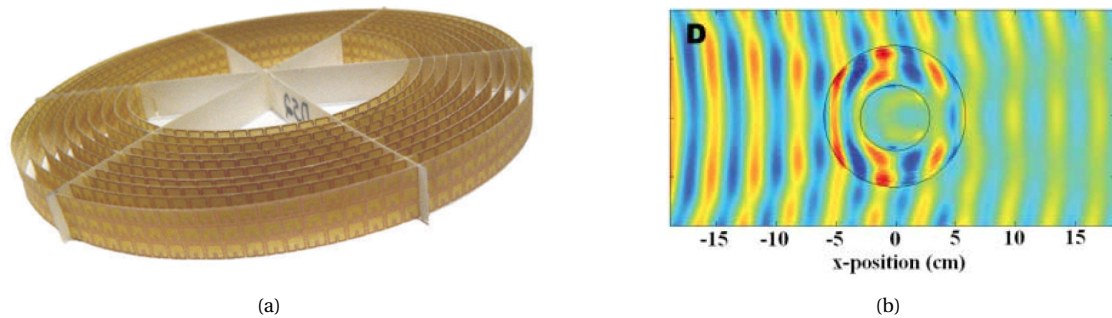
Figure 1.5: Metamaterial cloak for microwaves presented by Schurig et al. (2006): (a) two–dimensional structure consisting of 10 concentric cylinders of square split ring resonators. The cloak has an inner radius of 27.1 mm and an outer radius of 58.9mm. Each split ring resonator has a dimension of 10/3 mm; (b) experimental measurements showing a snapshot of the time-dependent, steady-state eletric field pattern. The cloak lies in the annular region between the two black circles and surrounds a conducting copper cylinder at the inner radius. From Schurig et al. (2006) and Cho (2006). Reprinted with permission from AAAS.

The first successful experimental implementation of an electromagnetic cloak was demonstrated by Schurig et al. (2006), where a two–dimensional cloaking structure consisting concentric shells of split–ring resonators was used to shield a small copper cylinder from a band of incoming microwaves. The structure of the cloaking metamaterial and the resulting steady-state electric field patterns are shown in Figure 1.5. More recently, Landy and Smith (2013) designed and experimentally tested a two–dimensional unidirectional microwave cloak capable of reducing the scattering of an object ten wavelengths in size. Microwaves have a relatively long wavelength, varying between a few millimeters and a little less than a meter. Visible light, however, has significantly smaller wavelengths and therefore cloaking of invisible light requires much smaller internal elements, on the order of nanometers, resulting in structures that are more difficult to fabricate (Soukoulis and Wegener, 2011; Wegener, 2013). Recent developments include the fabrication of a visible light carpet cloak which demonstrates wideband invisibility throughout the

visible spectrum with low loss (Gharghi et al., 2011).

1.2 Mechanical waves in metamaterials and composites

Recent developments in the field of elctromagnetic metamaterials has led to the exploration of other possible applications for metamaterials, such as acoustics and elastodynamics. Interest in these new applications has come from the realization that the concepts underlying the design of metamaterials for electromagnetic waves translate analogously to the design of elastic and acoustic metamaterials, which has led to a rapid increase in research activity. The full vector character of elastic waves, with different velocity of propagation for both the longitudinal and transverse components, provides a rich array of interesting problems for physicists and engineers.

Many of the challenges associated with the design and fabrication of electromagnetic metamaterials do not apply to elastic and acoustic metamaterials (Craster and Guenneau, 2013). For example, in optical metamaterials, to achieve strong contrast in optical properties generally requires the use of metals, which are accompanied by strong and undesirable dissipation or loss of energy. However, in acoustics and elastodynamics, the combination of strong contrast and weak energy dissipation is easily achieved. Fabrication of acoustic and elastic metamaterials can also be considerably easier than their optical counterparts. This opportunity for novel and exciting new materials in acoustics and elastodynamics has led to a burgeoning field in metamaterials science, and this section reviews the theory, numerical, and experimental work being conducted in this area.

1.2.1 Phononic crystals and acoustic metamaterials

Theoretical and experimental work on photonic crystals, discussed in Section 1.1.1, has shown the existence of frequency gaps for the propagation of electromagnetic waves. Phononic crystals are the acoustic equivalent of photonic crystals. Phononic crystals consist of a periodic array of elements with different elastic properties arranged so that the lattice constant of the structure is comparable in size to the wavelength of the incident wave. The interaction of the crystal with an acoustic wave causes the creation of band gaps or stop bands within the frequency spectrum, within which the applied wave cannot propagate and the incident energy is dispersed or scattered from the medium.

The band gaps observed in phononic crystals are caused by Bragg scattering and reflections within the structure. A full band gap is attained if the crystal is arranged so that band gaps overlap for all the directions of periodicity within the crystal, i.e., the band gaps are independent of the direction of propagation. This is caused by reflections on the surface of the scatterers or wave propagation within the scatterers (Miyashita, 2005). In this case, any incident wave is reflected completely from the structure, which results in the potential for many advantageous applications, such as for sound filters, transducers, wave-guides, acoustic imaging, and vibrationless environments (Kafesaki and Economou, 1999; Kushwaha et al., 1993).

The study of phononic crystals emerged in the early 1990's from investigations into the spectral gaps of periodic composites and the existence of localized waves in disordered systems. Studies on the spectral gaps of photonic crystals led to consideration of the band structure of materials interacting with acoustic and elastic waves. The investigation of acoustic and elastic wave propagation in composites consisting of spheres or cylinders embedded in a host material indicated that gaps could exist depending on the properties of the composite and its constituents (Sigalas and Economou, 1992, 1993; Economou and Sigalas, 1993; Sigalas et al., 1994; Economou and Sigalas, 1994; Kafesaki et al., 1995). The density and velocity contrast of the components of the composite, the volume fraction of each constituent, along with the lattice structure and topology all changed the band structure behavior of the material.

It was found that the use of different dielectric materials in photonic crystals could be equivalently applied through contrasting material constants in acoustic composites. The degree of contrast between the constituents led to different band structure behavior (Economou and Sigalas, 1993). For the case of three–dimensional fluid structures, the creation band gaps was easily induced using low velocity, low density inclusions in a high velocity, high density matrix. This, for example, is achieved in a system such as bubbles in a liquid. For the solid three-dimensional structures the optimal conditions for spectral gaps were obtained using low velocity, high density inclusions embedded in a high velocity, low density matrix. Economou and Sigalas (1994) proposed a composite of this type, using a silicon host containing a periodic array of gold or lead spheres with a volume fraction of about 10%.

Several theoretical methods were developed in order to study the elastic response of phononic crystals. The plane–wave expansion method is a popular approach that solves the wave equations in the Fourier space (Kushwaha et al., 1993; Sigalas and Economou, 1993; Kushwaha et al., 1994). However, phononic crystals containing elements with large contrast in their elastic properties are not easily treated with the plane–wave expansion method, because of the large number of plane waves required to obtain a reliable band structure. Other approaches can overcome these difficulties, and examples include the multiple scattering method (Kafesaki et al., 2000a; Kafesaki and Economou, 1999; Liu et al., 2000a) and finite-difference algorithms (Sigalas and García, 2000; Tanaka et al., 2000).

There are many potential arrangements and structures that can be created in a phononic crystal. Simple phononic crystals involving periodic arrays of cylinders have been shown to exhibit wave filtering behavior, utilizing spectral gaps to inhibit sound transmission. Mártinez-Sala et al. (1995) introduced an investigation into the sound attenuation achieved by a sculpture in Madrid, shown in Figure 1.6, where they measured transmission characteristics of the sculpture for sound wave vectors perpendicular to the vertical axis of the cylinders. They observed a sound attenuation peak at 1,670 Hz corresponding to the Bragg-type band gap predicted by theoretical calculations. This analysis was more formally presented by Sánchez-Pérez et al. (1998) with an experimental investigation of a two-dimensional periodic array of rigid stainless steel cylinders under lab conditions.

Another similar study was presented by Caballero et al. (1999), where they investigated the sonic band
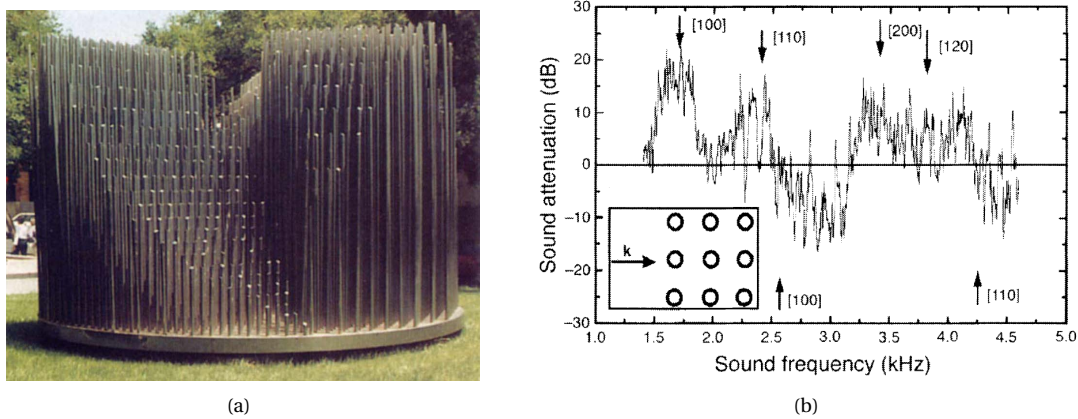
Figure 1.6: Phononic crystal in the form of a sculpture by artist Eusebio Sempere, located in Madrid; (a) The sculpture consists of a periodic array of hollow stainless steel cylinders. Each cylinder has a diameter of 2.9 cm arranged in a square lattice with a spacing of 10 cm. (b) Sound attenuation as a function of the sound frequency. The wave vector is along the (100) direction, as shown in the inset. Arrows on the figure indicate the calculated maxima and minima due to interference from different crystal planes of the sculpture. Reprinted by permission from Macmillan Publishers Ltd: Nature (Mártinez-Sala et al., 1995), copyright (1995).

gaps created by rigid cylinders in air, showing that wider gaps can be achieved by reducing the structure symmetry. The control of acoustic frequency gaps was also demonstrated theoretically by Goffaux and Vigneron (2001), where changes in geometry were shown to alter gaps in a system of parallel solid square-section columns distributed in a square lattice arrangement in air. Other interesting examples include an analysis of air bubbles in water presented by Kafesaki et al. (2000a) and fluids infiltrated in drilled solids for ultrasonic applications (Montero de Espinosa et al., 1998; Torres et al., 2001). Sonic crystals have also been developed for refractive acoustic devices used as interferometers or convergent lenses, which operate at wavelengths below the first acoustic gap. An example of of such a system was developed by Cervera et al. (2002) and is shown in Figure 1.7.

Phononic crystals containing both solid inclusions and a solid host have also been considered. Vasseur et al. (1998) experimentally investigated a square lattice of Duralumin cylindrical inclusions in an epoxy resin matrix, showing the existence of full band gaps. A further study by Vasseur et al. (2001) considered an array of steel cylinders in an epoxy matrix, thus using constitutent materials which have strong contrast in their densities and elastic constituents. The cylinders were arranged in a triangular lattice and demonstrated two absolute stop bands independent of the direction of propagation of the acoustic waves.

The existence of full or absolute band gaps in the transmission spectrum can be attributed two behavior, which must both be present in order for a full spectral gap to occur (Kafesaki and Economou, 1995; Kafesaki et al., 1995, 2000b; Klironomos and Economou, 1998). The first behavior is when the channel of propagation uses mainly the host material and avoids the inclusions, which causes a frequency gap when propagation is inhibited along the host material. The gap forms due to the presence of rigid inclusions,
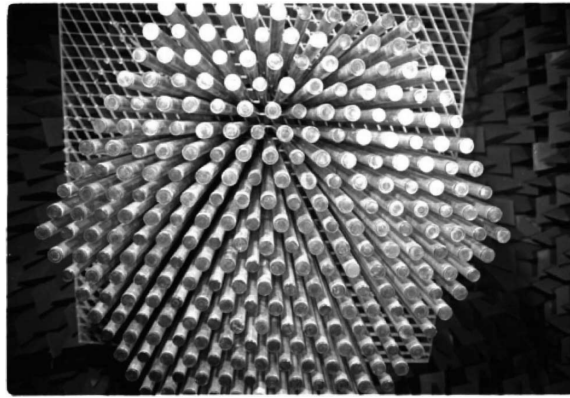
Figure 1.7: A sonic crystal sample, shown from underneath, consisting of 1 m long cylindrical aluminum rods hanging from a frame with a hexagonal pattern of lattice constant $a = 6.35$ cm. Experiments were performed with rods of $d = 1, 2, 3$, and 4 cm. Reprinted figure with permission from Cervera et al. (2002) Copyright (2002) by the American Physical Society, `http://dx.doi.org/10.1103/PhysRevLett.88.023902`

i.e., ones which do not allow the wave to enter its interior. The other channel employs resonance states, i.e., strong peaks in the scattering cross–section, which are created by coherent jumping from resonance state to neighboring resonance state equivalent to the linear combination of atomic orbitals in the electronic band structure. The combination of both of these phenomena leads to wide spectral gaps in the spectral regions between well-separated resonances, since in this gap neither channel is operational and consequently no propagation is expected to take place.

To further exploit the band gap behavior in phononic metamaterials consisting of cylinders embedded in a solid matrix, a new type of inclusion was considered, one in which there are localized resonances associated with each scattering unit. The use of these *locally resonant inclusions* can create new band structure behavior, allowing for spectral bands that are not dictated by the dimension of the lattice spacing. An analytical comparison of the band structure produced by arrays of solid Au cylinders and resonant Au cylinders layered with a thin rubber polymer was performed by Goffaux et al. (2002) and Goffaux and Sánchez-Dehesa (2003). They demonstrated that a complete band gap can be achieved in a frequency region two orders of magnitude lower than the one expected from considering only Bragg conditions. Similar studies include those by Hirsekorn (2004) and Wang et al. (2004a) on coated cylinders in an epoxy matrix, and that by Wang et al. (2004b) on the binary counterpart of locally resonant phononic crystals, where a locally resonant structure was created using purely rubber cylinders in an epoxy matrix. A review of the three–dimensional counterpart to these system is discussed in the following section.

1.2.1.1 Locally resonant sonic metamaterials

One subset of acoustic metamaterials is the class of composites known as *locally resonant sonic metamaterials*, introduced above. These structures combine some of the features of acoustic metamaterials and

phononic crystals with a new type of locally resonant inclusion. Locally resonant sonic materials contain inclusions with a layered structure, engineered to create band gaps or stop band at frequencies much lower than that achieved using a purely periodic material.

Phononic crystals make use of Bragg–type band gaps, where the periodicity of the structure induces vibration reduction within the material. However, inducing Bragg gaps in the low frequency range requires the internal structure to have a spatial period of similar size to the wavelength of the incoming wave. The wavelength of low frequency elastic waves in typical solids is relatively long in comparison to the dimensions of a typical acoustic shelter, thus making the use of Bragg gaps alone impractical for insulating acoustic waves.
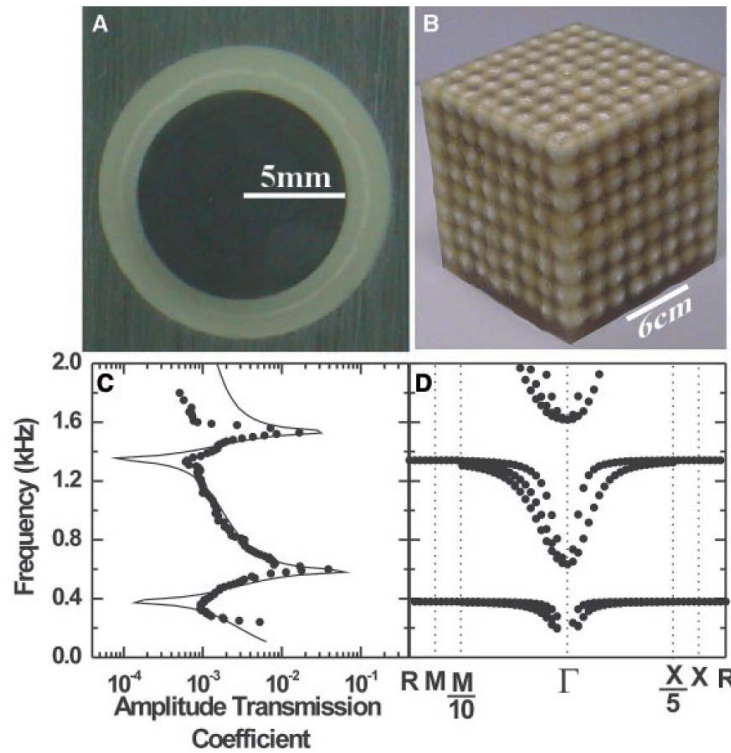
Figure 1.8: Locally resonant sonic crystal; (a) Cross section of a single inclusion, consisting of a lead sphere of radius 5 mm coated in a 2.5 mm layer of silicone rubber, embedded in an epoxy matrix. (b) 8×8×8 sonic crystal with a lattice constant of 1.55 cm tested with acoustic waves applied in the (100) direction with varying frequencies, producing the amplitude transmission plot shown in (c). The solid lines represent the calculated values and the circles represent the measured experimental values. (d) The calculated band structure for the sonic crystal, showing band gaps in the frequency spectrum. From Liu et al. (2000b). Reprinted with permission from AAAS.

To overcome this problem, Liu et al. (2000b) developed an array of locally resonant inclusions, consisting of silicone coated lead spheres in an epoxy matrix, shown in Figure 1.8. When a sonic wave passes through the material, resonance of the internal lead sphere can be activated at chosen frequencies, cre-

ating resonance induced band gaps two orders of magnitude lower than that obtained by the Bragg limit. Liu et al. (2002) demonstrated that the configuration of the band-gap can be tuned continuously from a resonance gap to a Bragg gap by varying the elastic properties of the inclusion components. A softer coating led to a resonance gap, whereas a stiff coating material created an elastic wave gap derived from Bragg scattering.

The wave attenuation behavior of locally resonant sonic materials is derived from the unusual material properties that these composites display, such as negative effective mass or negative bulk modulus. Liu et al. (2000b) demonstrated that disordered composites constructed with locally resonant inclusions display negative effective material properties, breaking the conventional mass-density law of sound transmission. Mass density is typically considered to be the volume average of the constituents . The implicit assumption in this expression is that the two components of the composite move in unison. However, in the case of resonant inclusions there is relative motion between the constituents and the matrix, meaning that the internal mass of the local resonator can move out of phase with the matrix displacement (Mei et al., 2006). If, in addition, the local resonators occupy a significant volume of the composite, then this results in a change in the overall mass density. Thus the effective mass density for the dynamic case is different from that in the static configuration (Banerjee, 2011; Mei et al., 2013). The effective mass density can also become negative in value when the core of the inclusion resonates, leading to interesting and unusual interactions with the applied wave motion. The concept of effective mass density has also been studied by Sheng et al. (2003, 2007), Liu et al. (2002, 2005), and Liu et al. (2011).

To further investigate the design of locally resonant metamaterials, Wang et al. (2006) studied longitudinal wave propagation in a quasi-one-dimensional slender beam with periodically attached harmonic oscillators. They computed the transmission frequency response function for the system and performed vibration experiments on a laboratory setup with an arrangement of masses and springs resembling the theoretical model, observing good correspondence between the two results. Wang et al. also found analytically that the beam to inclusion coating stiffness ratio highly influenced the attenuation properties within the observed transmission frequency band gap. Xiao et al. (2012) extended this work, modeling a uniform elastic rod containing a periodic array of multi-degree-of-freedom resonators, developing a methodology to predict the complex band structure resulting from these metamaterials. The inclusion of multi-degree-of-freedom resonators resulted in the presence of multiple band gaps, often achieving greater attenuation performance than in the single-degree-of-freedom case. Through a parametric study they were able to show that there exists coupling between both the Bragg-type and resonance-type gaps present in the response. This coupling behavior resulted in a great improvement in the bandwidth and attenuation performance of gaps around Bragg conditions, leading to super-wide band gaps useful in broadband vibration control applications.

There have been a number of recent efforts in the development of analytic modeling tools for metamaterials containing inclusions and other complex microstructures. Milton and Willis (2007) presented

a rigorous framework involving what they term the Willis equations, introducing a new point of view on the elastodynamic equations of composite materials. They consider the harmonic motion of a rigid body with hidden spring–mass systems, using a number of configurations to explain the concept of negative effective mass density in simple metamaterials with resonators. Using Newton's law for the motion of the included mass, they derive generalized equations of motion for the rigid body, where the effective mass (or p–mass) is a function of the oscillation frequency. Near the resonance frequency of the spring-mass system the p-mass assumes large values, becoming complex and eventually negative.

Zhu et al. (2011) used the same metamaterial proposed by Milton and Willis (2007) to develop a microstructure continuum model as an alternative to classic continuum theory. They derived field equations to represent elastic metamaterials with resonator microstructures, and used these in comparison with the finite element method to show accurate prediction of band gap features. Liu et al. (2012) took a similar approach, developing a multi-displacement microstructure continuum model to obtain the macroscopic governing equations for an anisotropic elastic metamaterial consisting of an epoxy matrix with lead cylinders coated with an elliptically shaped soft layer. Milton et al. (2006) and Milton (2007) also discussed metamaterials in the context of elastic cloaking devices, developing theory that may be useful for design of composites that can cloak objects from elastic waves of a given frequency.

1.2.1.2 One–dimensional model for negative–mass materials

The behavior of structures with locally resonant inclusions has been attributed to negative effective material properties, such as negative effective mass. As described above, the static and dynamic mass density are different when the composite material under dynamic excitation contains locally resonant inclusions.
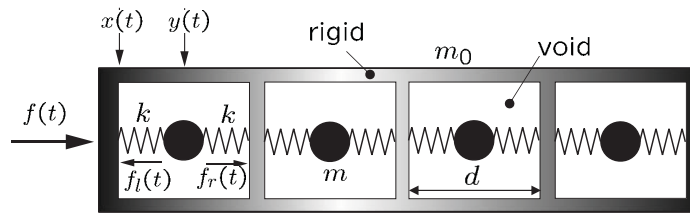
Figure 1.9: A one-dimensional material where the 'effective' mass depends on the frequency ω and can be negative (Milton and Willis, 2007).

The concept of negative effective mass is important in the design and analysis of metamaterials with locally resonant inclusions. To aid in the understanding of how these materials behave under an oscillating loading, we introduce the idea of negative mass by briefly recalling the elementary example described in Milton and Willis (2007). They consider a one-dimensional model consisting of n cylindrical cavities of length d, carved out from a bar of rigid material with mass m_0. In each cavity, a mass m is connected to

the walls through two springs of stiffness k, as illustrated in Figure 1.9.

The system oscillates harmonically in time with frequency ω under the action of the external force $f(t)$. The spring forces acting on the right and left side of each mass are denoted $f_r(t)$ and $f_l(t)$, respectively. All the forces vary in time according to

$$
\begin{aligned}
f(t) &= \mathrm{Re}(F\,e^{-i\omega t}), \\
f_r(t) &= \mathrm{Re}(F_r\,e^{-i\omega t}), \\
f_l(t) &= \mathrm{Re}(F_l\,e^{-i\omega t}),
\end{aligned}
$$

where capital symbols denote complex numbers. The position of the left wall and of the first mass are denoted by the coordinates $x(t)$ and $y(t)$, with

$$
x(t) = \mathrm{Re}(U_x\,e^{-i\omega t}), \qquad y(t) = \frac{d}{2} + \mathrm{Re}(U_y\,e^{-i\omega t}),
$$

where U_x and U_y are the complex displacements of the rigid system and of the mass, respectively. The velocities follow as

$$
v_x(t) = \mathrm{Re}(V_x\,e^{-i\omega t}), \qquad v_y(t) = \mathrm{Re}(V_y\,e^{-i\omega t}),
$$

with

$$
V_x = -i\omega U_x, \qquad V_y = -i\omega U_y.
$$

and accelerations are

$$
a_x(t) = \mathrm{Re}(A_x\,e^{-i\omega t}), \qquad a_y(t) = \mathrm{Re}(A_y\,e^{-i\omega t}),
$$

with

$$
A_x = -i\omega V_x = \omega^2 U_x, \qquad A_y = -i\omega V_y = \omega^2 U_y. \tag{1.1}
$$

The equation of motion of the rigid body is

$$
F - n(F_l - F_r) = m_0 A_x \tag{1.2}
$$

and the equation of motion for each mass m is

$$
F_l - F_r = m A_y. \tag{1.3}
$$

The forces of the springs can be expressed in terms of the displacement by using the Hooke's law

$$
F_l - F_r = 2k(U_y - U_x), \tag{1.4}
$$

leading to

$$2k(U_y - U_x) = 2k\frac{A_y - A_x}{\omega^2} = mA_y, \tag{1.5}$$

from where the expression of A_y can be derived

$$A_y = \frac{2k}{2k - m\omega^2}A_x. \tag{1.6}$$

By combining (1.2)-(1.3) and (1.6) we obtain

$$F = M(\omega)A_x, \qquad M(\omega) = m_0 + \frac{2k\,nm}{2k - m\omega^2}.$$

The mass M is called the effective momentum mass or p-mass. The p-mass reduces to the rigid body mass m_0 for vanishing spring stiffness, and to the sum of the masses $m_0 + nm$ in absence of motion. If we introduce the natural frequency of one of the mass-spring cores as

$$\omega_\rho = \sqrt{\frac{2k}{m}} \tag{1.7}$$

we can write the p-mass as

$$M(\omega) = m_0\left(1 + \alpha\frac{\omega_\rho^2}{\omega_\rho^2 - \omega^2}\right), \qquad \alpha = \frac{nm}{m_0}. \tag{1.8}$$
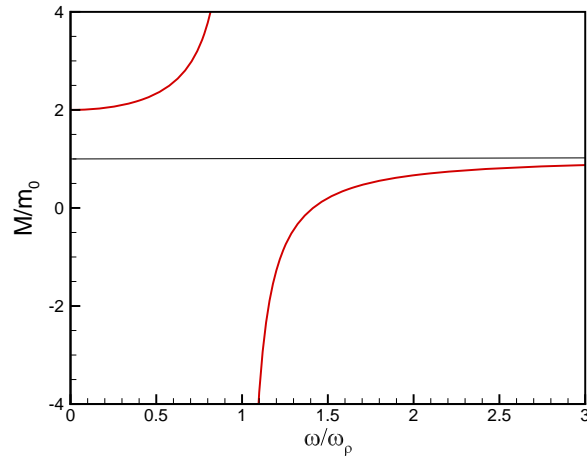
Figure 1.10: Variation of the p-mass value with the excitation frequency of the model described in Milton and Willis (2007).

The p-mass can become very large and complex near the resonant frequency, achieving negative values for $\omega > \omega_\rho$, as seen in Figure 1.10. Thus the effective mass is a function of the oscillation frequency, and it is this behavior near the resonant value of the internal system that causes the change in global material properties, leading to the new and novel materials with the ability to reduce the effect of an applied

wave.

Similar models consisting of one–dimensional spring–mass chains have also been used to model the band gap and transmission behavior in acoustic and elastic metamaterials, where the band gap results from the occurrence of negative effective mass. Jensen (2003) used a one–dimensional array of masses and springs to model a periodic lattice structure, investigating the structural response and band gap behavior. The model showed that the one–dimensional filter was insensitive to both damping and small imperfections within the system. With the development of locally resonant sonic metamaterials, one–dimensional mass-spring chains have also been used to derive the dispersion relation for systems containing mass–in–mass resonating units. (Huang et al., 2009) and (Huang and Sun, 2009) compute the dispersion curves for such a system, demonstrating the formation of band gaps and relating this to resonant behavior. They also link this behavior to the effective mass of the periodic unit, showing that modeling the system in this way leads to negative effective mass at freqeuncies just above the resonance value. Similarly, Yao et al. (2008) used a one–dimensional system with effective mass to compute band gap behavior and wave transmission, finding close correspondence between the numerical and experimental results.

1.2.2 Other mechanical metamaterials

Many of the systems used in phononic crystals and acoustic metamaterials are also applicable to other mechanical waves. The control of elastic wave trajectories in thin plates is one interesting area being explored. Farhat et al. (2009) proposed a design for a cloak to control bending waves propagating in isotropic heterogeneous thin plates. This was followed with further analysis in Farhat et al. (2012), where it was shown that a heterogeneous orthotropic cloak can be designed using a radially symmetric multilayered structure. An object surrounded by such a cloak can appear neutral for flexural waves, due to a set of periodic perforations, or air holes, in the plate. This theoretical and numerical work was then experimentally tested by Stenger et al. (2012), using a cloak consisting of 20 concentric rings of 16 different metamaterials to show that cloaking behavior can be successfully achieved in thin plates at low frequencies. A similar experimental study on flat lens focusing of elastic waves in plates was performed by Dubois et al. (2013), using an array of circular air holes in a thin plate to achieve large–angle negative refraction.

The studies on elastic waves in thin plates naturally suggest potential useful applications in vibration isolating structures in the aeronautical, automotive, and ship industries, along with larger scale applications such as earthquake resistant infrastructures and anti-earthquake passive systems (Farhat et al., 2009). Work in the seismic application of these systems has recently been presented by Brûlé et al. (2014), where civil engineers explored the potential of using metamaterials with seismic surface waves. They present the results of a large scale experiment, shown in Figure 1.11, where a grid of holes was bored 5 m deep into clay soil and the system tested using a vibrating probe to simulate an earthquake. Measurements showed a modification of the seismic energy distribution in the presence of the metamaterial, displaying shielding of surface elastic waves at around 50 Hz, and the results were in agreement with those

(a)   (b)
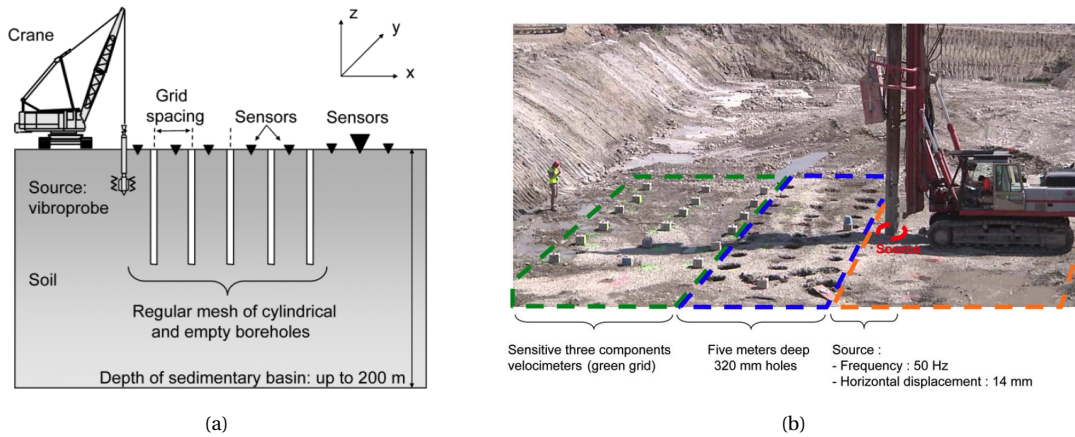
Figure 1.11: Seimic metamaterial experiment by the Ménard company: (a) cross section of the seismic testing device in the x-z plane, and (b) photograph of the experiment showing the location of the sensors (green dashed line), the 5 m deep self-stable holes of diameter 0.32 m with center–to–center spacing of 1.73 m making up the seismic metamaterial (blue dashed line), and the rotating source, which is a vibrating probe set on a crane generating an elastic wave of frequency 50 Hz (red dashed line). Reprinted from Brûlé et al. (2014), http://dx.doi.org/10.1103/PhysRevLett.112.133901.

from numerical simulations using an approximate plate model. A system of this type could be useful for the protection of buildings from earthquake shaking and the authors suggest that this is only the starting point for these applications, with much further investigation needed.

Figure 1.12: Structured cloak for surface waves in fluids, consisting of 100 rigid sectors evenly machined in a metallic ring of inner diameter 82 mm and outer diameter 200 mm. Reprinted figure with permission from Farhat et al. (2008) Copyright (2008) by the American Physical Society, http://dx.doi.org/10.1103/PhysRevLett.101.134501.

Another idea being explored is the use of cloaking devices for surface waves in fluids. Farhat et al. (2008) built a prototype for a cloak of this type consisting of concentric rings of metallic rods, creating a

structure ranging from 82 mm to 200 mm in diameter, shown in Figure 1.12. This structure was tested in a wave tank with a closely located acoustic source and was observed to bend surface waves over a finite interval of frequencies. These devices could eventually be developed on a larger scale and used for hiding vulnerable coastlines and protecting offshore platforms from ocean waves such as tsunamis.

1.3 Further applications for metamaterials

Metamaterials have also been considered for a number of other applications, some of which will be briefly summarized here.

One interesting field being considered is the use of metamaterials in thermodynamics. In the design of optical metamaterials, much of the focus is on molding of the flow of energy flux per unit time and area, i.e., the Poynting vector. The heat current density in thermodynamics has the same meaning and units and follows a related continuity equation to that in optical design, even though in thermodynamics waves do not occur. A thermodynamic cloak could be made using the principles of metamaterial design conidered in optics, thus protecting objects from overheating while keeping the heat flow in their surroundings as though nothing is there (Guenneau et al., 2012; Schittny et al., 2013). Further, active thermodynamic metamaterials could provide exterior thermal cloaking to objects, i.e., where the object is spatially separated from the cloak. This could be achieved using metamaterials to create negative heat conductivities, reversing the flow of heat so that it moves from cold to hot (Wegener, 2013).

Active metamaterials have already been demonstrated using embedded active circuits and devices, such as the zero loss structures tested by Yuan et al. (2009) and the self-tuning metamaterials presented by Barrett and Cummer (2014). Likewise, active metamaterials could be considered for mechanical metamaterials, integrating miniature energy sources together with sensors, actuators, and feedback loops into the individual unit cells (Wegener, 2013). An acoustic metamaterial with active elements was recently demonstrated by Popa and Cummer (2014), and a model for an active elastodynamic cloak was presented by Norris and Amirkulova (2014) based on the active acoustic cloaking theory of Norris et al. (2012).

We have provided a description of the theory, design, numerical and experimental testing of metamaterials for a variety of applications in electromagnetics, mechanics, and fields beyond classical waves. This summary provides the background and motivation for the design and analysis of a new concrete metamaterial, discussed in detail in the following chapters.

1.4 Blast and impact protection structures

The protection of buildings and structures from terrorist or accidental explosions is becoming an increasingly important consideration for many government, military, and even civilian facilities (Krauthammer, 2008). Explosive events generate a high-pressure dynamic loading on a structure, and for many this load-

ing goes well beyond the conventional lateral earthquake and wind loads that the building system is designed to resist. The detonation of an explosive device generates an overpressure wave which radiates out from the source of the detonation, and when this reaches the structure it results in a dynamically applied pressure load. Without proper design and consideration of the effects of this loading, the structure and the occupants can be at risk from failure of the exterior of the structure, high-velocity debris, and high-pressure demands entering the interior of the building or structure.

There have been a number of structural systems developed for the protection of structures and sensitive facilities. These range from simple techniques, such as the use of interior rubber membrane coatings and exterior soil embankments, to more sophisticated systems such fiber–reinforced composites and layered wall panels for the retrofit of at–risk structures. Naito et al. (2011) describe the design and testing of a precast concrete panel system for the retrofit of facilities with exterior light gauge metal stud walls. These conventional wall systems provide many benefits in terms of fire and weather resistance; however, their low weight and weak floor connections result in poor performance when subjected to a blast loading. The use of precast concrete wall panels can provide additional protection, with their large mass and high inertial resistance making them ideal for resisting a dynamic blast event. A series of precast panels was installed exterior to the test building envelope, with measurements from a blast test showing that the precast wall system can provide effective protection, with only minor cracking and no permanent deformation on the interior wall.

Fiber reinforcement has also been used to protect structural beams, columns, slabs, and walls. Malvar et al. (2007) review some of the techniques proposed, such as fiber–reinforced jackets for columns and beams, near-surface mounted rods, and fiber reinforced expoxies or polyurea layered on masonry walls. These systems provide additional strength to critical structural elements and can also allow for the containment of fragments ejected from the structural material during a blast event.

Fibers can also be mixed into the concrete itself, forming what is termed 'fiber reinforced concrete'. Garfield et al. (2011) test a number of different concrete panel configurations containing macro-synthetic fibers dispersed through the concrete matrix. Fiber reinforced concrete panels containing steel bar reinforcement provided the best performance when experimentally tested with a blast loading, exhibiting significantly less damage when compared to standard concrete panels. Similar numerical studies were conducted by Pantelides et al. (2014) on fiber reinforced panels with normal weight concrete and Mao et al. (2014) on fiber reinforced panels using high strength concrete.

Other designs combine these techniques, using layered panels to reduce the effect of blast loading. Christian and Chye (2014) propose a steel-concrete composite panel consisting of fiber-reinforced high-strength concrete on the incident face combined with a steel sandwich inner layer. The inner layer of the composite panel is designed to dissipate energy from the imparted blast wave. This panel design displayed good performance and high energy absorption in numerical simulations when tested with a blast charge.

For a general review of the history of blast protective structures, explosive devices, design procedures, and recommendations for blast fortifications, see Krauthammer (2008).

1.5   A new concept for an engineered concrete

Research on engineered composites designed for interaction with electromagnetic, acoustic, and elastic waves has led to a new suite of materials that can develop unusual properties. As the field of metamaterials science has grown, the creation of new devices and structures in one field of wave science has led scientists and engineers to consider its benefits in other areas. For example, the use of designed structures in electromagnetics led to new devices in acoustics and elastodynamics. One structural material with the potential for enhanced properties through the use of a designed microstructure is concrete, a composite used for myriad of structural applications. Influenced by the development of locally resonant inclusions in acoustic and elastic metamaterials, we investigate a new type of concrete that contains resonant 'aggregates' to modify the effect of an applied dynamic loading. We name this particular composite *metaconcrete*.

Metaconcrete utilizes the concept of negative effective mass, which has been shown to successfully attenuate acoustic waves in locally resonant sonic crystals, discussed previously in Sections 1.2.1.1 and 1.2.1.2. This new composite material employs bi-material spherical inclusions as a replacement for the standard stone and gravel aggregates of regular concrete. Metaconcrete aggregates contain a heavy metal core and are coated with a thin compliant outer layer, a few millimeters in thickness. Layering a softer coating between two relatively stiff materials allows for relative motion, and thus resonance, within the aggregate. Under the action of particular frequencies, the aggregates display resonant behavior by oscillating about their equilibrium configuration and consequently trapping a portion of the supplied mechanical energy of the system.

Resonant aggregates characterize metaconcrete with a wide range of natural frequencies not observed in regular concrete. We investigate the dynamic behavior of metaconcrete by considering a number of different loading profiles applied to a slab of material with an internal structure containing a periodic array of metaconcrete aggregates. By adjusting the geometry and coating stiffness we can modify the resonant behavior of the aggregate so that it occurs within a desired frequency range.

Meataconcrete aggregates can therefore be easily tuned to a chosen dynamic loading by simply adjusting the properties of the coating and core layers, and this provides the opportunity for the material to be engineered for a variety of applications. A metamaterial system utilizing locally resonant inclusions could be used in a panel structure or protective slabs for blast shielding, acting as an absorbing layer to remove some of the energy from a propagating shock wave caused by an explosion. Metaconcrete could be used as an alternative to or in conjunction with the structural protection devices described in Section 1.4, for example, as a metamaterial layer to absorb shock energy in wall panels or as a protective barrier slab

for retrofit applications. Other possible applications include impact protection, vibration absorption, and tuned damping foundations to mitigate seismic actions in buildings.

1.6   Outline of contents

The thesis builds on the general concepts and theory of engineered materials introduced in this chapter, which provide the motivation and background for the development of metaconcrete. Chapter 2 begins by detailing the design and structure of a metaconcrete aggregate, providing the geometrical and material parameters considered in all the numerical analyses. An analysis of resonant behavior and aggregate natural frequencies is presented for both a simplified one–dimensional model and a more detailed three-dimensional aggregate model. A slab design for the computations is then presented, along with details of the finite element models used in the study.

We begin the numerical analyses in Chapter 3 by considering the effect of resonant behavior on the performance of the slab. We first consider a simple one–dimensional model to generate dispersion plots, indicating band gap frequency ranges where attenuation of the propagating wave can be achieved. We then consider the transmission of wave energy through a three–dimensional metaconcrete slab model. The method for computing the transmission ratio from a finite element slab model is presented along with results from four aggregate configurations, showing the change in behavior as the frequency of the applied sinusoidal displacement reaches the resonant value of the aggregates.

In Chapter 4 we examine numerically the behavior of metaconcrete slabs under the action of a blast wave profile caused by the ignition of an explosive. We investigate a range of different aggregate geometry and material configurations to identify how changes in resonant frequency effect slab behavior. The consideration of transmitted mechanical energy and maximum mortar stress provide some design indications for the tuning of the aggregate structure for particular dynamic loadings.

An analysis of the fracture behavior of metaconcrete follows in Chapter 5, where we extend the elastic analyses of the previous chapter to include fracture and damage of the mortar material. Brittle fracture is incorporated through the use of an eigenerosion scheme, which erodes elements satisfying an energy–based fracture criterion. The effect of different fracture parameters on the performance of the slab is investigated through parametric studies, looking at the change in slab behavior due to various aggregate material and geometry configurations. We examine slab stress distribution, fracture surfaces, and energy transmission to identify the best aggregate configuration for enhanced slab performance.

Finally, a summary of the most important results from the study is given in Chapter 6, along with concluding remarks and an outline of future avenues for investigation.

Chapter 2

Modeling metaconcrete

A new type of structural concrete for dynamic loading applications was introduced in Chapter 1, which we have called *metaconcrete*. To investigate this new material we conduct a numerical study of its behavior under a variety of conditions, including harmonic displacement loading, blast loading, and in the presence of brittle fracture. We begin by detailing the design and configuration of the metaconcrete aggregates, the spherical layered inclusions that provide metaconcrete with unusual global properties. This chapter provides a description of the geometry and materials chosen for the aggregates, the calculation of the eigenfrequencies for each aggregate configuration, and the finite element models used in the analyses.

2.1   Metaconcrete aggregates and their properties

Metaconcrete aggregates consist of a layered structure designed to allow for resonance and absorption of wave energy. We use a similar structure to the locally resonant inclusions utilized by Liu et al. (2000b) in the design of sonic crystals for the attenuation of acoustic waves. These inclusions were shown to resonate at certain frequencies, creating a negative effective dynamic mass density which has been linked to the reduction in wave transmission observed in theoretical and experimental studies.

Standard concrete consists of a graded assortment of gravel, crushed stone, and sand aggregates mixed into a paste made from cement and water (McMillan and Tuthill, 1973; Mehta, 1986). The cement paste acts as a binding medium, taking up approximately one–quarter of the total volume, and the aggregates act as a relatively inert filler material, occupying roughly three–quarters of the concrete volume (Troxell et al., 1956). The proportions of these principal constituents can be changed to create concrete with different properties, such as high–strength or lightweight concrete. The aggregates serve a number of functions; they provide a relatively cheap filler for the cementing material, they reduce volume changes resulting from the hardening process and moisture changes, and they provide a mass of particles to resist the action of applied loads, abrasion, and weather (Troxell et al., 1956). The material character of the aggregate particles effects the workability of the fresh mix along with the strength and durability of the hardened material.

To design a concrete composite with the ability to attenuate dynamic loading, we replace the traditional stone and gravel aggregates of standard concrete with an engineered aggregate. These new ag-

gregates produce local resonances within the material and provide metaconcrete with a range of natural frequencies not found in typical concrete. Standard coarse concrete gravel and stone aggregates have a maximum size of around 10-38 mm (American Concrete Institute, 2007). We therefore design our aggregates so that they have an outer diameter of 24 mm and mix them into a cement paste that will form the outer matrix material. The properties of the metaconcrete aggregates will be discussed in this section, providing an outline of how to tune the aggregates for different resonant behavior.

2.1.1 Aggregate structure and materials

Metaconcrete aggregates contain two components which interact to cause resonance. Each aggregate contains a heavy metal core coated in a more compliant outer material, a few millimeters in thickness, as shown in Figure 2.1. The aggregates are suspended in a mortar matrix, that for numerical purposes we assume is homogeneous in nature. It is possible that for certain applications a thin protective metal or plastic casing may be required to maintain the integrity of the aggregate when cast in large sections or to prevent any seepage into the coating material.
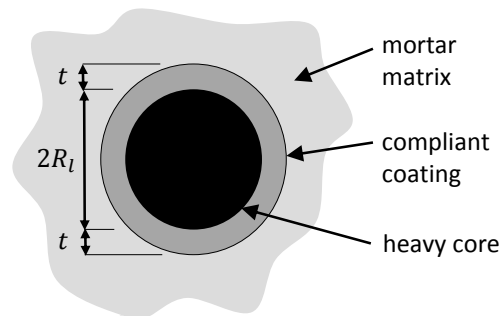
Figure 2.1: Structure of a metaconcrete aggregate with lead core radius R_l and coating thickness t.

Table 2.1 lists the materials considered in the numerical analyses. The table displays properties for the mortar matrix along with the aggregate core and coating materials, listing the density ρ, elastic modulus E, and poisson's ratio v. In our numerical analyses, lead is used for the aggregate core material. Lead has a very high density and therefore creates a drastic mass contrast between the core and outer layer of the aggregate. This mass contrast combined with the large difference in stiffness between the coating layer, the surrounding matrix, and the core material helps to create the out of phase behavior required for resonance within the aggregate at the frequencies typical of elastic waves.

To investigate a range of coating materials, we consider five different aggregate coatings with elastic moduli ranging between 1 MPa and 10 GPa, as listed in Table 2.1. Choosing coatings that encompass a range of elastic moduli allows us to assess the effect of coating stiffness on slab performance. Moreover, we study three different aggregate geometry configurations, presented in Table 2.2, where R_l represents

Table 2.1: Material constants used in the simulations.

Material	ρ (kg/m^3)	E (GPa)	ν
Mortar	2,500	30	0.20
Lead	11,400	16	0.44
Silicone	1,100	0.001	0.47
Natural rubber	900	0.01	0.49
Low density polyethylene (LDPE)	1,100	0.1	0.45
Nylon	1,150	1.0	0.40
Urea formaldehyde (UF)	1,500	10	0.40

the radius of the lead core and t is the thickness of the coating layer. Changing the thickness of the coating and lead core radii allows us to consider the effect of geometry changes on the performance of the aggregate, since we can generate different natural frequencies and behavior for each configuration. The outer diameter of the aggregate remains at 24 mm for all three cases, and the coating thickness varies between 1 mm and 3 mm.

Table 2.2: Aggregate geometry data.

Configuration	R_l (mm)	t (mm)	$R_l\, t$ (mm)
A	11	1	11
B	10	2	20
C	9	3	27

2.1.2 Aggregate resonant frequency

Metaconcrete aggregates are structured so that local resonances may occur when a slab of metaconcrete material is under the action of a dynamic loading. Resonance of the heavy core is the key aggregate feature influencing slab behavior. The aggregate configurations listed in Section 2.1.1 each produce a different resonant frequency. Therefore, in order to compare each configuration, we derive the resonant frequencies using two methods. First, we develop general tuning equations based on a simple one–dimensional spring–mass system. We then use a three–dimensional metaconcrete unit cell to compute a more detailed picture of the modal frequencies using finite element analysis.

2.1.2.1 One–dimensional model for resonant frequency

With the help of a mass-spring system equivalent to the resonant aggregate, we derive a simple relationship for the main geometry and stiffness parameters of the aggregate, accounting for the movement of the central core through the softer outer material. This relation can be used to define the range of resonant frequencies for an ideal metaconcrete.

Let us consider a single inclusion, where we choose a heavy core consisting of lead with a radius R_l and a soft material coating of thickness t. The density of lead is denoted ρ_l, and the total mass of the heavy core is

$$m = \rho_l \frac{4}{3} \pi R_l^3. \tag{2.1}$$

The stiffness of the surrounding soft material can be assumed, on each side, to be equivalent to a spring of constant k

$$k = \frac{E_c A}{t}, \tag{2.2}$$

where $A = \pi R_l^2$ is proportional to the lead core maximum section area, i.e., the portion of soft material resisting the motion of the core, and E_c is the elastic modulus of the coating material.
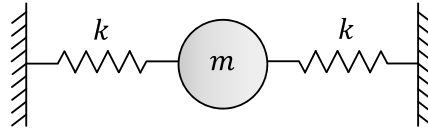
Figure 2.2: One–dimensional spring–mass system, with heavy mass m and spring constant k.

The resonant frequency of a one-dimensional system of mass m and with two equivalent springs of stiffness k, shown in Figure 2.2, is therefore given by

$$\omega^2 = \frac{2k}{m} \tag{2.3}$$

Combining Eqs. (2.1)-(2.3) gives the following relation for the aggregate resonant frequency,

$$\omega^2 = \frac{3}{2} \frac{E_c}{R_l \, t \, \rho_l}, \tag{2.4}$$

or expressed in units of Hertz,

$$f = \frac{1}{2\pi} \sqrt{\frac{3}{2} \frac{E_c}{R_l \, t \, \rho_l}}. \tag{2.5}$$

Table 2.3: Aggregate resonant frequency, in kHz, for each geometry and material configuration.

	Silicone	Natural Rubber	LDPE	Nylon	Urea formaldehyde
A	0.55	1.74	5.50	17.41	55.04
B	0.41	1.29	4.08	12.91	40.82
C	0.35	1.11	3.51	11.11	35.13

Using the material data from Table 2.1 along with the geometry data from Table 2.2, we can therefore compute the approximate resonant frequencies for each aggregate configuration. Table 2.3 lists the nat-

ural frequency, computed using Eq. (2.5), for every aggregate material and geometry arrangement under consideration in the numerical analyses. The same data is plotted in Figure 2.3, where we observe that decreasing the coating thickness and increasing the coating elastic modulus will increase the value of the aggregate resonant frequency. Using the chosen configurations, we cover frequencies between 0.35 kHz and 55.04 kHz in the analyses. We therefore consider aggregates with a wide range of frequencies, encompassing those typical of fast dynamical actions.
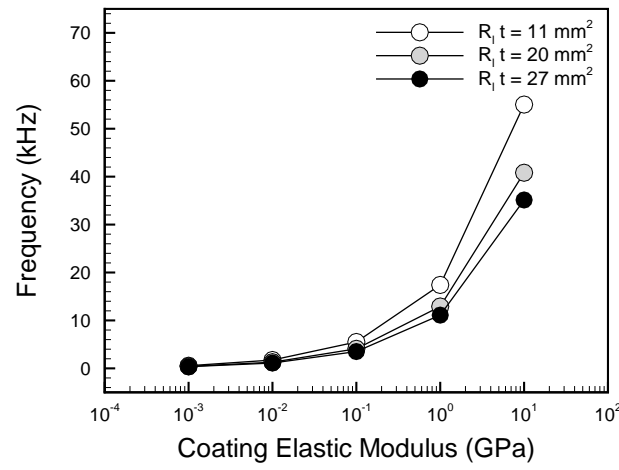
Figure 2.3: Resonant frequency for each geometry and material aggregate configuration studied in the numerical analyses, computed using Eq. (2.5).

The spring mass system considered here can also be used to indicate the best aggregate configuration for a specific resonant frequency. We derive general tuning equations which can be used to configure aggregates for a particular loading case. For an assigned frequency $\omega = \bar{\omega}$, Eq. (2.4) or Eq. (2.5) provide the optimal combination of geometry and mechanical properties for the aggregates. In particular, for an assigned geometry one can estimate the appropriate material stiffness E_c as

$$E_c = \frac{2}{3} R_l \, t \, \rho_l \, \bar{\omega}^2. \tag{2.6}$$

Likewise, for an assigned material, the geometrical term $R_l \, t$ is given by

$$R_l \, t = \frac{3}{2} \frac{E_c}{\rho_l \, \bar{\omega}^2}, \tag{2.7}$$

which provides an approximate definition of the aggregate size.

The variation of the coating elastic modulus E_c and the aggregate size $R_l \, t$ with the resonant frequency are visualized in Figures 2.4(a) and 2.4(b), respectively. The figures provide interesting design suggestions according to the application desired of the metaconcrete material. For the material to be employed as pro-

(a) Elastic modulus
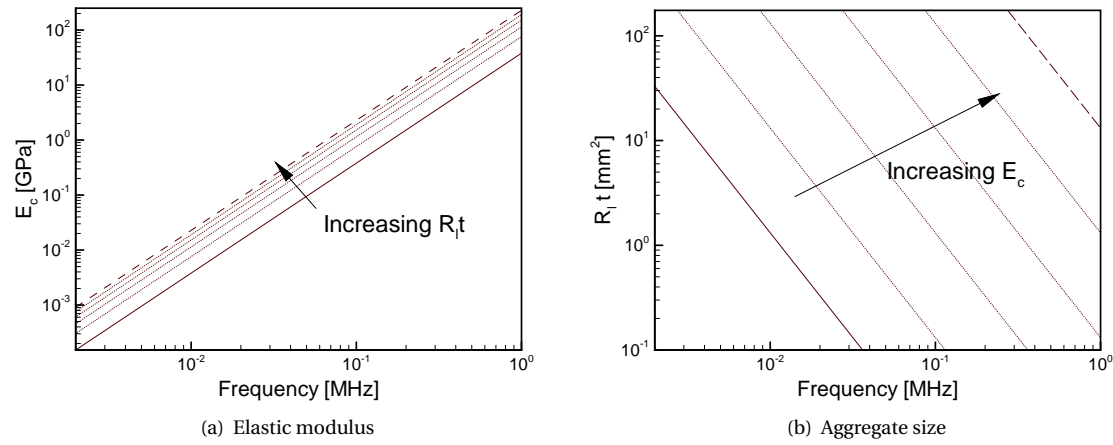
(b) Aggregate size

Figure 2.4: Dependence of aggregate parameters on the resonant frequency. (a) Elastic modulus of the soft coating. Lines correspond to different aggregate sizes $R_l\, t$, from 5 mm^2 (solid line) to 30 mm^2 (broken line). (b) Size of the aggregate. Lines correspond to different elastic moduli E_s, from 0.001 GPa (solid line) to 100 GPa (broken line).

tection against blast loading, metaconcrete must behave as a resonant material at high frequencies, since blast pressure histories are typically characterized by high frequency spectra. Adopting a stiff coating layer and a small aggregate size achieves the high resonant frequencies desired, as seen in Figure 2.4(a). For the case of protection against earthquakes, whose frequencies are in the range 0.01-10 Hz, the aggregates must be of larger size and a lower value of elastic modulus must be chosen, see Figure 2.4(b).

2.1.2.2   Three–dimensional model for resonant frequency

The aggregate resonant frequency given by Eq. (2.5) provides an estimate for the purposes of aggregate tuning and design. However, the one-dimensional spring–mass model used to derive this equation cannot adequately capture all the behavior present in a three-dimensional metaconcrete model. To more accurately understand the resonant behavior of the system, we can model a three-dimensional metaconcrete aggregate using commercial finite element software capable of performing frequency or modal analyses (Abaqus/Standard 6.12-2, 2012).

We consider a 0.03 m mortar cube containing a single aggregate, representing a periodic unit cell from a metaconcrete slab. Figure 2.5 depicts the finite element model used to estimate the modal properties of a 1 mm nylon coated aggregate. The model is meshed with quadratic tetrahedral elements with a maximum size of 2.5 mm, reducing to a smaller size within the coating and core phases. We consider four aggregate cases for this analysis: 1 mm and 3 mm rubber coated aggregates, and 1 mm and 3 mm nylon coated aggregates. Table 2.4 provides the discretization data for the geometry cases considered, along with the volume fractions for each phase of the aggregate, given as a percentage of total slab volume.

Boundary conditions are assigned to the outer edges of the cube so that only the modes of interest,
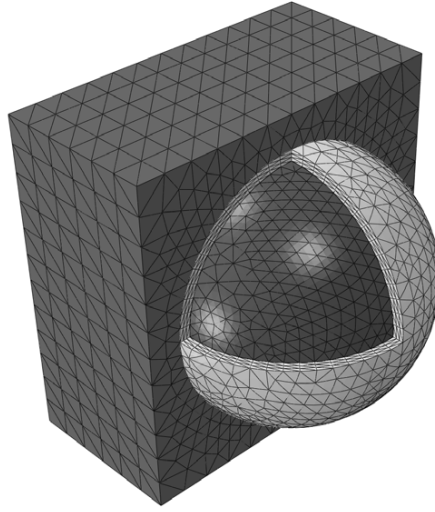
Figure 2.5: A periodic unit cell used for the modal analysis, showing the outer mortar block containing a 1 mm nylon coated lead aggregate.

Table 2.4: Discretization data and volume fractions for the finite element periodic unit cell model.

Configuration	Nodes	Elements	V_{mortar} (%)	$V_{coating}$ (%)	V_{lead} (%)
A	40,307	25,047	73.2	6.2	20.6
C	41,074	26,260	73.2	15.5	11.3

those involving the aggregate constituents, are output from the analysis. Each part within the model is assigned the appropriate properties as given in Table 2.1 and a linear elastic material model is assumed for each constituent.

A frequency analysis is run to compute the first four eigenfrequencies and corresponding eigenshapes. Table 2.5 lists the results for each aggregate configuration. The first mode shape represents a rigid body rotation of the lead core inside the compliant coating. The second mode shape consists of rigid body translation of the heavy core, oscillating within the coating material. The third and forth mode shapes correspond to vibration and flexing of the lead core and/or coating materials.

Table 2.5: Resonant frequencies from both Eq. (2.5) and the finite element periodic unit cell model.

Configuration	Eq. (2.5) (kHz)	Finite Element Unit Cell (kHz)			
		Mode 1	Mode 2	Mode 3	Mode 4
1 mm Rubber	1.74	1.99	5.99	25.00	27.70
3 mm Rubber	1.11	1.51	3.39	10.44	11.12
1 mm Nylon	17.41	18.84	21.12	32.14	36.42
3 mm Nylon	11.11	15.08	15.94	34.19	36.92

The eigenshapes are also illustrated in Figure 2.6, where each of the first four mode shapes are shown for the 1 mm nylon aggregate configuration. A contour plot of the maximum principal strain is shown for each mode, and it can be seen that the first two modes display rigid body motion, with rotation of the heavy core in the first mode and translation in the second mode. The third and fourth modes display mixed bending and oscillation of the core and coating.

(a) Mode 1

(b) Mode 2

(c) Mode 3

(d) Mode 4
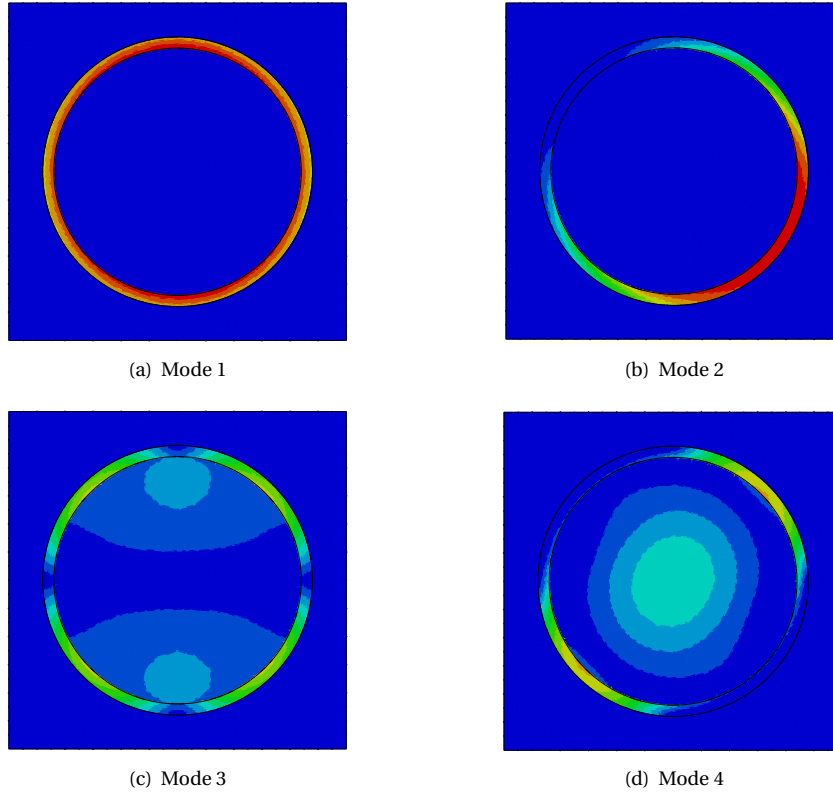
Figure 2.6: Contour plot of the maximum principal strain for each of the eigenshapes corresponding to the first four eigenfrequencies for a metaconcrete unit cell containing a 1 mm nylon coated aggregate; blue represents zero strain and red indicates large values of strain.

The second mode shape containing rigid body translation of the heavy core is the mode we wish to activate in metaconcrete and is also the mode shape we hoped to capture in Eq. (2.5). However, as can be seen from Table 2.5, while the frequency from Eq. (2.5) reasonably estimates the first mode natural frequency, it underestimates the second mode resonant frequency by approximately 2-4 kHz. Therefore, the additional accuracy provided by the eigenfrequencies from the modal analysis allows us to see which mode shapes produce changes in slab behavior. In particular, in Chapter 3 we analyze the change in wave transmission across the depth of a metaconcrete slab, computing a transmission coefficient for a range of forcing frequencies. The eigenfrequencies computed in Table 2.5 enable us to more directly attribute changes in transmission coefficient to the activation of a particular mode of resonance.

2.2   Finite element slab models

To investigate the behavior of metaconcrete we incorporate the aggregate configurations discussed in Section 2.1 into a finite element slab model. Using a numerical analysis of each aggregate configuration for a number of different loading cases, we can explore how aggregate design influences slab performance.

2.2.1   Slab configuration and meshes

We consider an infinite planar slab of thickness L and restrict our attention to a square cross section of material spanning the entire slab thickness, shown in Figure 2.7. The concrete portion is constrained so that is does not deform in the slab plane.
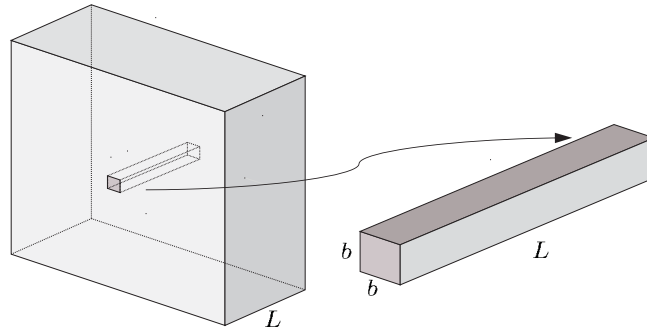
Figure 2.7: Geometry of the concrete slab of thickness L, and the restricted slab portion of edge length b.
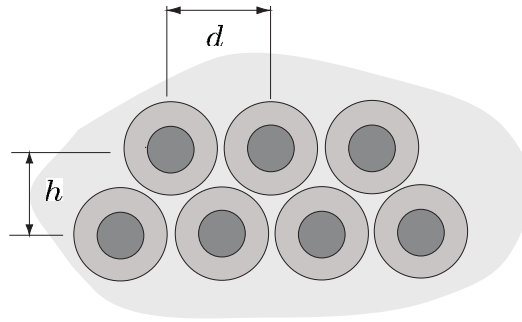
Figure 2.8: Geometrical assembly of the aggregates in a regular two-dimensional arrangement, characterized by heavy cores located at central distances of magnitude d and h.

The size b of the sample is chosen to be significantly smaller than the slab thickness and close to the actual size of the aggregates, which are arranged periodically at a distance d one from another (see

Figure 2.8). Geometrical constraints impose the following restriction:

$$2\left(R_l + t\right) \leq d. \tag{2.8}$$

To increase the density of the aggregates within the slab, we model quarter aggregates along the longitudinal edges, at a distance $h = d\sqrt{3}/2$ from the center of the aligned aggregates, as seen in Figure 2.8.

The total volume and the total mass of the system can be expressed in terms of the volume and mass of the components,

$$v_{\text{tot}} = v_m + v_c + v_l, \qquad M_{\text{tot}} = v_m \rho_m + v_c \rho_c + v_l \rho_l, \tag{2.9}$$

where v_i and ρ_i denote, respectively, the volume and the density of the component i. Indices m, c, and l refer to the mortar, compliant coating, and lead phases, respectively. The volume fractions of the components V_i, and the filling fraction of the aggregates in terms of weight f_a, are defined as:

$$V_i = \frac{v_i}{v_{\text{tot}}}, \qquad f_a = \frac{1}{M_{\text{tot}}}\left(v_c \rho_c + v_l \rho_l\right). \tag{2.10}$$

In the present study, we assume $L = 0.24$ m and $b = 0.03$ m with the aggregates arranged at 0.03 m centers. Each aggregate has a dimension $R_l + t = 12$ mm, and we vary R_l and t according to the values reported in Table 2.2.

In the numerical analyses we consider two different aggregate arrangements within the slab. The primary configuration is a high–density arrangement, where we include the 28 quarter spheres located along the longitudinal edges of the slab, resulting in 36 separate inclusions. This arrangement is considered for all numerical analyses. A low–density arrangement is also used in the analysis of wave transmission in Chapter 3, and consists of only 8 whole spherical aggregates located along the central axis of the slab. The volume and filling fractions for both arrangements are listed in Table 2.6 for each of the aggregate geometry configurations. The filling ratio varies according to the choice of the compliant coating material.

Table 2.6: Geometrical data.

# Aggregates	Configuration	$R_l\,t$ (mm^2)	V_m (%)	V_c (%)	V_l (%)	f_a (%)
	A	11	73.2	6.2	20.6	56.8-57.2
8	B	20	73.2	11.3	15.5	50.6-51.4
	C	27	73.2	15.5	11.3	43.9-45.4
	A	11	49.7	11.6	38.7	78.4-78.7
36	B	20	49.7	21.2	29.1	73.8-74.5
	C	27	49.7	29.1	21.2	68.3-69.7

Configuration A is visualized in Figure 2.9. The solid model is discretized with a uniform mesh, which reduces, if necessary, to a smaller value within the soft layer according to the coating thickness, as shown

Table 2.7: Discretization data.

Mesh Size	Configuration	Nodes	Elements	$h_{\min}$ (mm)	h_{avg} (mm)
Coarse $h = 2.5$ mm	A	19228	96314	0.0026	0.503
	B	19645	95390	0.0271	0.502
	C	20891	107562	0.1271	0.486
Fine $h = 1.5$ mm	A	102,965	561,846	0.0762	0.279
	C	84,000	451,457	0.1031	0.287
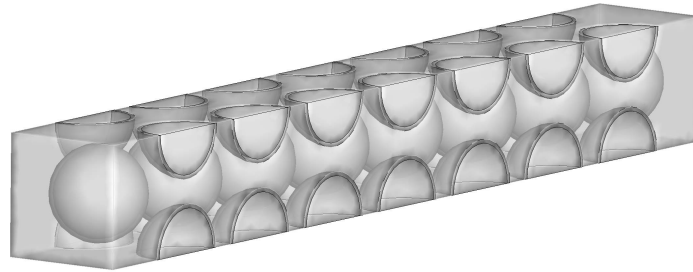
(a) Solid model
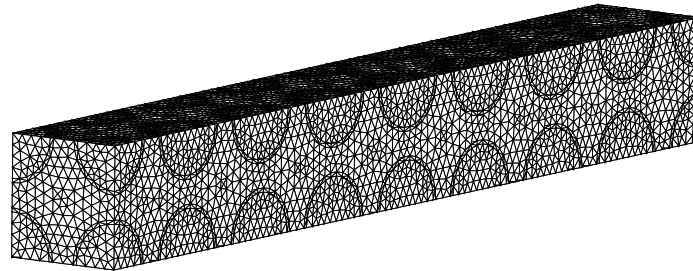
(b) Finite Element Mesh

Figure 2.9: Solid model and finite element discretization for a metaconcrete slab containing an array of 1 mm coated aggregates (configuration A) and discretized with a coarse mesh of size $h = 2.5$ mm.

in Figure 2.9(b). Two mesh sizes are needed for the numerical analyses; a coarse mesh of size $h = 2.5$ mm, and a fine mesh of size $h = 1.5$ mm, which is used for configurations A and C in the calculation of transmission coefficients discussed in Chapter 3.

The discretization data for each finite element configuration is presented in Table 2.7, listing the number of nodes and elements for each finite element model. We also present more detailed information on the mesh size for each slab case, listing the minimum mesh size $h_{\min}$, and the average mesh size h_{avg}, within the mortar phase of the slab. The minimum mesh size is used in the implementation of the fracture algorithm, discussed in Chapter 5.

The elastic material behavior of each slab constituent is described by a neo-Hookean material model, extended to the compressible range and adopting the material properties listed in Table 2.1. Details of the model can be found in Appendix A.

In the numerical analyses we model the matrix surrounding the aggregates as a homogeneous material with the equivalent properties of concrete. Although standard concrete is a true composite, we assume that for applications where the elastic behavior is dominant it can be considered a homogeneous material. Conversely, metaconcrete is non–homogeneous because of the particular choice of aggregates. In each numerical study we therefore also model a homogeneous slab for comparison with metaconcrete, where we fill the entire finite element model with the homogeneous concrete material.

2.2.2   Blast wave loading

We test the metaconcrete slab model with two loading profiles. The first is a harmonic displacement applied to the end surface of the slab at a prescribed frequency in order to activate resonance within the aggregates. This is described in further detail in Chapter 3. We also consider a loading caused by a blast wave, which is used in Chapter 4 and Chapter 5 to investigate a range of slab behavior.

(a) Blast force versus time   (b) Blast force magnitude versus frequency
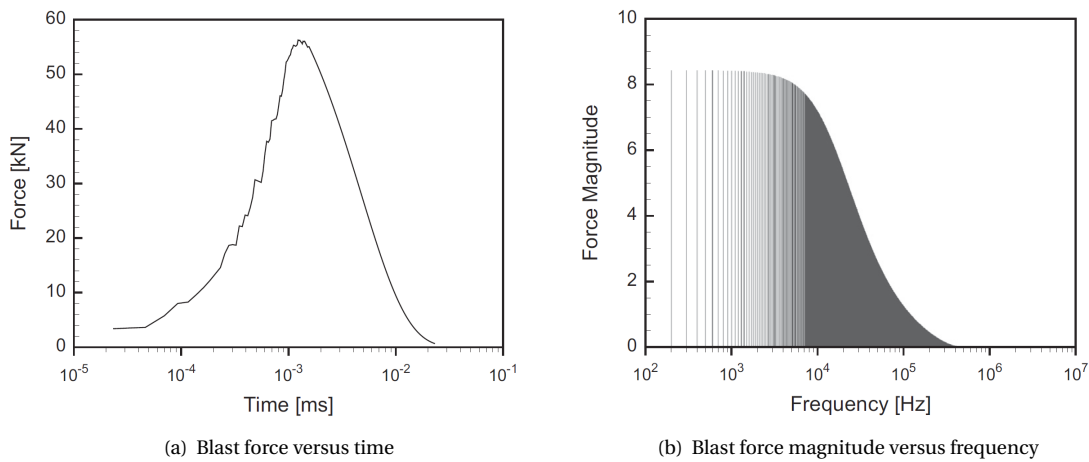
Figure 2.10: Blast wave loading: (a) Variation in time of the resultant blast pressure on the exposed surface of the slab. (b) Fourier transform (signal magnitude) of the blast force.

The blast pressure history activates a large spectrum of frequencies within the system. We assume that the blast is applied to the forward side of the slab, while the opposite side is free to move, and we apply periodic boundary conditions to the lateral surfaces. The blast pressure history is caused by the ignition of an explosion in air, which results in a spherical pressure wave that propagates out from the ignition site. We assume a blast force caused by the ignition of an explosive charge located 0.015 m from the central point of the exposed slab surface. The controlling parameter for explosions in atmosphere is the yield factor λ, i.e., the cubic root of the ratio between the energy released by the actual explosion and the energy released in a 1 ton of TNT reference explosion. The model for the blast pressure history used in the calculations is summarized in Appendix B and a more detailed description of explosions in air can

be found in, e.g., Kinney (1962).

The blast force is characterized by the time history and frequency spectrum. The total blast force at time t is given by the resultant of the blast pressures acting normally to the exposed surface A_{exposed}, i.e.

$$F(t) = \int_{A_{\text{exposed}}} p(t) \, dA. \tag{2.11}$$

To demonstrate the shape of a typical blast profile we consider, as an example, a blast pressure wave caused by a yield factor $\lambda = 0.01$, which is applied to the exposed end face of a metaconcrete slab. This yield factor corresponds to the ignition of a 1 g TNT charge. Figure 2.10(a) shows the time history of the blast force. The frequency spectrum, shown in Figure 2.10(b), is obtained in terms of magnitude by taking the Fourier transform of the blast force time history. For this particular example, the blast pressure acts for a short time interval of less than 0.01 ms, and most of the excited frequencies are in the range between 1 kHz and 1 MHz, indicating the frequency range for which activation of the resonant aggregates may occur.

Chapter 3

Wave transmission in a metaconcrete slab

Transmission ratio plots have been used to quantify the band gap and resonance–induced behavior of acoustic crystals with a layered structure analogous to that used in metaconcrete (Liu et al., 2000b; Sheng et al., 2003). These crystals have been shown to exhibit resonant behavior when experimentally tested with sound waves of varying frequencies, where the ratio of the change in wave amplitude across the crystal is measured and plotted against input wave frequency. The dispersion equation, which defines the wave frequencies for different wave numbers, is also closely related to wave transmission behavior. Plotting the dispersion equation allows for the identification of the band gap behavior of the system. The formation of band gaps within locally resonant sonic crystals has also been linked to the negative effective mass that these materials display near the resonant frequency of the inclusions, caused by out–of–phase behavior between the constituents and the matrix.

We can investigate the wave transmission properties of metaconcrete by modeling slab behavior using both one– and three–dimensional systems. We begin by considering a one–dimensional model of a meta-concrete slab and analyze the link between band gap behavior, resonance, and wave attenuation using this simplified system. Similar behavior can be seen by computing a wave transmission ratio for a finite element metaconcrete model containing a periodic array of aggregates, where we consider the amount of energy transmitted through a slab. We examine the transmission behavior and resonance activation of metaconcrete by considering a metaconcrete slab subjected to a displacement loading over a range of chosen frequencies. The information gained from these analyses allows us to more accurately determine the appropriate aggregate properties for specific loading applications.

3.1 The characteristics of aggregate resonant behavior

We introduce the effect of local resonances in metaconcrete by simplifying the system to a one–dimensional spring–mass model. This enables us to easily derive the dispersion relation for the system, which aids in the visualization of band gap behavior. While the one–dimensional model does not capture all of the complexities of the three–dimensional slab model, it does address the most important behavior present,

which is the activation of the resonant aggregates and the development of negative effective mass. This leads to the attenuation of the wave motion within the band gap freqeuncy range, and we can observe this effect by deriving a transmission ratio for the one–dimensional model. A one–dimensional metaconcrete model will therefore provide further insight into the link between local resonances and formation of band gaps, which will aid in the understanding of wave transmission behavior produced by a three–dimensional finite element slab model, discussed in Section 3.2.

3.1.1   Dispersion and a simple spring–mass chain

We begin by deriving the dispersion relation for the simple one–dimensional spring–mass chain shown in Figure 3.1 (Banerjee, 2011). The system consists of periodically spaced lumped masses m, with a unit cell spacing of L, connected by springs of stiffness k.
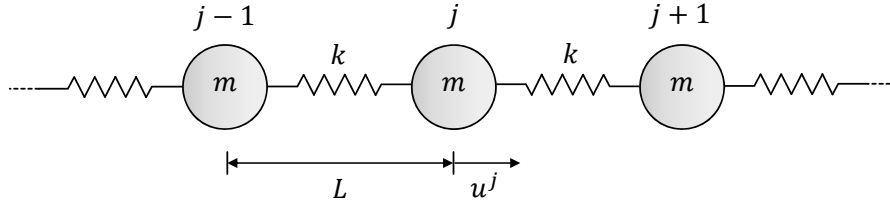
Figure 3.1: Simple one–dimensional spring–mass system representing a periodic structure.

The displacement at unit cell j is given by u^j and the system is constructed from an infinite number of the spring–mass unit cells. Using Newton's second law, we can therefore write the equation of motion for the j-th mass as

$$m\ddot{u}^j + k(u^j - u^{j-1}) + k(u^j - u^{j+1}) = 0, \tag{3.1}$$

where $\ddot{u}^j$ is the acceleration of the j-th mass given by $\ddot{u}^j = d^2 u^j / dt^2$.

The harmonic wave solution for the $(j+n)$-th unit cell is expressed in the form

$$u^{j+n} = A e^{i(jqL+nqL-\omega t)}, \tag{3.2}$$

where A is the wave amplitude, q is the wave number, and ω is the oscillation frequency, and we assume that only the real part of Eq. (3.2) is to be taken for the physical interpretation of the solution. This can also be written in the form

$$u^j = A e^{i(jqL-\omega t)}, \tag{3.3}$$

where we have

$$\frac{d^2 u^j}{dt^2} = -\omega^2 u^j \quad \text{and} \quad u^{j+n} = u^j e^{inqL}. \tag{3.4}$$

Note that this indicates that the equation satisfies the Bloch periodicity condition, which is a consequence of the Bloch-Floquet theorem. Thus, we can rewrite the equation of motion by substituting Eq. (3.4) for $n = \pm 1$, which gives

$$\left[k(2 - e^{-iqL} - e^{iqL}) - m\omega^2 \right] u^j = 0. \tag{3.5}$$

We can use identities $e^{iqL} + e^{-iqL} = 2\cos(qL)$ and $1 - \cos(qL) = 2\sin^2(qL/2)$ to rewrite this expression as

$$\left[\frac{4k}{m} \sin^2\left(\frac{qL}{2} \right) - \omega^2 \right] u^j = 0. \tag{3.6}$$

For real q, and since $\omega > 0$, this equation has a nontrivial solution only if

$$\omega^2(q) = 4\frac{k}{m} \sin^2\left(\frac{qL}{2} \right), \tag{3.7}$$

or, noting that $\omega_0 = \sqrt{(k/m)}$ is the natural frequency of the mass-spring system

$$\omega(q) = 2\sqrt{\frac{k}{m}} \left| \sin\left(\frac{qL}{2} \right) \right| = 2\omega_0 \left| \sin\left(\frac{qL}{2} \right) \right|. \tag{3.8}$$

This expression represents the dispersion relation for the structure, which is plotted in Figure 3.2.
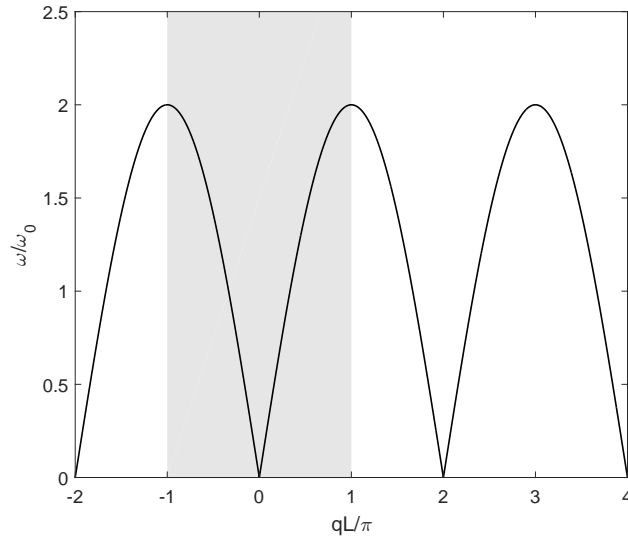
Figure 3.2: Dispersion plot for the one–dimensional spring–mass system, showing the first Brillouin zone shaded in gray.

The dispersion plot is a periodic function of q with a period of $2\pi/L$, and at the value of the period the function falls to zero. This is explained by looking at the reciprocal lattice vector, which has a spacing of $d := 1/L$. Thus the frequency is zero every time q becomes an integer multiple of $2\pi d$. The mode where

both ω and q go to zero simultaneously is called the acoustic mode.

We may use the periodicity to concentrate on a small range of values of k while still being able to understand the behavior of the system for all q. This irreducible set of values of q is indicated by the gray region in Figure 3.2, and is called the first Brillouin zone. At the boundaries of the Brillouin zone $\omega = 2\omega_0$, and the group velocity $d\omega/dq$ becomes zero. Therefore we have standing waves for values of q which are odd integer multiples of π/L.

Because the system is a periodic array of units consisting of a single spring–mass system, i.e., there is only one k and one m in the model, we only see one mode in the dispersion plot. We will observe other modes as further detail is included in the model.

3.1.2 Spring–mass chain with local resonances

We increase the complexity of our one–dimensional model by adding local resonances to the simple spring–mass chain (Huang et al., 2009; Huang and Sun, 2009). This allows the system to approximately represent a chain of metaconcrete aggregates in a mortar matrix. The updated model is shown in Figure 3.3 where an additional spring–mass system, with mass m_2 and spring constant k_2, is added internally to the lumped mass used in simple chain arrangement, which is now denoted m_1. The unit cells are periodically spaced at a distance L and the external masses are connected by a spring with constant k_1.
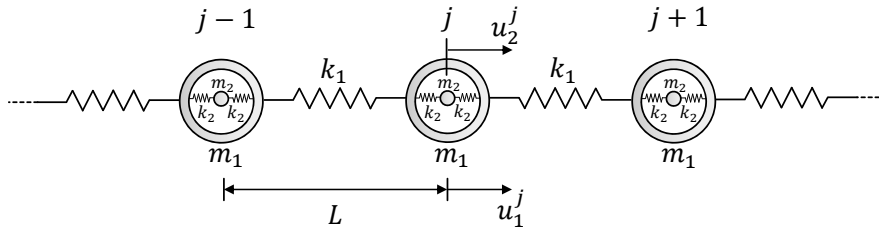
Figure 3.3: One–dimensional spring–mass chain with local resonances. The system is constructed using a periodic array of mass–in–mass unit cells.

We can derive the dispersion relation for this system using the same process as used previously. We begin by writing the equations of motion for the both the external and internal masses,

$$m_1^j \ddot{u}_1^j + k_1 \left(2u_1^j - u_1^{j-1} - u_1^{j+1} \right) + 2k_2 \left(u_1^j - u_2^j \right) = 0 \tag{3.9}$$

$$m_2^j \ddot{u}_2^j + 2k_2 \left(u_2^j - u_1^j \right) = 0. \tag{3.10}$$

We substitute the following relations from the time harmonic wave solution

$$\ddot{u}_1^j = -\omega^2 u_1^j \qquad \ddot{u}_2^j = -\omega^2 u_2^j \tag{3.11}$$

$$u_1^{j+1} = u_1^j e^{iqL} \qquad u_1^{j-1} = u_1^j e^{-iqL} \tag{3.12}$$

to get

$$-m_1 \omega^2 u_1^j + k_1 \left(2u_1^j - u_1^j e^{-iqL} - u_1^j e^{iqL}\right) + 2k_2 \left(u_1^j - u_2^j\right) = 0 \tag{3.13}$$

$$-m_2^j \omega^2 u_2^j + 2k_2 \left(u_2^j - u_1^j\right) = 0. \tag{3.14}$$

Using again the following identities, $e^{iqL} + e^{-iqL} = 2\cos(qL)$ and $1 - \cos(qL) = 2\sin^2(qL/2)$, we can rewrite these expressions as

$$\left(-m_1 \omega^2 + 2k_2 + 4k_1 \sin^2\left(\frac{qL}{2}\right)\right) u_1^j - 2k_2 u_2^j = 0 \tag{3.15}$$

$$-2k_2 u_1^j + \left(-m_2^j \omega^2 + 2k_2\right) u_2^j = 0. \tag{3.16}$$

In order to find the dispersion relation for this system we want to reduce the problem into a generalized matrix eigenvalue problem of the form

$$\left[\mathbf{K(q)} - \omega^2 \mathbf{M}\right] \mathbf{u} = \mathbf{0}, \tag{3.17}$$

where $\mathbf{M}$ and $\mathbf{K}$ are the mass and stiffness matrices, respectively, which contain the geometry and material parameters, $\mathbf{q}$ is the wave number, ω is the frequency, and $\mathbf{u}$ is the displacement vector for the degrees of freedom in the system. Thus, we rewrite the equations of motion in the form

$$\begin{bmatrix} -m_1 \omega^2 + 2k_2 + 4k_1 \sin^2\left(\frac{qL}{2}\right) & -2k_2 \\ -2k_2 & -m_2^j \omega^2 + 2k_2 \end{bmatrix} \begin{bmatrix} u_1^j \\ u_2^j \end{bmatrix} = 0. \tag{3.18}$$

This eigenvalue problem has a nontrivial solution if $\det\left(\mathbf{K(q)} - \omega^2 \mathbf{M}\right) = 0$, resulting in

$$m_1 m_2 \omega^4 - \left(2k_2 (m_1 + m_2) + 4m_2 k_1 \sin^2\left(\frac{qL}{2}\right)\right) \omega^2 + 8k_1 k_2 \sin^2\left(\frac{qL}{2}\right) = 0. \tag{3.19}$$

Solving this expression for $\omega(q)$ gives the dispersion relation for the locally resonant spring–mass chain,

$$\omega(q) = \left(\pm \frac{\sqrt{\left(-4k_1 m_2 \sin^2\left(\frac{qL}{2}\right) - 2k_2 (m_1 + m_2)\right)^2 - 32k_1 k_2 m_1 m_2 \sin^2\left(\frac{qL}{2}\right)}}{2m_1 m_2}\right.$$

$$\left. + \frac{2k_1 \sin^2\left(\frac{qL}{2}\right)}{m_1} + \frac{k_2}{m_1} + \frac{k_2}{m_2}\right)^{1/2} \tag{3.20}$$

taking only the positive eigenvalues. Note that the dispersion relation for this case results in an extra mode, called the optical mode. We will see this in more detail upon examination of the dispersion plot resulting from the use of equivalent metaconcrete properties in one–dimensional form, discussed in the

following section.

We can also rearrange Eq. (3.19) into the following form

$$\omega^2 = 4\frac{k_1}{m_{\text{eff}}}\sin^2\left(\frac{qL}{2}\right) \tag{3.21}$$

with

$$m_{\text{eff}} = m_1 + \frac{\omega_0^2 m_2}{\omega_0^2 - \omega^2}, \tag{3.22}$$

where $\omega_0^2 = 2k_2/m_2$ is the resonant frequency of the internal spring–mass system. This equation is therefore equivalent to that given in Eq. (3.7) for the simple spring–mass chain; however, the mass m is now replaced with the effective mass m_{eff} (Yao et al., 2008; Huang et al., 2009). This frequency–dependent mass is identical to that derived by Milton and Willis (2007) in the analysis of a one–dimensional bar with voids containing hidden resonant systems, as given by Eq. (1.8) of Chapter 1. Just above the resonant frequency ω_0, the effective mass becomes very large and negative in value, leading to the response being out of phase with the input force. This is what is known as *negative effective mass*, and was discussed in relation to acoustic metamaterials in Chapter 1. When the oscillation frequency reduces towards zero, i.e., in the long wavelength limit as $\omega \to 0$, the effective mass approaches $m_{\text{eff}} = m_1 + m_2$, and the static mass for the system is recovered. It is the presence of local resonances within the system which leads to negative effective mass, which in turn creates the wave attenuation properties observed in locally resonant metamaterials.

Eq. (3.21) also implies that the lumped mass of Figure 3.1 can simply be replaced in the equations of motion by an effective frequency dependent mass m_{eff}, as demonstrated in Figure 3.4. In light of this, we can now easily derive a simple relation for the amplitude tranmission ratio.
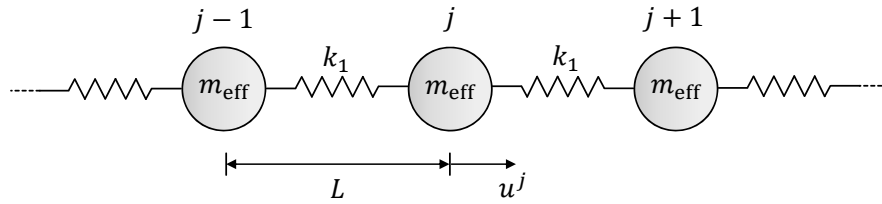
Figure 3.4: One–dimensional spring–mass chain containing lumped masses with effective properties equivalent to a mass–in–mass resonator.

For a finite periodic system of N units, the amplitude transmission of the spring–mass chain can be computed from the ratio given by the displacement amplitude of the last unit over the displacement amplitude of the excitation (Yao et al., 2008). Assuming that the displacement u_1^j of the j-th unit is given by $u_1^j = \bar{u}_1^j e^{-i\omega t}$, where $\bar{u}_1^j$ is the time–independent complex displacement amplitude, i.e., $\bar{u}_1^j = A_1 e^{jqL}$, we

can rewrite the equations of motion for the simple chain using the effective mass m_{eff},

$$\left(2k_1 - \omega^2 m_{\text{eff}}\right)\bar{u}_1^j = k_1 \left(\bar{u}_1^{j+1} + \bar{u}_1^{j-1}\right), \qquad j = 1, 2, \ldots, N-1 \tag{3.23}$$

$$\left(k_1 - \omega^2 m_{\text{eff}}\right)\bar{u}_1^j = k_1 \bar{u}_1^{j-1}, \qquad j = N. \tag{3.24}$$

From Eqs. (3.23) and (3.24), we can write the transmission ratio $T = \left|\bar{u}_1^N / \bar{u}_1^0\right|$ as

$$T = \left|\prod_{j=1}^N T_j\right|, \tag{3.25}$$

where $T_j = \bar{u}_1^j / \bar{u}_1^{j-1}$ is given by the recurrence relation

$$T_j = \frac{k_1}{k_1 \left(2 - T_{j+1}\right) - m_{\text{eff}}\omega^2} \qquad j = 1, 2, \ldots, N \tag{3.26}$$

with $T_{N+1} = 1$.

Another quantity of interest is the relative amplitudes between the outer mass m_1 and the inner mass m_2 at different values of oscillation frequency. We can find a ratio of these amplitudes by substituting the harmonic wave solution from Eq. (3.11), i.e., $u^{j+n} = A_\gamma e^{i(jqL+nqL-\omega t)}$, into the equation of motion for the inner mass, i.e., Eq. (3.10), which gives

$$\frac{A_2}{A_1} = \frac{2k_2}{2k_2 - m_2\omega^2} = \frac{1}{1 - (\omega/\omega_0)^2}, \tag{3.27}$$

where A_1 and A_2 are the displacement amplitudes for the outer and inner masses, respectively (Milton and Willis, 2007).

3.1.3   Effect of local resonances in a one–dimensional metaconcrete model

We can use the one–dimensional spring–mass model from Section 3.1.2 to form a simplified model of a metaconcrete slab. This will allow us to investigate the formation of band gap type behavior and to approximate the frequency location of changes in transmission for comparison with the three-dimensional model discussed in the next section.

We model an eight aggregate periodic configuration, using the outer mass m_1 and spring constant k_1 to represent the mortar, and the inner mass m_2 and spring constant k_2 to model the lead core and coating material of the aggregate. The spring constant for the coating material is derived using the tuning equations from Section 2.1.2.1 of Chapter 2, and is given by

$$k_2 = \frac{\pi R_l^2 E_c}{t}. \tag{3.28}$$

Table 3.1: Aggregate configurations.

Configuration	R_l (mm)	t (mm)	Coating
1	11	1	Nylon
2	9	3	Nylon
3	11	1	Rubber
4	9	3	Rubber

Table 3.2: Mass and spring constants for the elements of the one–dimensional metaconcrete model.

Configuration	m_1 (kg)	m_2 (kg)	k_1 (N/m)	k_2 (N/m)
1	0.0494	0.0636	1.2296×10^9	3.8013×10^8
2	0.0494	0.0348	1.2296×10^9	8.4823×10^7
3	0.0494	0.0636	1.2296×10^9	3.8013×10^6
4	0.0494	0.0348	1.2296×10^9	8.4823×10^5

The spring constant for the mortar material is derived using a similar approach, by computing an equivalent stiffness for the mortar in a single slab unit cell, i.e.,

$$k_1 = \frac{E_m A}{L}, \tag{3.29}$$

where E_m is the elastic modulus of the mortar material, $A = b^2$ is the cross sectional area of the slab, and L is the equivalent length of the volume of mortar in a slab unit cell, given by

$$L = \frac{b^3 - \frac{4}{3}\pi (R_l + t)^3}{A}. \tag{3.30}$$

Substituting Eq. (3.30) into Eq. (3.29) therefore gives

$$k_1 = \frac{E_m A^2}{b^3 - \frac{4}{3}\pi (R_l + t)^3}. \tag{3.31}$$

We consider four aggregate cases; 1 mm and 3 mm nylon coated inclusions and 1 mm and 3 mm rubber coated inclusions, as listed in Table 3.1. The material properties and resonant frequencies for each of these configurations are presented in Section 2.1 of Chapter 2. Table 3.2 summarizes the values computed for each of the mass and spring constants used in the one–dimensional metaconcrete model.

The results for the nylon coated aggregates are shown in Figure 3.5 and Figure 3.7. The inclusion of the internally resonant masses creates a second mode in the dispersion plot, known as the optical mode. The dispersion relation is plotted only for the first Brillouin zone, i.e., for $qL = -\pi$ to $qL = \pi$. Due to the periodicity of the structure, this reduced range of values can represent the behavior of the system for all q, as discussed in relation to the dispersion plot for the simple mass-spring chain.

The resonant frequency ω_0, and the amplitude ratio $|A_2/A_1|$, are also shown in Figure 3.5, where it can be seen that the amplitude of the motion for the internal mass grows significantly larger than the amplitude of the external mass at the resonance frequency. The resonant frequency of 17.4 kHz lies near the lower end of the band gap frequency range, but slightly above the lower bound.
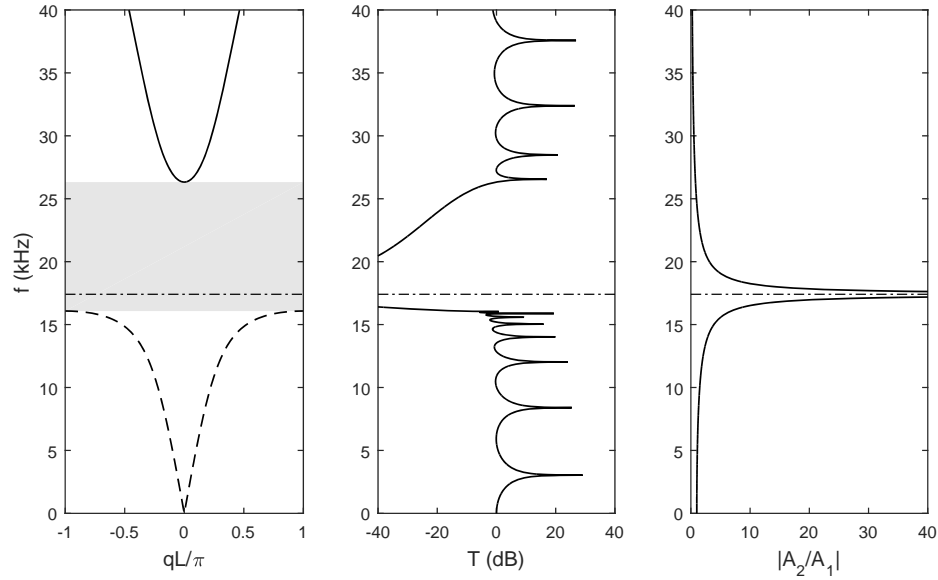
Figure 3.5: Plot of the dispersion relation, transmission ratio T, and amplitude ratio $|A_2/A_1|$ for a one–dimensional model based on a periodic array of *1 mm nylon* coated aggregates in a mortar matrix. The band gap is shaded in gray and the dotted line represents the natural frequency of the resonant aggregate ω_0.

From the plot of the dispersion relation, we observe a gap between the maximum value of the acoustic mode and the minimum value of the optical mode. This is a *band gap* and is caused by the inclusion of locally resonant spring–mass systems in the model and the interaction of these internal systems with the global spring–mass chain. The band gap for the 1 mm nylon coated inclusion spans the frequency range of 16.1 kHz to 26.3 kHz, as shown by the gray shaded region in Figure 3.5. We also observe that this band gap corresponds to the large dip seen in the plot of wave amplitude transmission T, where the transmission ratio drops dramatically from positive to negative values. This indicates that within the bad gap region, the system attains a negative value of effective mass which results in attenuation of the wave amplitude.

We can investigate the effect of negative effective mass by considering the link between the behavior within the band gap frequency range and the motion of the masses m_1 and m_2. From Eq. (3.22) we can see that negative mass occurs in the frequency range given by

$$\omega_0 < \omega < \omega_R, \qquad \omega_R = \omega_0 \sqrt{\frac{m_1 + m_2}{m_1}}. \tag{3.32}$$

The upper bound of this range corresponds with the upper bound of the band gap given by the dispersion relation, i.e., for the case of 1 mm nylon coated aggregates, $\omega_R = 26.3$ kHz. By substituting the amplitude ratio given in Eq. (3.27) into the time harmonic wave solution, we can compute the displacements of m_1 and m_2 for different forcing frequencies, i.e.,

$$u_1^j = A_1 e^{i(jqL-\omega t)} \tag{3.33}$$

$$u_2^j = A_2 e^{i(jqL-\omega t)} = \frac{A_1}{1-(\omega/\omega_0)^2} e^{i(jqL-\omega t)}, \tag{3.34}$$

where the wavenumber q is given by

$$q = \frac{\omega}{c_L}, \qquad c_L = \sqrt{\frac{E}{\rho}}, \tag{3.35}$$

and c_L is the longitudinal wave speed, which for the mortar matrix material is $c_L = 3464$ m/s . We can then compute the normalized real–valued displacement for each of m_1 and m_2 for four forcing frequencies: $0.2\omega_0$, $0.9\omega_0$, $0.75\omega_R$, and $1.2\omega_R$, i.e., one frequency much smaller than the resonant frequency, one just under the resonant frequency, one in the negative mass frequency range, and one at a frequency outside the upper bound of the band gap.

The displacements computed for the $j = 8$-th mass in a spring–mass chain representing 1 mm nylon coated aggregates are shown in Figure 3.6. At frequencies much lower than the resonant frequency, Figure 3.6(a) shows that the displacement of both masses are almost identical, with in phase motion of a similar amplitude. As the forcing frequency is increased to just below the resonant frequency, the displacement amplitude of the smaller inner mass m_2 becomes very large; however, both masses are still in phase with each other, as seen in Figure 3.6(b). When the oscillation frequency lies in the range $\omega_0 < \omega < \omega_R$, as shown in Figure 3.6(c) , the motion changes and the two masses oscillate out of phase. In fact, m_2 moves in the opposite direction to m_1, 180° out of phase and at three and a half times the displacement amplitude. When the forcing frequency further increases to a value above ω_R, the amplitude of both masses decreases. However, the motion of external mass becomes larger than that of the inner mass, and the two masses still move out of phase, see Figure 3.6(d). It is this transition to out of phase motion with a large amplitude contrast within the negative mass frequency range that leads to band-gap behavior and a reduction in transmission ratio.

We observe similar band gap behavior for the 3 mm nylon coated aggregate configuration, shown in Figure 3.7. However, in this case the band gap is much smaller and located at lower frequencies, spanning the range between 10.9 kHz and 14.5 kHz. For the 3 mm nylon case the mass of the heavy core m_2, is now smaller than the mass representing the mortar material m_1. This lower contrast between the two masses, in combination with a smaller spring constant due to the increase in coating thickness, results in a smaller band gap at a lower frequency. The lower bound of the band gap also corresponds with the resonant
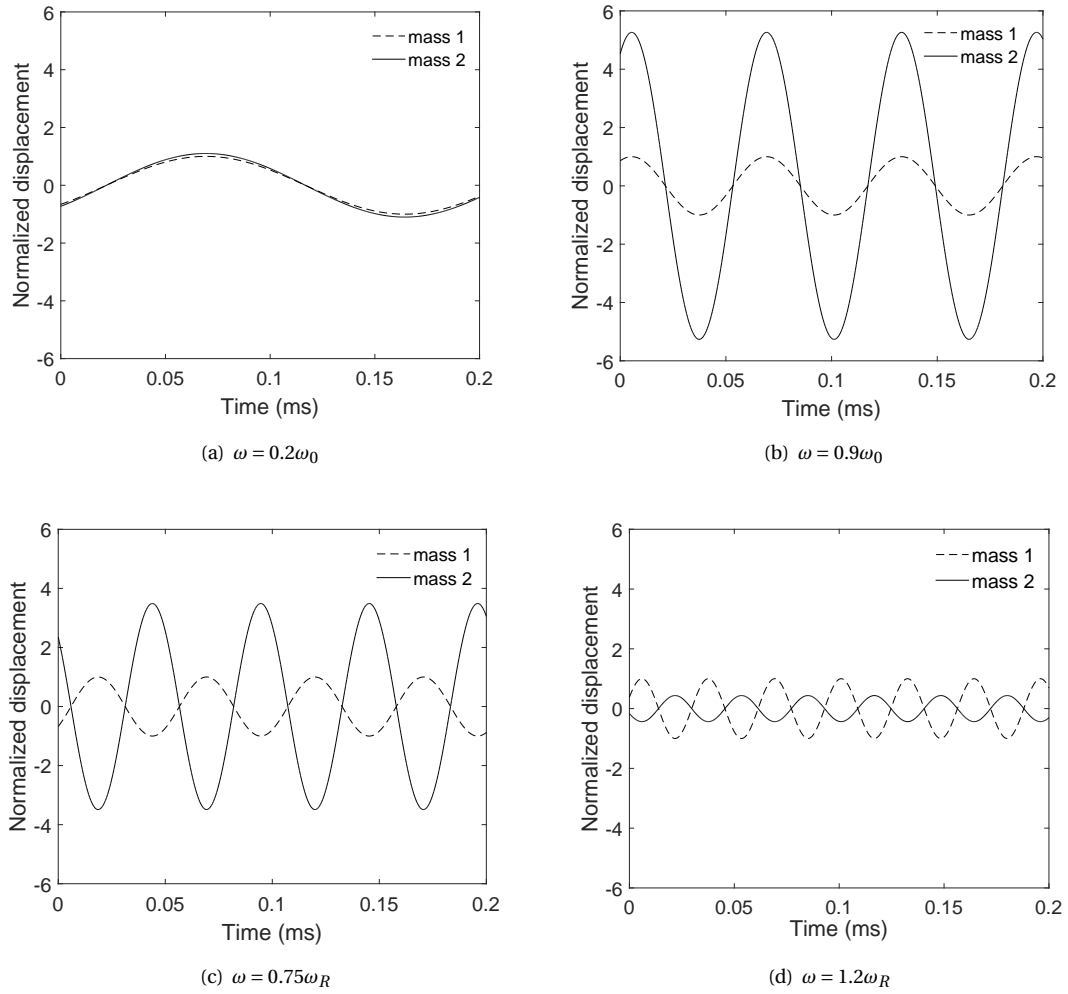
Figure 3.6: Displacement time histories for both the outer mass m_1 and the inner mass m_2 of the locally resonant spring–mass chain representing the 1 mm nylon aggregate configuration. The displacements are plotted for four forcing freqeuncies: (a) $0.2\omega_0$, (b) $0.9\omega_0$, (c) $0.75\omega_R$, and (d) $1.2\omega_R$.

frequency of the inclusion at 11.1 kHz. As in the 1 mm nylon aggregate configuration, the amplitude transmission ratio shows a large dip to negative values within the range of frequencies corresponding to the band gap and the resonant frequency of the inclusion.

The results for the rubber coated aggregate configurations are shown in Figure 3.8 and Figure 3.9. In this case, there is a lower contrast in stiffness between the parameters representing the coating material and the mortar matrix. This leads to a frequency gap that covers a narrower range of frequencies. The softer coating material also leads to resonance behavior and a band gap located at lower values of frequency. For the 1 mm rubber coated aggregates the band gap spans the range of 1.7 kHz to 2.6 kHz, and the resonant frequency, at 1.7 kHz, lies on the lower bound of the band gap range. Similarly, for the 3 mm rubber coated aggregates, the band gap ranges from 1.1 kHz to 1.4 kHz with a corresponding resonant
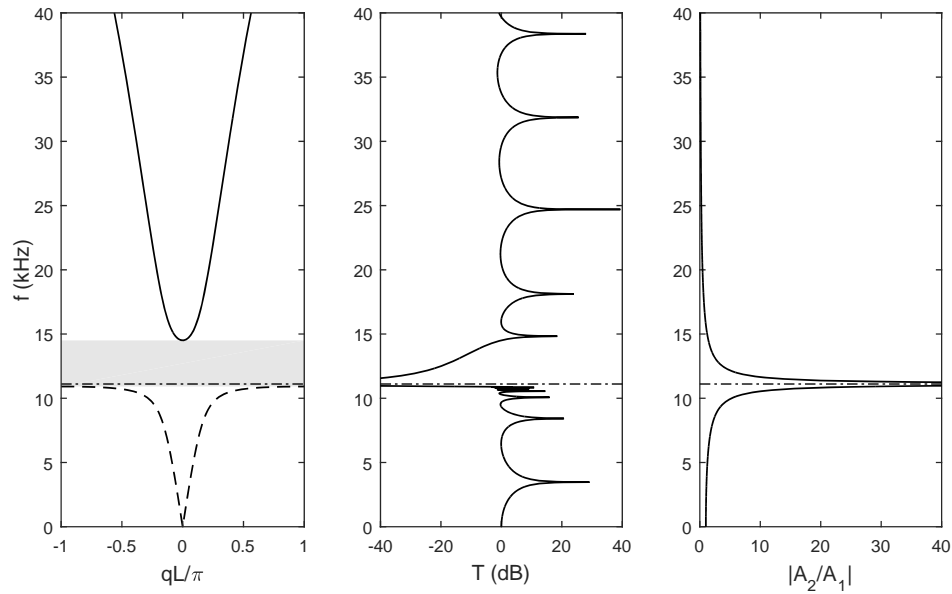
Figure 3.7: Plot of the dispersion relation, transmission ratio T, and amplitude ratio $|A_2/A_1|$ for a one–dimensional model based on a periodic array of *3 mm nylon* coated aggregates in a mortar matrix. The band gap is shaded in gray and the dotted line represents the natural frequency of the resonant aggregate, ω_0.
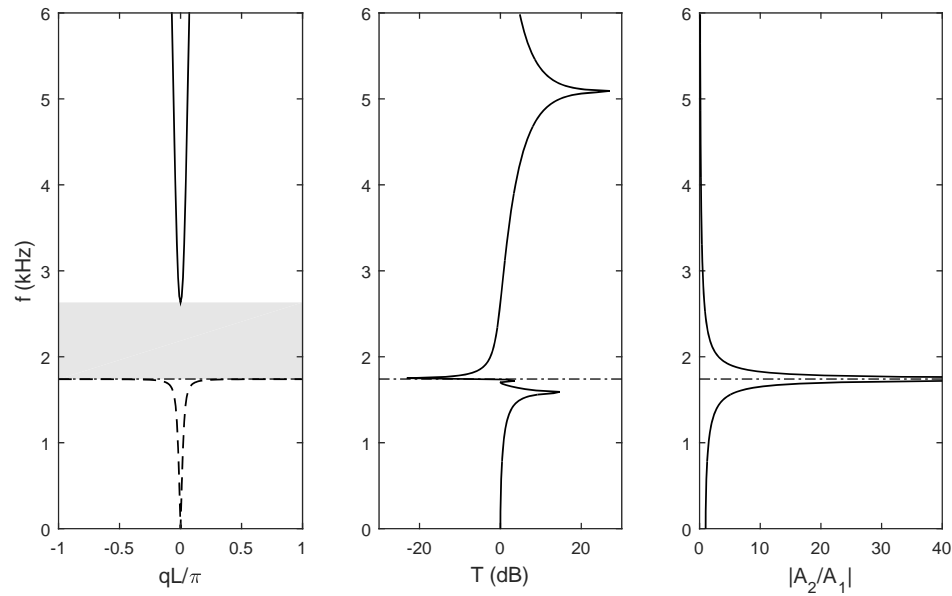
Figure 3.8: Plot of the dispersion relation, transmission ratio T, and amplitude ratio $|A_2/A_1|$ for a one–dimensional model based on a periodic array of *1 mm rubber* coated aggregates in a mortar matrix. The band gap is shaded in gray and the dotted line represents the natural frequency of the resonant aggregate, ω_0.
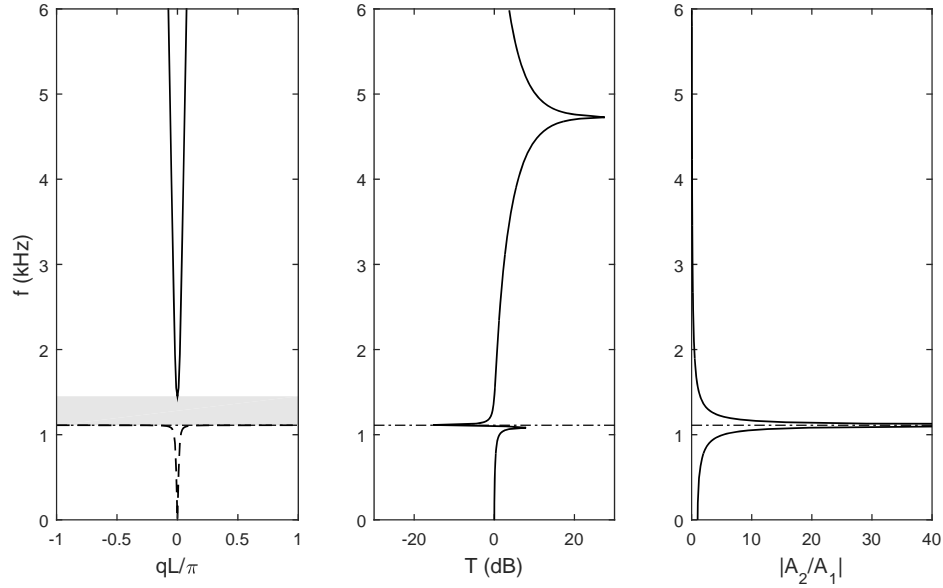
Figure 3.9: Plot of the dispersion relation, transmission ratio T, and amplitude ratio $|A_2/A_1|$ for a one–dimensional model based on a periodic array of *3 mm rubber* coated aggregates in a mortar matrix. The band gap is shaded in gray and the dotted line represents the natural frequency of the resonant aggregate, ω_0.

frequency of 1.1 kHz. The amplitude transmission plots also appear to have a different shape around the band gap range when compared with the the nylon coated aggregate case, with a less drastic contrast in magnitude between the regions located inside and outside the band gap frequency range.

Comparing the same geometry configuration for the two different coating materials, we see that changing the elastic modulus of the coating leads to a smaller band gap. Therefore, aggregates with a smaller coating thickness, i.e., a larger core radius, and a stiffer coating material, lead to wider gaps at higher frequencies. Aggregate configurations of this type display the highest mass contrast between the aggregate and the mortar matrix along with the highest one–dimensional equivalent coating stiffness. By contrast, a larger coating thickness and a softer coating material leads to a band gap, and corresponding wave attenuation, over a smaller range of lower frequencies. The one–dimensional study also indicates that aggregates within the metaconcrete slab can be easily tuned to create band gaps with different widths and frequency locations by simply changing the material properties and geometry of the aggregate constituents. We further investigate the transmission behavior of metaconcrete in the following section by using finite element analysis to compute wave energy transmission through a three–dimensional slab model.

3.2 Computation of wave transmission coefficients from finite element metaconcrete slab models

Transmission coefficients have been used to identify the band gap properties of both photonic (Sigalas et al., 1993; Smith et al., 1993, 1994) and acoustic crystals (Sánchez-Pérez et al., 1998; Liu et al., 2000b; Sheng et al., 2003). For sonic metamaterials using layered resonant inclusions, the change in sound wave amplitude across the crystal was measured experimentally to give the transmission ratio for a chosen wave frequency (Liu et al., 2000b; Sheng et al., 2003). A similar ratio can be computed for metaconcrete by considering the amount of mechanical energy transmitted through a slab. This ratio is plotted against input frequency to investigate which ranges of frequency correspond to reduced wave transmission and to ascertain whether this effect is caused by the activation of resonance.

3.2.1 Finite element model
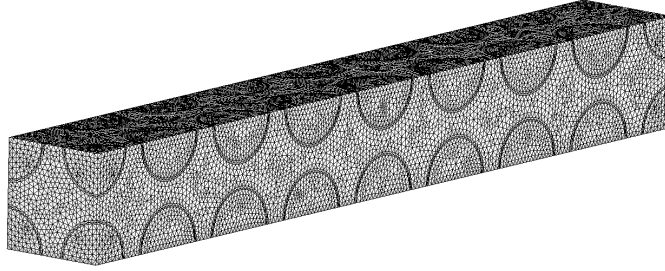
Figure 3.10: Finite element mesh with a fine discretization (mesh size $h = 1.5$ mm) for a metaconcrete slab containing an array of aggregates with a 1 mm coating.

To investigate the transmission of wave energy we employ the finite element model described in Chapter 2. We consider a rectangular section of an infinite planar slab containing a periodic array of metaconcrete aggregates. The solid model is discretized with the fine mesh, i.e., of size $h = 1.5$ mm, described in Chapter 2. An example of the fine discretization finite element mesh for an array of 1 mm coated aggregates is shown in Figure 3.10. We can check the maximum allowable applied wave frequency that can by calculated using this mesh by considering the maximum wavenumber q_{max}, computed using the mesh size h,

$$q_{max} = \frac{1}{h}.$$ (3.36)

We obtain the equation for maximum frequency f_{max}, by multiplying the maximum wavenumber by the longitudinal wave speed of the material c_L,

$$f_{max} = \frac{c_L}{h}.$$ (3.37)

If we consider the longitudinal wave speed for the homogeneous mortar material $c_L = 3464$ m/s, given by $c_L = \sqrt{E/\rho}$, we compute the approximate maximum allowable frequency as $f_{max} = 2309$ kHz.

The chosen dimensions for the slab are $L = 0.24$ m and $b = 0.03$ m, with a periodic arrangement of aggregates at 0.03 m centers. This gives a total of 8 whole spherical central inclusions and 28 quarter spheres around the longitudinal edges of the slab. Each aggregate has an outer diameter of 24 mm and contains a central lead core.

In the study of wave transmission, we consider the four aggregate configurations listed in Table 3.1. In addition, we consider two periodic aggregate arrays. First, the slab is configured with a total of 8 aggregates in a periodic arrangement along the center of the slab. The simulations are then run again with a more densely packed configuration, this time also including the 28 quarter spheres surrounding the outer edges of the slab, giving a total of 36 separate inclusions. A mortar slab with no inclusions is analyzed as a baseline comparison. The material properties, geometry, and resonant frequencies for each of these configurations are presented in Section 2.1 of Chapter 2, and the volume fractions and descretization data are provided in Section 2.2 of Chapter 2.

We consider purely elastic behavior for all components, with the material behavior described by a neo-Hookean material model, extended to the compressible range, see Appendix A. The forcing function is generated by applying a sinusoidal displacement to all nodes on one end face of the slab at a prescribed frequency. The other end face is unconstrained, and we apply periodic boundary conditions to the lateral faces of the slab. To have the same input energy for every harmonic wave frequency, we scale the amplitude of the applied displacement relative to a reference resonance value. The energy of a harmonic wave is proportional to the square of both the frequency and the amplitude of the wave, i.e.,

$$\mathbb{E} \propto \omega^2 A^2. \tag{3.38}$$

To maintain the same input energy for a frequency other than the resonant value, we therefore multiply the reference amplitude by f_r/f, the ratio of the resonant frequency relative to the frequency value under consideration. For example, an amplitude of $A_r = 0.001$ m was chosen for the reference critical frequency equal to the resonant frequency of the inclusion. The amplitude for a subcritical frequency $f_1 = 0.25 f_r$ is therefore $A_1 = 0.004$ m, and similarly, the amplitude for a supercritical frequency $f_2 = 2 f_r$ is $A_2 = 0.0005$ m.

The amount of energy trapped within the metaconcrete aggregates is averaged over a total fixed time duration for each configuration. We begin computation of the transmission ratio after the greater of either one period of the harmonic forcing function or the time it takes for approximately two transits of a wave through a homogeneous slab. The transit time for the wave to travel once through the length of the slab is given by $t_L = L/c_L$, where L is the length of the slab and $c_L = 3464$ m/s is the longitudinal wave speed of mortar, given previously. For the homogeneous mortar slab under consideration this gives $t_L = 7 \times 10^{-5}$ s

and a minimum time $2t_L = 1.4 \times 10^{-4}$ s. The end time for the simulation is chosen based on the aggregate configuration and is given by $t_{total} = 0.0004$ s for the 1 mm nylon coated aggregates, $t_{total} = 0.0005$ s for the 3 mm nylon coated aggregates, $t_{total} = 0.0011$ s for the 1 mm rubber coated aggregates, and $t_{total} = 0.0018$ s for the 3 mm rubber coated aggregates. The time interval for averaging is chosen so that there is a minimum of two transits of the applied wave through the slab, with an average of 15 cycles of the applied displacement over the duration of the calculation. This allows sufficient time for resonance activation of the aggregates while preventing any build-up of numerical interference.

To compute the transmission coefficient we consider the amount of energy that is trapped by the aggregate farthest away from the applied loading and compare this to the behavior of the entire slab. This indicates how much energy reaches the far end of the slab and therefore how much energy has been distributed and absorbed by the aggregates during the transition of the wave. The transmission coefficient T is therefore given by the ratio of the amount of energy trapped in the last aggregate relative to the total energy trapped within all the aggregates of the slab,

$$T = \frac{\mathbb{E}^N}{\sum\limits_{j=1}^{N} \mathbb{E}^j}, \tag{3.39}$$

where $\mathbb{E}^j$ is the total mechanical energy of the j-th aggregate, time-averaged over the duration of the calculation, and N is the total number of aggregates, where the aggregate furthest from the exposed face is denoted by $j = N$. A decrease in transmission coefficient therefore implies that less energy has reached the final aggregate and thus activation of the inclusions has resulted in a behavior that absorbs energy from the applied wave.

3.2.2 Transmission plots for four aggregate configurations

The transmission ratio is computed from the results of the finite element analyses using the model and material properties described in the previous section. Both the 8 and 36 aggregate array configurations are tested for each model with the same range of applied wave frequencies, varying between 4-139 kHz for the 1 mm nylon coated inclusions, 5-100 kHz for the 3 mm nylon coated inclusions, 2-37 kHz for the 1 mm rubber coated inclusions, and 1-22 kHz for the 3 mm rubber coated inclusions. Each frequency range is chosen so that any behavior near the four modes of vibration given in Table 2.5 of Chapter 2 can be fully captured. In addition, the maximum frequency considered is selected to be significantly smaller than the maximum allowable frequency computed from Eq. (3.37).

The resulting plots for the two cases of nylon coated lead inclusions are shown in Figure 3.11. The plot for the 1 mm nylon coated inclusions, shown in Figure 3.11(a), displays a low frequency dip in transmission coefficient at 22 kHz for both the 8 and 36 aggregate arrays. This dip occurs near the approximate resonant frequency of 17.4 kHz calculated from the one–dimensional spring–mass system (Eq. (2.5) of

Chapter 2) and at the Mode 2 resonant frequency of 21.12 kHz computed with the modal analysis.

The low frequency decrease in energy transmission ratio observed in Figure 3.11(a) also corresponds with the bad gap frequency range found for the equivalent one–dimensional spring–mass model of Section 3.1.3, where the bad gap was found to lie between 16.1 kHz and 26.3 kHz. Due to the nature of the one–dimensional spring–mass system, only one mode of resonant behavior can be modeled and therefore we note that the system cannot capture any of the higher mode band gaps that may be present in the finite element transmission analysis.

The transmission plot also displays a second dip at a higher frequency of 35 kHz, which corresponds approximately to the Mode 3 and 4 frequencies found from the modal analysis. This dip is slightly greater in magnitude and wider in frequency range, which indicates that vibration and oscillation of the core and coating at higher frequencies produces a greater reduction in transmission. However, a distinct dip is only apparent for the 36 aggregate case and a significant drop in transmission ratio is not seen when fewer aggregates are present in the slab. A further decrease at very high frequencies greater than approximately 78 kHz is also observed. The high-frequency decrease in transmission coefficient seen in Figure 3.11(a) is possibly due to the periodic arrangement of aggregates combining to provide amplification of the energy absorption properties, a Bragg-type scattering of the waves caused by the applied wavelength nearing the aggregate spacing and dimensions, improved performance at higher modal frequencies, or numerical interference.

We observe an improvement in transmission ratio when we compare the results of the metaconcrete configurations to that achieved with a homogeneous mortar slab. The transmission coefficient for the homogeneous slab is independent of the frequency of applied loading, maintaining a value of 0.13 over the entire frequency range for all cases. The low frequency dip for the 1 mm nylon aggregate case at 22 kHz displays a magnitude that is 3.0% of the transmission coefficient of the homogeneous mortar slab for both aggregate configurations. The second low frequency dip for the 36 aggregate arrangement occurs at 35 kHz, with 2.2% of the mortar value. This improvement over the homogeneous mortar slab suggests enhanced performance within the range of frequencies corresponding to the dips.

We see similar behavior for the 3 mm nylon aggregate case, shown in Figure 3.11(b). A sharp dip for both array configurations is located at the Mode 2 natural frequency of the aggregate, 15.94 kHz. The magnitude of this dip is 3.2% of the homogeneous mortar slab coefficient, thus achieving a similar Mode 2 dip magnitude to the 1 mm nylon case. Like the 1 mm nylon aggregate case, we also observe a higher frequency dip for the 36 aggregate configuration located near the Mode 3 and 4 natural frequencies, along with a drop in transmission coefficient at very high frequencies greater than 60 kHz.

In this case, the one–dimensional model from Section 3.1.3 underestimates the location of the first transmission dip. The band gap from the one–dimensional model spanned the range between 10.9 kHz and 14.5 kHz, thus covering the lower section of the dip location in Figure 3.11(b); however, the one–dimensional approximation does not capture the higher frequency part of the attenuation band.
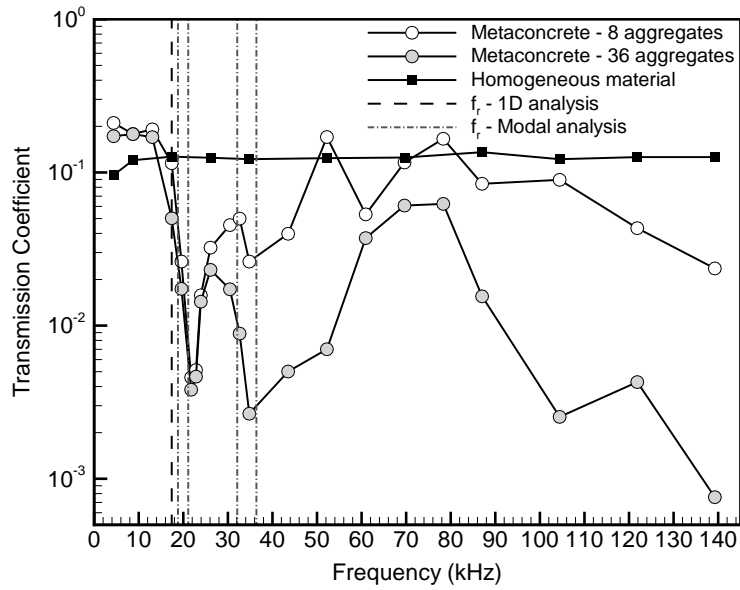
(a) 1 mm nylon coated lead aggregates
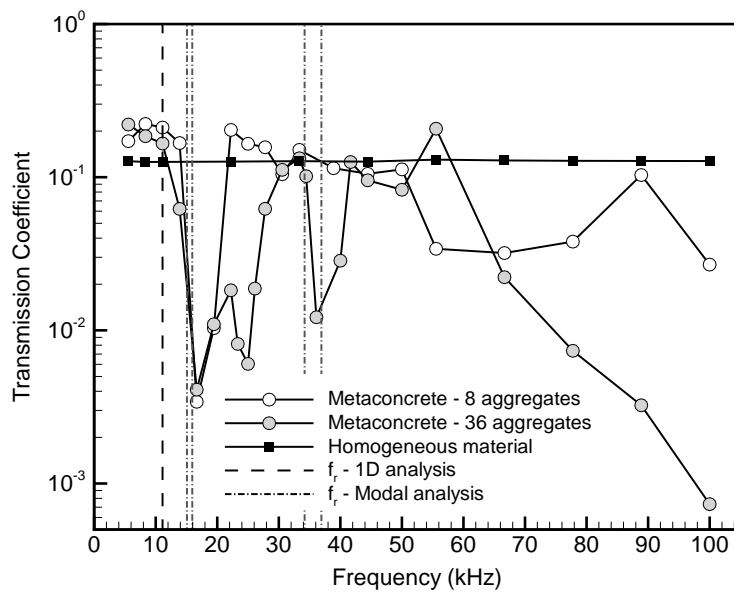
(b) 3 mm nylon coated lead aggregates

Figure 3.11: Transmission coefficient plotted against frequency of excitation for a metaconcrete slab consisting of (a) 1 mm and (b) 3 mm nylon coated aggregates. Also shown are the corresponding transmission coefficients for a homogeneous slab along with the resonant frequencies f_r of the inclusion from both the approximate one–dimensional equation and the modal analysis.
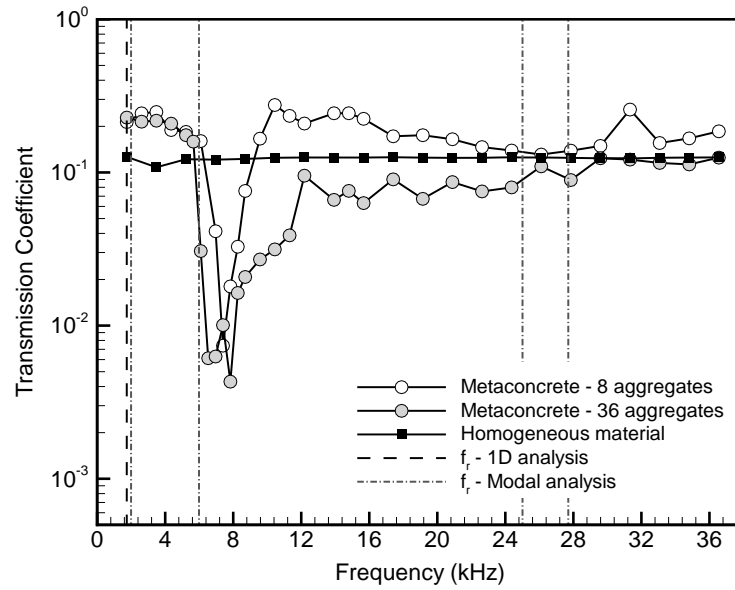
(a) 1 mm rubber coated lead aggregates
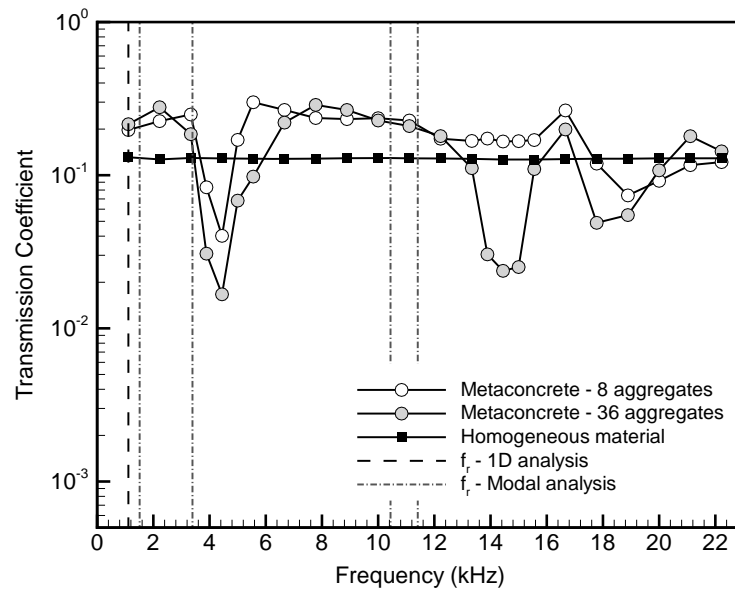
(b) 3 mm rubber coated lead aggregates

Figure 3.12: Transmission coefficient plotted against frequency of excitation for a metaconcrete slab consisting of (a) 1 mm and (b) 3 mm rubber coated aggregates. Also shown are the corresponding transmission coefficients for a homogeneous slab along with the resonant frequencies f_r of the inclusion from both the approximate one–dimensional equation and the modal analysis.

The results for the two rubber coated aggregate configurations are shown in Figure 3.12. The 1 mm rubber coated aggregregate case, shown in Figure 3.12(a), displays a dip located in the range of 6-10 kHz, which corresponds to the Mode 2 natural frequency of 5.99 kHz as computed by the modal analysis. This dip occurs for both the 8 and 36 aggregate configurations and reaches 3.5% of the homogeneous mortar value, although the apparent band gap is wider when there are more aggregates present in the slab. For either array configuration case, we do not observe a second dip at higher frequencies near the Mode 3 and 4 values. Instead, the transmission ratio sits near that of the homogeneous mortar slab, indicating a lack of improved performance at higher frequencies for the case where a thin 1 mm rubber coating is used.

By contrast, the transmission plot for the 3 mm rubber coated aggregates, shown in Figure 3.12(b), displays three distinct dips in transmission coefficient, most particularly for the 36 aggregate arrangement. The first dip occurs in the frequency range of 3.5-5.5 kHz and is present for both the 8 and 36 aggregate cases, achieving a minimum of 13.0% of the homogeneous slab transmission value. The second dip is present only in the 36 aggregate configuration and occurs in the range of 14-16 kHz, reaching 18.8% of the homogeneous mortar value. The third dip is present for both aggregate array configurations and occurs in the range of 17-21 kHz. Only the first dip corresponds directly to the natural frequency computed with the modal analysis, occuring near the Mode 2 natural frequency of 3.39 kHz. The second and third dips are greater than 3 kHz higher than the fourth Mode natural frequency, suggesting they are generated by some higher mode combination of coating and core oscillation within the aggregate.

The three gaps observed in the transmission plot in Figure 3.12(b) for the 3 mm rubber case are more distinct than any other configuration of coating material and thickness. However, the magnitude of the dips are much smaller and the gaps are narrower, or in the case of the 8 aggregate configuration, barely present. Furthermore, the shape of the gaps present in Figure 3.12(b) also resemble the form of the measured amplitude transmission found in the experiments conducted by Liu et al. (2000b) and Sheng et al. (2003) on sound waves in locally resonant sonic crystals. Sound wave transmission was tested using an array of 15 mm diameter inclusions with 2.5 mm silicone rubber coated lead cores. These inclusions are of similar configuration to those tested in the metaconcrete slab and the transmission coefficient plots produced from experiments on sonic crystals of this structure display a similar trend; two distinct dips in transmission coefficient with frequency locations corresponding to those calculated from theoretical analyses.

For the rubber coated aggregates we also note that there are large ranges in frequency for which the plots indicate that metaconcrete performs the same or worse than the homogeneous concrete slab; the transmission coefficient sits above the line of the reference homogeneous value. In contrast, the aggregates with the comparatively more stiff nylon coating perform, in general, better than the concrete slab over large spans of frequency within the range under investigation.

The one–dimensional metaconcrete slab approximation from Section 3.1.3 displays a band gap near the one–dimensional estimate of the resonant frequency. As a consequence, the one–dimensional ap-

proximation therefore underestimates the location of the transmission attenuation band, predicting much lower frequencies than seen in Figure 3.12. However, the one–dimensional model did predict a significantly smaller band gap range for the rubber coated aggregates when compared with the nylon coated configurations, and this trend was observed in the energy transmission results calculated using the finite element model.

3.3   Summary

We present a numerical investigation of the transmission behavior of four metaconcrete slab configurations for a range of forcing frequencies. Dispersion relations are derived from a one–dimensional approximation of a metaconcrete slab, using mass–in–mass resonators within a spring–mass chain. These relations display band gaps and large attenuation of wave transmission near the aggregate resonant frequency. Within the band gap frequency range, the transition to negative effective mass causes the mass representing the aggregate core to move out of phase with the equivalent one–dimensional mortar matrix mass. The high amplitude contrast between the two masses combined with the antiphase behavior leads to large energy absorption within the aggregate and attenuation of the applied wave.

To further investigate the frequency–dependent nature of metaconcrete, a finite element model is used to compute the transmission coefficients for metaconcrete slabs over a range of forcing frequencies. The transmission coefficients are computed based on the amount of energy transmitted through the slab, where the average energy absorbed by the last aggregate was compared to that of all the aggregates. The transmission coefficient plots indicate the existence of bands of reduced energy transmission within the frequency spectrum and also suggest a frequency range for which a particular aggregate configuration provides the most beneficial behavior. For each of the four cases, the most significant dip in transmission coefficient is achieved near the Mode 2 natural frequency computed by the modal analysis, which corresponds to the rigid body translation resonant frequency of the inclusion. This dip is present for both 8 and 36 aggregate configurations, with both aggregate arrays achieving the same dip magnitude in the Mode 2 range in three out of four cases. For the nylon coated inclusion, this gap is given by frequencies within the range of approximately 20-60 kHz for the 1 mm coated aggregates and 13-30 kHz for the 3 mm coated aggregates. For the more compliant rubber coating, the Mode 2 gap is present in the range of 6-9 kHz for the 1 mm coated aggregates and 3.5-5.5 kHz for the 3 mm coated aggregates. The density of the aggregates within the slab was also seen to affect the magnitude of the dip in transmission coefficient, with a larger number of aggregates per unit volume leading to a wider frequency range of influence. Of the two cases, aggregates with the more stiff nylon coating provide a greater dip in wave energy transmission over a larger range of applied frequencies.

The understanding gained from the location and size of of the wave attenuation frequency bands for each inclusion configuration can be further utilized in the design of metaconcrete aggregates for loading

applications where attenuation of dynamic excitation with a specific frequency profile is desired.

Chapter 4

Metaconcrete and shock mitigation

To further explore the dynamic behavior of metaconcrete we now consider slab performance under the action of a blast wave caused by the ignition of an explosion. We utilize the finite element model described in Chapter 2, and apply a blast wave loading to the exposed end of the slab, which activates a wide range of frequencies. We will show that the mechanical behavior of metaconcrete differs from that of regular concrete. Resonant aggregates are able to trap a portion of the supplied energy through the activation of localized oscillatory motions, which is characterized by an exchange of elastic and kinetic energy between the stiff core and soft outer coating. The global effect is to reduce the amount of energy and stress within the mortar phase of the slab, enhancing the slab's ability to sustain the applied dynamical actions without damage. We investigate a range of different aggregate and geometry configurations and consider how changes in local resonant behavior effect slab performance. The insight gained from this analysis will help to build on the understanding of general transmission and band gap characteristics outlined in Chapter 3, suggesting optimal design configurations for the mitigation of shock waves in blast wave loading applications.

4.1 Energy time histories

To investigate blast wave loading of metaconcrete, we utilize the finite element slab model with the coarse element mesh described in Section 2.2.1 of Chapter 2. The blast wave loading is generated using the model outlined in Section 2.2.2 of Chapter 2, with an explosion yield factor of $\lambda = 0.01$. Further details are provided in Appendix B. We consider the aggregate and geometry configurations described in Section 2.1 of Chapter 2, using only the high–density 36 aggregate arrangement. This allows us to explore how the different aggregate configurations, and therefore resonant frequencies, affect energy transfer and stress distribution within the slab.

We begin by providing a qualitative illustration of the behavior of metaconcrete when subject to a blast excitation. As an illustrative example, we first consider a metaconcrete slab consisting of nylon coated inclusions of the configuration denoted A in Table 2.2 of Chapter 2. We analyze this alongside a homogeneous slab with the effective properties of concrete, which provides a baseline for comparison. We evaluate the two materials using the energy time history, which is shown in Figure 4.1(a) for the case

(a) Homogeneous Material

(b) Metaconcrete
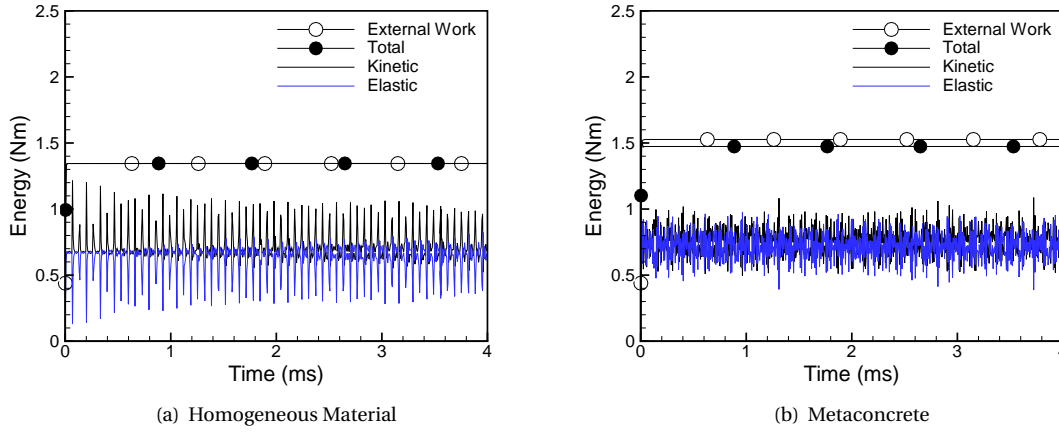
Figure 4.1: Global system energy history: supplied energy (white circles), kinetic energy (black line), elastic energy (blue line), and total mechanical energy of the system (black circles).

of the homogeneous material, and Figure 4.1(b) for the chosen metaconcrete slab configuration. In these figures, black lines denote the total kinetic energy, blue lines the total elastic energy, black circles the total mechanical energy, and white circles the energy supplied to the system. The supplied energy is given by the external work done by the pressure forces on the impacted surface, or

$$W^{\text{ext}} = \int_0^t \int_{A_{\text{exposed}}} p(t) \, du(t) \, dA, \tag{4.1}$$

where $du(t)$ is the incremental displacement component normal to the exposed area. Note that the amount of supplied energy differs depending on the configuration chosen for the metaconcrete and according to the choice of soft coating material. Since the applied force is equal, the difference is due to the magnitude of the displacement at the exposed surface. Figure 4.1 shows clearly that the system is conservative; the supplied energy provides the total mechanical energy and a continuous exchange between kinetic and elastic energy is observed during the process.

Details concerning the partition of the energy between the three components of the metaconcrete system can be observed in Figure 4.2. The plots show the time histories of the mechanical, kinetic, and elastic energy for each component of the system. Black lines denote the energy carried by the mortar, blue lines the energy carried by the compliant coating, and red lines the energy carried by the lead cores. The energies are expressed with respect to the total mechanical energy of the system. For the configuration of metaconcrete considered, Figure 4.2(a) shows that approximately 60% of the total mechanical energy is carried by the heavy lead cores, while the mortar carries only 30%. Figure 4.2(b) shows that the elastic energy in the mortar and in the compliant coating is only one third of the elastic energy in the lead cores, which undergo elastic oscillations. Figure 4.2(c) shows that a large amount of kinetic energy remains

(a) Mechanical Energy

(b) Elastic Energy
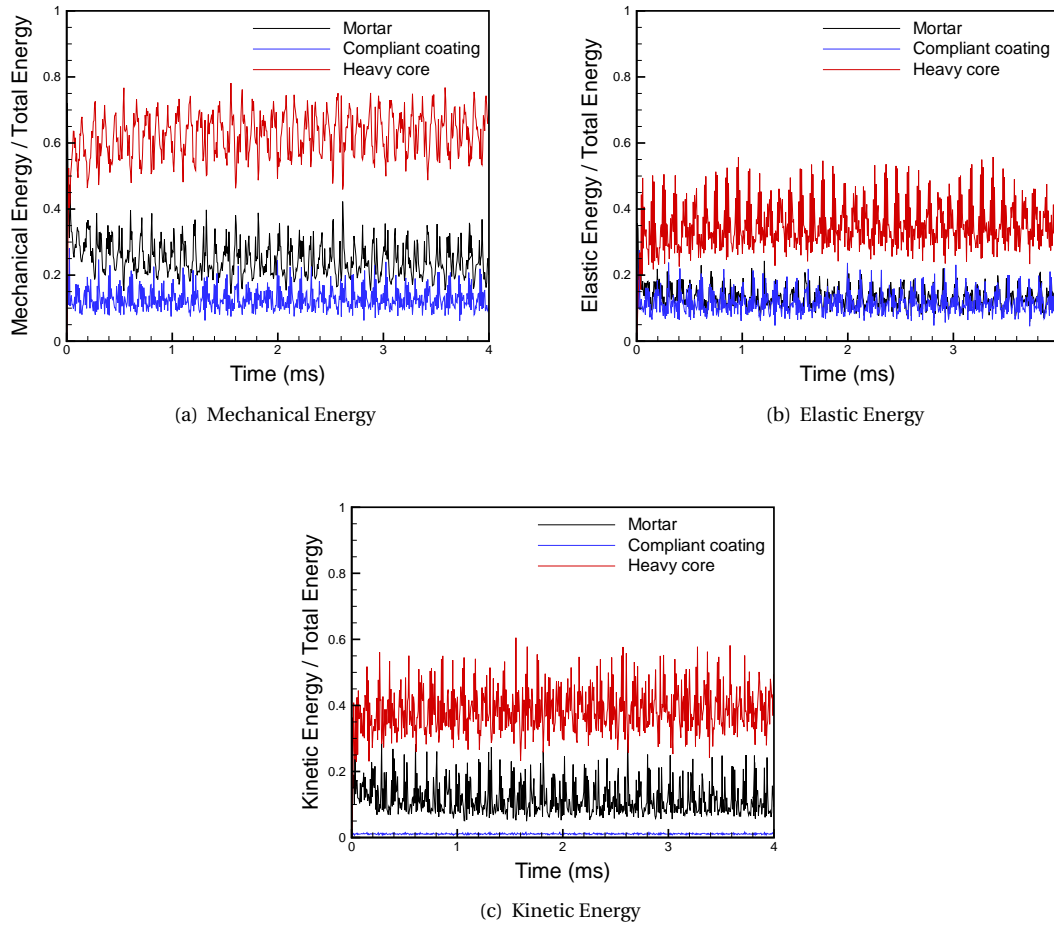
(c) Kinetic Energy

Figure 4.2: Fractions of mechanical, elastic and kinetic energy carried by the three components of the metaconcrete slab, expressed with respect to the total mechanical energy of the system.

trapped in the heavy lead cores.

Comparison of the plots suggests the presence of oscillatory motion of the lead cores inside the aggregates. The large amount of kinetic and elastic energy absorbed by lead core of the aggregates can be related to the resonant behavior seen in the analysis of transmission characteristics. This absorption of energy is caused by the activation of resonant or near–resonant behavior within the aggregates, which in Chapter 3 was found to lead to higher–amplitude antiphase motion within the negative–mass frequency band. This suggests that the resonant behavior of this aggregate configuration is activated by the chosen blast loading profile, leading to a reduction in mechanical energy within the mortar phase.

We further investigate the trapping of energy within the aggregates in the following section, by considering the energy distribution and energy density for other aggregate material and geometry configurations.

4.2 Influence of aggregate properties on slab energy distribution

We perform a parametric study of the mechanical behavior of metaconcrete by varying the material properties and geometry of the compliant coating. We investigate the five aggregate coating and three aggregate geometries presented in Section 2.1 of Chapter 2. The results of the analyses are presented in terms of the distribution of kinetic, elastic, and mechanical energies between the three phases of the metaconcrete slab.

(a) Mechanical Energy

(b) Mortar Energy Density

(c) Mortar Elastic Energy Density

(d) Mortar Kinetic Energy Density
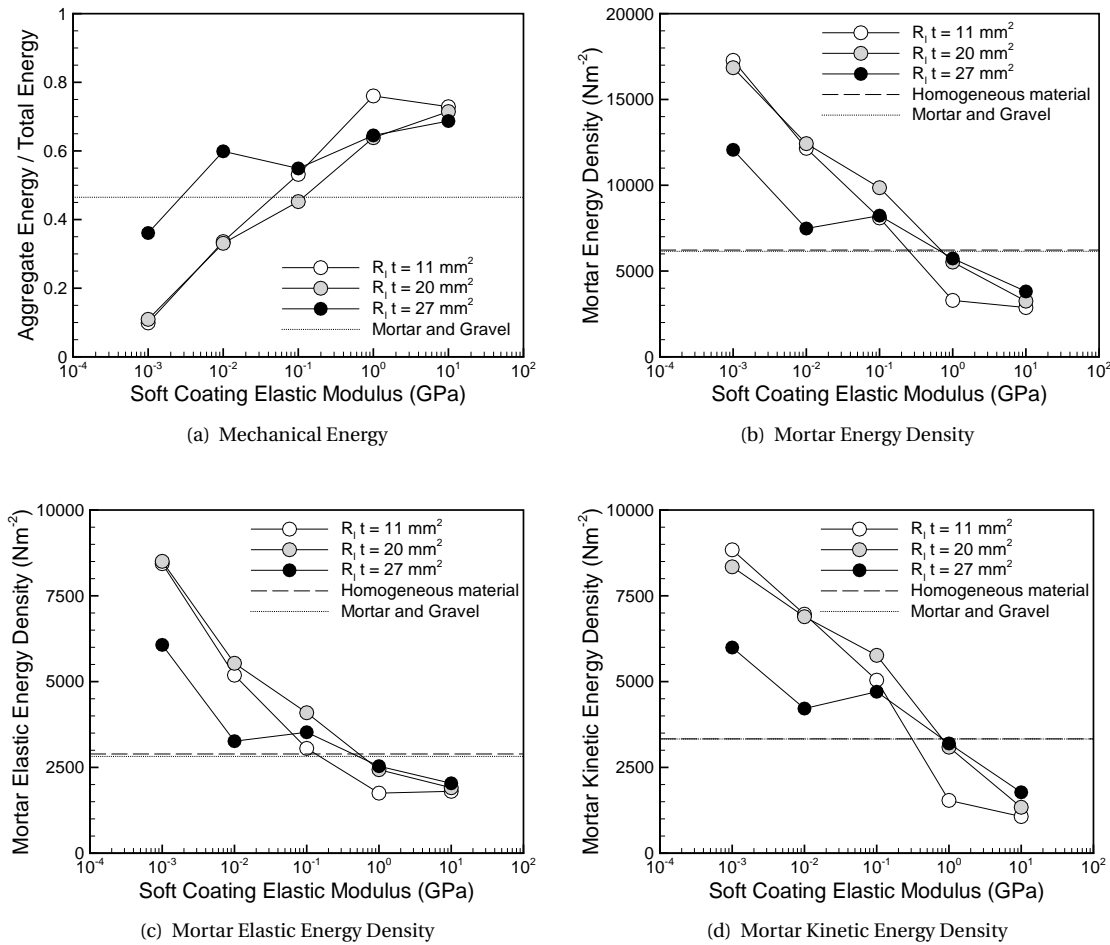
Figure 4.3: Parametric study by varying the compliant coating thickness and elastic modulus. (a) Fraction of the total mechanical energy captured by the aggregates; (b) Average energy density of the mortar; (c) Average elastic energy density of the mortar; (c) Average kinetic energy density of the mortar. For each case, the results obtained using an equivalent homogeneous slab and a mortar and gravel slab are also shown for comparison.

Figure 4.3(a) shows the fraction of mechanical energy captured by the aggregates as a function of the elastic modulus of the soft coating. Each line refers to a different aggregate geometry. As the elastic modulus of the coating material is increased, each aggregate configuration displays an increase in trapped energy. This indicates that propagating shock wave energy caused by the blast loading is captured by the

aggregates, and as a result, removed from the mortar matrix material. The same trend is present for all three aggregate geometry configurations, with the 1 mm nylon coated aggregate achieving the highest fraction of aggregate energy of all the cases considered.

The fraction of energy trapped in a equivalent aggregate volume of gravel in a mortar slab is also plotted in Figure 4.3(a) to provide a baseline for comparison. These aggregates assume the properties of gravel or stone, as used in standard concrete, utilizing the same positioning and spherical shape as the metaconcrete aggregates. The material properties used for the gravel aggregates are $\rho = 2700$ kg/m^3, $E = 50$ GPa, and $\nu = 0.25$. From Figure 4.3(a) we see that the fraction of the total energy captured by the aggregates with the three highest elastic moduli is larger than that trapped by the equivalent gravel aggregates in a gravel and mortar slab. This indicates that the layered resonant aggregates with higher coating stiffness can trap a larger proportion of the energy supplied from the blast wave.

The aggregate energy can also be presented in terms of aggregate resonant frequency, which is shown in Figure 4.4. The scatter plot reveals that aggregates with resonant frequencies above 4 kHz absorb a greater amount of energy than that found for the mortar and gravel case, for all three of the geometry configurations considered. Aggregates with resonant frequencies below this value absorb significantly less energy, as low as 10% of the total mechanical energy for configurations with the lowest resonant frequency. Above 10 kHz, increasing the resonant frequency causes very little, if any, increase in the energy absorbed by the aggregates. This implies that aggregates in this range are activated by the applied blast wave loading and that once an aggregate has transitioned to resonant behavior a similar fraction of the total energy is absorbed for all cases.
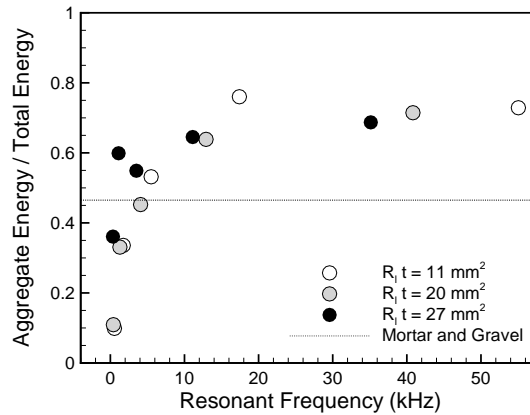
Figure 4.4: Fraction of mechanical energy absorbed by the metaconcrete aggregates, plotted against the aggregate resonant frequency computed from the one–dimensional model for each aggregate configuration.

To see the changing distribution of energy among the slab constituents as the aggregate properties are varied, we plot the mechanical energy for each slab component for three cases, shown in Figure 4.5. We consider only the 1 mm aggregate geometry and choose three different coatings covering the range of

elastic moduli under investigation: silicone, low density polyethylene, and urea formaldehyde.

(a) 1 mm silicone coating

(b) 1 mm LDPE coating

(c) 1 mm urea formaldehyde coating
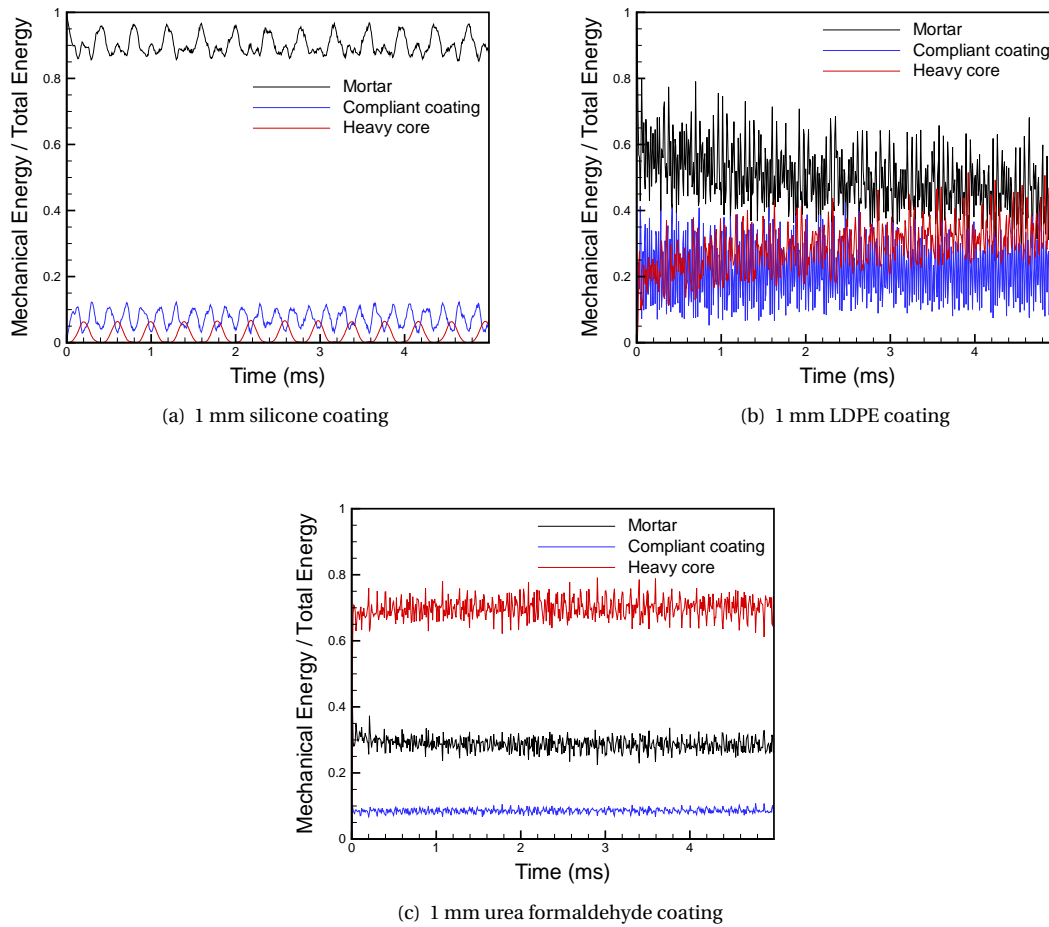
Figure 4.5: Mechanical energy distribution for three slab cases: (a) 1 mm silicone coated aggregates, (b) 1 mm low density polyethylene coated aggregates, and (c) 1 mm urea formaldehyde coated aggregates.

For soft coatings, such as the silicone coating shown in Figure 4.5(a), the mechanical energy is distributed so that the mortar phase accounts for approximately 90% of the total energy, with the coating and core materials absorbing the remaining 10%. This indicates that aggregates with a soft coating are not activated by the chosen blast loading, and therefore their energy trapping properties are not utilized, causing the aggregate energy to be much lower, as seen in Figure 4.3(a). As the coating elastic modulus is increased the behavior starts to transition, where the fraction of energy trapped within the aggregates begins to increase. This is seen in Figure 4.5(b) for the low density polyethylene coated aggregate, where the fraction of energy present within the mortar phase starts to decrease, and the energy trapped within the core and coating of the aggregates increases. Finally, at the highest coating stiffness considered, the urea formaldehyde coating shown in Figure 4.5(c), the behavior has fully transitioned and the aggregate core now absorbs the largest portion of the mechanical energy. This indicates that inclusions with coat-

ings of higher stiffness display resonant or near-resonant behavior, leading to energy trapping within the aggregates.

We explore this further by considering the mortar energy density, which is the average mechanical energy in the mortar material divided by the mortar volume, see Figure 4.3(b). The elastic and kinetic energy components of the mortar energy density are shown in Figure 4.3(c) and Figure 4.3(d), respectively. The plots display a distinct trend which corresponds with that found for the aggregate energy; as the coating elastic modulus is increased, the mortar energy density decreases. This suggests the energy is transferred away from the mortar matrix and trapped within the metaconcrete aggregates.

Lines representing the energy density for both a homogeneous mortar slab and a mortar and gravel slab are also shown in Figures 4.3(b)-4.3(d). These lines are in an almost identical location, showing no difference in mortar energy density. We see that the two coatings with the highest stiffness produce mortar energy densities below the corresponding values for the homogeneous or gravel slabs.

The distribution of energy for the different aggregate configurations shows that, in order to transfer energy from the mortar to the heavy cores, it is necessary to have a coating softer than the other two phases but still stiff enough to transfer some stress. Very soft coatings (such as silicone, natural rubber, or low density polyethylene) do not lead to resonance behavior in the presence of the chosen blast loading, causing the heavy core to be excluded from the dynamic behavior of the metaconcrete slab. As a consequence, this results in a reduction in the global stiffness of the system, and therefore, at an equal blast force, the material deforms more and the supplied energy is higher. In these cases, the performance of the metaconcrete can be considered inferior to that of a homogeneous concrete slab, as shown by the first three points in Figure 4.3(b). When the stiffness of the soft material is comparable to the stiffness of both the lead and mortar phases, the metaconcrete works as a whole and exhibits attenuation of the propagating shock wave, due to trapping of the energy within the resonant cores.

4.3 Influence of aggregate properties on slab stress distribution

Further insight into the resonant and energy trapping behavior of metaconcrete aggregates can be revealed by studying the longitudinal stress distribution along the surface of the mid-longitudinal cross-section of the slab. Figure 4.6 compares the stress distribution 0.05 ms after the beginning of the blast in a homogeneous material along with two metaconcrete slabs; one containing 1 mm silicone coated aggregates and the other containing 1 mm nylon coated aggregates. The blast pressure acts on the left end section of the slab, and lasts for less than 0.01 ms. The stress profile captures the first transition of the compressive shock wave through the depth of the slab. In the figure, blue shades denote compression and the red shades denote tension.

In the homogeneous material, shown in Figure 4.6(a), the initial shock wave travels at the velocity of the longitudinal wave speed, maintaining a regular planar shock front structure. In the metaconcrete

slabs, however, the shock front propagates at lower speed, delayed in time most significantly when the aggregates are activated. The metaconcrete slab containing 1 mm silicone coated aggregates, seen in Figure 4.6(b), shows that little or no stress enters the aggregate constituents. Instead, the shock wave stress travels around the aggregates, concentrated in the mortar matrix material. This indicates that no resonant or energy absorbing properties are present, as expected from the energy analyses in the previous section.

By contrast, the slab containing 1 mm nlyon coated aggregates, presented in Figure 4.6(c), shows a significant amount of stress is concentrated inside the aggregates themselves. In this configuration, the stress wave is significantly delayed in time and the magnitude of the stress in the matrix material appears to be less. The average magnitude of the longitudinal stress also reduces with the distance from the blasted surface. The aggregates in this slab are subject to elastic oscillations, which can be observed in the left side of Figure 4.6(c). The resonant behavior can be seen in the second inclusion from the left; the center of the lead core displays compressive stresses while the annular region surrounding the core displays tensile stresses.

(a) Homogeneous material

(b) 1 mm silicone coated lead aggregates

(c) 1 mm nylon coated lead aggregates
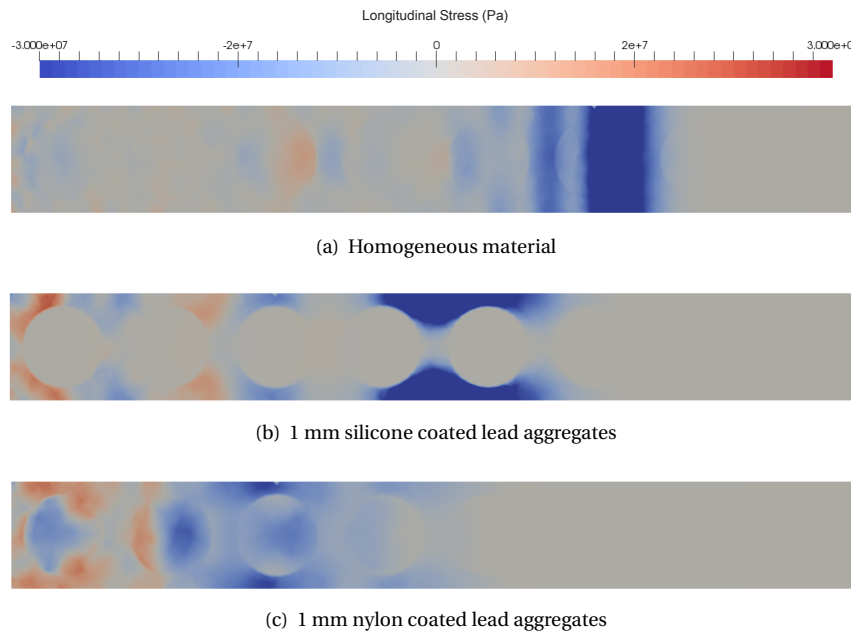
Figure 4.6: Comparison of the distribution of longitudinal stress at $t = 0.05$ ms for (a) a homogeneous mortar slab (maximum 59 MPa compression, 28 MPa tension), (b) a metaconcrete slab containing 1 mm silicone coated inclusions (maximum 86 MPa compression, 21 MPa tension), and (c) a metaconcrete slab containing 1 mm nylon coated inclusions (maximum 29 MPa compression, 28 MPa tension). Blue shades denote compression, red shades denote tension.

An assessment of the stress profile for each of the different configurations can be made by considering the maximum longitudinal tensile and compressive stresses present in the mortar matrix of the slab. Lower stresses in the mortar phase suggest improved slab performance, as this indicates the slab will be

less susceptible to brittle behavior or fracture processes that are typical of mortar–like materials. The stress in the section of slab nearest to the blast exposed face cannot be reduced, however, it is likely that the magnitude of the stress induced in the mortar reduces progressively with distance from the exposed face. Therefore, we consider the maximum stresses in both the full slab and the half slab furthest from the blast site.
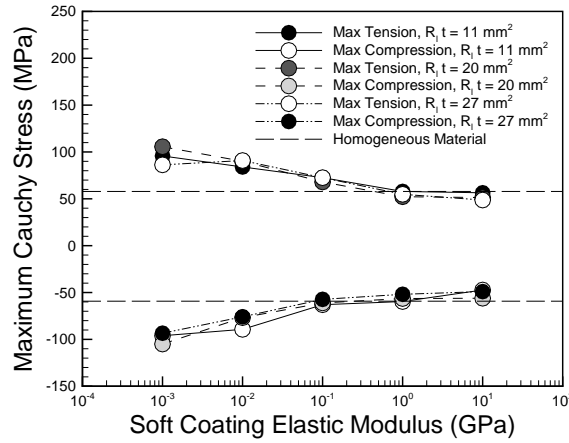
(a) Full length
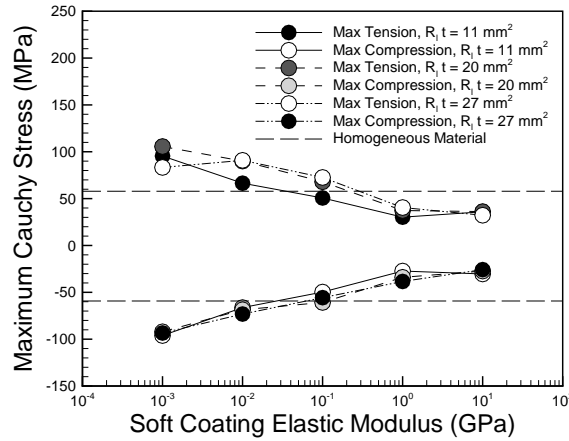
(b) Half slab

Figure 4.7: Maximum and minimum longitudinal Cauchy stress in the mortar matrix of the metaconcrete slab, as a function of the soft coating elastic modulus. (a) Stresses in the full length of the slab. (b) Stresses in the half slab furthest from the blast face.

Figure 4.7(a) shows the maximum tensile and compressive longitudinal stress observed in the mortar of the full slab over the entire duration of the dynamical analysis. The maximum longitudinal stress in the mortar reduces with increasing compliant coating stiffness. In the case of urea formaldehyde, the maximum longitudinal stress is half of the stress computed for the silicone coating. It is also seen that the

maximum longitudinal stress is slightly lower than that obtained for the homogeneous mortar slab when coatings with higher stiffness are used.

The stress reduction is more evident when we consider only the right half of the slab, furthest from the blast site, see Figure 4.7(b). In this region, the maximum stress evaluated for the urea formaldehyde coating reduces to a quarter of the stress computed for the silicone coating. The maximum tensile and compressive stresses are also significantly lower than the homogeneous mortar value for the two highest coating elastic moduli, reducing to around $45-60\%$ of the mortar value. Therefore, we can ascertain that the main advantage of the layered resonant aggregates is to reduce the amount of energy transmitted through the depth of the slab perpendicular to the blast face and, consequently, the magnitude of the stress in the mortar phase.

4.4   Summary

In this chapter we consider the energy and stress distribution in metaconcrete slabs subjected to a blast wave loading profile. A numerical analysis of a range of coating and aggregate configurations reveals that oscillatory behavior within the aggregates may be activated by the chosen blast loading, indicated by an increase in aggregate energy. The aggregates with higher coating elastic moduli are able to absorb a consistent fraction of the mechanical energy, reducing the total energy and stress within the mortar matrix of the slab. The numerical results show that, under dynamic excitation, metaconcrete behaves in a rather different way to an equivalent homogeneous slab with the effective properties of concrete. The most prominent effect is the reduction in the amount of energy transmitted across the system and, as a result, the reduction of stress within the brittle phase, i. e., the mortar.

In the numerical calculations, we considered three heavy core radii and three coating thicknesses. However, in the results obtained, we do not observe a strong dependence of the mechanical response on these geometrical parameters. Our results show that the most important parameter is the elastic modulus of the soft coating. This outer layer to the heavy core must be more compliant, although of comparable stiffness, to the mortar and lead components. Only under these conditions is the compliant coating layer able to transfer the mechanical energy contained in the mortar to the heavy cores and, as a result, activate elastic oscillations inside the resonant aggregates. The energy absorption properties were most prominent for aggregate coatings with higher elastic moduli, such as nylon and urea formaldehyde, and this corresponds with the wide band gap behavior observed with stiffer coatings in the analysis of slab wave transmission. The presence of resonant aggregates leads to the attenuation of wave energy and therefore a reduction in the tensile and compressive stresses observed in the brittle mortar phase, which is most susceptible to weakening and fracture under high stresses. This analysis provides additional understanding and design indications for applications where blast wave loading is considered.

Chapter 5

Brittle fracture in a metaconcrete slab

In Chapter 4 the analysis of purely elastic metaconcrete slabs under the action of a blast wave loading revealed that tuned aggregates are capable of trapping a significant portion of the supplied energy, thus reducing the energy and stress transferred to the mortar matrix. However, these analyses did not account for the brittle behavior of the mortar phase, which can fracture under dynamic loading, and thus models that contain only elastic constituents cannot accurately describe the full dynamic behavior of metaconcrete.

In this chapter, we analyze the response of metaconcrete slabs under blast loading, additionally incorporating into the analyses the brittleness of the mortar phase of the slab. We account for fracture through an eigenerosion scheme that applies to the finite element discretization of the solid (Pandolfi and Ortiz, 2012). Erosion of solid elements within the mortar phase occurs when elements meet an energy–based criterion for failure, meaning that they can no longer carry the applied stress and are therefore labeled as eroded. The insight gained from the incorporation of fracture within the dynamic analysis of a slab will enable us to better understand metaconcrete behavior in applications such as blast shielding and impact protection.

To assess the performance of metaconcrete in the presence of brittle fracture, we utilize the slab model outlined in Chapter 2. We model a periodic array of metaconcrete aggregates within a mortar matrix, and perform an inelastic analysis where fracture of the slab constituents, and most importantly the mortar phase, is accounted for through an eigenerosion scheme. Elastic analyses conducted previously displayed distinct trends in energy distribution and stress magnitude, clearly showing that both the material properties and thickness of the aggregate coating change the way in which metaconcrete behaves under the action of a blast wave. Therefore, to fully characterize the behavior of a metaconcrete slab, we investigate a number of aggregate material and geometry configurations. The investigation of different aggregate configurations allows us to evaluate the effect of the presence of selective natural frequencies on the attenuation of the shock waves induced by an assigned blast loading, and to additionally understand the behavior of aggregates with various resonant frequencies in the post-blast behavior of a fractured metaconcrete slab.

5.1   Modeling mortar fracture through an eigenerosion scheme

The shock and damage mitigation properties of metaconcrete are derived from the dynamical behavior of the inclusions. These properties are observed when an impulsive loading is applied to the system. Under such a loading, it is unlikely that metaconcrete behaves in an elastic manner, and therefore it is possible to observe damage and fracture due to the natural brittleness of the mortar matrix. So far, we have only considered purely elastic metaconcrete constituents; however, in this study, we wish to account for inelasticity within the mortar material, i.e., the inability of mortar to support stresses that exceed its resistance. We perform inelastic analyses, accounting for fracture by utilizing an erosion algorithm derived from a general eigenfracture approach that has been proved convergent (Schmidt et al., 2009).

Eigenfracture is an approximation scheme for variational models of Griffith's theory of fracture that resorts to the classical device of eigendeformations (Colonnetti, 1917) in order to account for material fracture. To this end, the energy functional of the system is assumed to be dependent on two fields: the displacement field u and an eigendeformation field ε^* which describes the crack set and the opening displacements of the crack. Specifically, eigendeformations allow the displacement field to develop jumps at no cost in local elastic energy. In the eigenfracture scheme the definition of the support of the eigendeformation field requires the introduction of a small parameter ϵ, with the dimension of length, which has the only requirement that it must tend to zero with, but more slowly than, the discretization size h. Thus, the support of the eigendeformation field is called the ϵ-neighborhood. Upon this definition, the fracture energy is set to be proportional to the volume of the ϵ-neighborhood, suitably scaled by $1/\epsilon$. The optimal crack set is obtained by minimizing the energy functional with respect to both the displacement and the eigendeformation fields, subject to irreversibility constraints.

We note that other two-field approximation schemes for brittle fracture, most notably the Ambrosio-Tortorelli scheme (Ambrosio and Tortorelli, 1992; Braides and Dal Maso, 1997; Francfort and Marigo, 1998), have been proposed in the past and used as a basis for numerical approximations (Bourdin et al., 2000) and they have been shown to be convergent (Negri, 2006).

When combined with a finite element discretization, eigenfracture may be implemented as a particular form of element erosion named *eigenerosion*, i. e., an element can be either intact, in which case its behavior is elastic, or be completely failed, or *eroded*, and have no load bearing capacity. The concept of element erosion has been extensively utilized to simulate fracture in a number of areas of application, including terminal ballistics (Johnson and Stryk, 1987; Belytschko and Lin, 1987; Ortiz and Giannakopoulos, 1990; Børvik et al., 2010). However, some of these methods fail to converge or converge to the wrong limit (Negri, 2003). By contrast, the eigenerosion approach inherits the characteristics of the eigenfracture scheme which is known to properly converge to Griffith fracture (Griffith, 1921) in the limit of vanishingly small mesh sizes (Schmidt et al., 2009). In particular, the local-neighborhood averaging of the energy which underlies the calculation of the effective energy-release has the effect of eliminating spuri-

ous mesh-dependencies.

The implementation of eigenerosion, including the all-important ϵ-neighborhood construction, is exceedingly simple (Pandolfi and Ortiz, 2012) and applies to general situations, possibly involving complex three-dimensional fracture patterns such as branching and fragmentation, and most notably, to any kind of approximation scheme (Pandolfi et al., 2013; Li et al., 2015). The convergence properties of the eigenerosion scheme for modeling fracture propagation in three dimensional problems have been discussed in Pandolfi and Ortiz (2012). The accuracy and convergence of the eigenerosion approach is comparable, at a much reduced implementation cost and complexity, to that of other numerical fracture approaches.

(a)

(b)
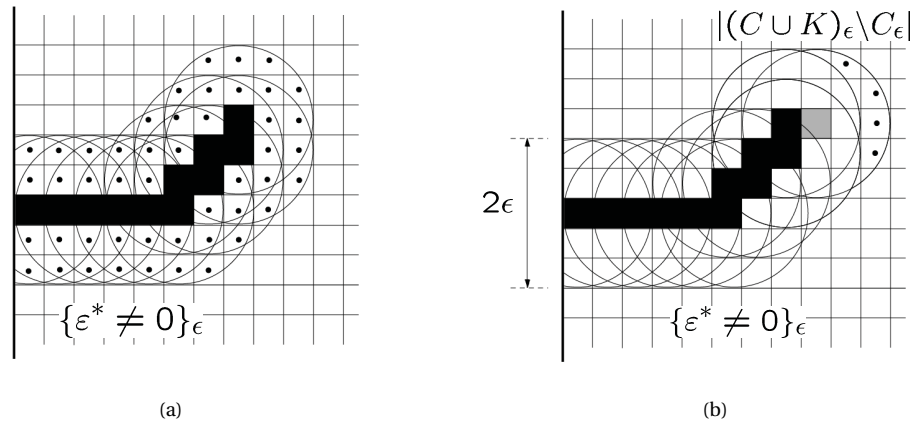
Figure 5.1: (a) Visualization of the crack ϵ-neighborhood, $C_\epsilon = \{\varepsilon^* \neq 0\}_\epsilon$, where ε^* represents the eigendeformation. The ϵ-neighborhood is the set of elements whose barycenters are at distance less or equal to ϵ from any of the barycenters of the eroded elements in the crack set, C, filled in black. Elements in the crack ϵ-neighborhood are marked with black dots. (b) Visualization of the elements belonging to the incremental crack ϵ-neighborhood to be considered for the erosion of the test element, K, marked in gray (Pandolfi and Ortiz, 2012).

The ease of implementation of eigenerosion in a finite element code motivates the choice of this approach for modeling fracture in metaconcrete. The method requires the construction of the ϵ-neighborhood for each element, and necessitates an auxiliary topology array together with a search algorithm to fill its entries. The practical meaning of the element ϵ-neighborhood is to define the portion of discretized solid whose elastic energy will be dissipated as the consequence of the element failure. The collection of the ϵ-neighborhood of eroded elements defines, in turn, the ϵ-neighborhood of the crack set. This is visualized in Figure 5.1(a), where the crack set elements are filled in black and the crack ϵ-neighborhood is shown surrounding the eroded elements.

The failure criterion consists of a comparison of energies for each non-eroded element. The amount of elastic energy of the element ϵ-neighborhood is compared with the attendant fracture energy, so that

the determination of the next set of elements to be eroded is based on the net energy gain,

$$-\Delta F_K = -\Delta E_K - G_c \Delta A_K, \tag{5.1}$$

where $-\Delta E_K$ is the elastic energy released upon erosion of element K, and $G_c \Delta A_K$ denotes the fracture energy cost. The energy release rate attendant to the erosion of one element can be computed explicitly as the difference between the energies of the body before and after the erosion of the element, or more conveniently, it can be approximated using first–order asymptotic formulae for notches (Pandolfi and Ortiz, 2012). For the particular case of metaconcrete subject to a blast wave loading, we modify the eigenerosion algorithm to also account for failure in compression, which was not considered in the original algorithm. In this case, we therefore account for only the deviatoric part of the elastic energy,

$$\Delta E_K^{\text{dev}} = \Delta E_K - \Delta E_K^{\text{vol}}. \tag{5.2}$$

The fracture energy cost is computed using the critical energy release rate G_c of the material multiplied by a measure of the crack extension. The crack extension is given by the elemental area ΔA_K, which is the increment of the crack area attendant to the erosion of a previously intact element $K \notin C$. This is set to be proportional to the advancing volume of the crack ϵ-neighborhood, shown in Figure 5.1(b), suitably scaled by $1/\epsilon$, i.e.,

$$\Delta A_K = \frac{|(C \cup K)_\epsilon \setminus C_\epsilon|}{2\epsilon}. \tag{5.3}$$

If the elemental elastic energy is larger than the elemental fracture energy, the element is eroded. The larger the value of the G_c parameter, the higher the elastic energy needed to enable the advance of the crack. Note that in the implementation of the eigenerosion scheme with metaconcrete, when an element is eroded the element material is replaced with a corresponding material with no shear bearing capabilities. This material behaves as a fluid in compression, and therefore is still able to transmit stresses.

In addition to the standard material parameters needed for elastic analyses, an implementation of eigerosion also requires the critical energy release rate for any material that is allowed to fracture, along with the specification of the extension of the ϵ-neighborhood, i.e., the regularization parameter ϵ. The size of the regularization parameter must be chosen so that it tends to zero more slowly than the mesh size. For the purposes of convergence, it is suffice to express ϵ as simply a multiple of the minimum mesh size h_{min}, i.e.,

$$\epsilon = C_1 h_{\text{min}}, \tag{5.4}$$

where C_1 is a constant. In the following analyses, we utilize a ϵ-neighborhood size of either $\epsilon = 6h_{\text{min}}$ or $\epsilon = 4h_{\text{min}}$, and consider three values of critical energy release rate for the mortar matrix material; $G_c = 60$, 70, and 80 N/m. This range of energy release rates covers the typical estimated values of fracture energy for mortar.

5.2 Finite element dynamic analysis including erosion

To study the behavior of metaconcrete undergoing fracture and erosion, we implement the same finite element model as used in the elastic analyses of Chapter 4. We utilize the coarse finite element discretization outlined in Chapter 2, details of which are repeated here in Table 5.1. For each configuration, Table 5.1 lists the minimum mesh size $h_{\min}$, and the average mesh size h_{avg}, within the mortar phase of the slab. The minimum mesh size is used in the eigenerosion implementation for calculation of the ϵ-neighborhood size, and in our models we implement $\epsilon = 6h_{\min}$ for configurations A and B, and $\epsilon = 4h_{\min}$ for configuration C.

Table 5.1: Discretization data for fracture calculations.

Configuration	$R_l\, t$ (mm^2)	Nodes	Elements	$h_{\min}$ (mm)	h_{avg} (mm)
A	11	19228	96314	0.0026	0.503
B	20	18299	91519	0.0271	0.502
C	27	20891	107562	0.1271	0.486

The elastic material behavior of each slab constituent is described by a neo-Hookean material model, extended to the compressible range. Fracture occurring under the eigenerosion scheme is allowed only in the mortar phase of the metaconcrete slab when lower yield explosions are considered. Given the higher resistance and ductility of the aggregate constituents, in the case of smaller explosions we therefore assume elastic behavior for both the core and coating of the aggregates. A further investigation for larger explosion pressures also includes erosion of the aggregate materials. To facilitate a quantitative comparison, we analyze an equivalent mortar slab by using the same meshes as utilized for the metaconcrete slab, assigning in this case the properties of the mortar material to all elements.

We apply periodic boundary conditions to the lateral faces of the slab. The forward face is subjected to a blast loading caused by the ignition of an explosion in air, while the opposite end face is unconstrained and thus free to move. The blast pressure history results in a large spectrum of applied frequencies, through which we activate the resonant aggregate behavior. We assume a blast force caused by the ignition of an explosive charge located 0.015 m from the central point of the exposed slab surface. As discussed in Chapter 2, the controlling parameter for explosions in atmosphere is the yield factor λ, i. e., the cubic root of the ratio between the energy released by the actual explosion and the energy released by a 1 ton TNT reference explosion. The model for the blast pressure history used in the calculations is summarized in Appendix B. For the study of fracture behavior, we investigate yield factors within the range of $\lambda = 0.01 - 0.5$, looking at both low and high yield explosions to see the effect on the amount of erosion and energy distribution within the slab.

We study the behavior of metaconcrete slabs under erosion by first considering the features and appearance of the propagating stress wave in both a metaconcrete slab and an equivalent homogeneous

mortar slab. These analyses provide a baseline and motivation for subsequent parametric studies, where we evaluate numerically the effect of different model parameters, aggregate geometries, and material properties on the fracture behavior of metaconcrete slabs.

5.2.1 Stress wave propagation in metaconcrete slabs under fracture

To see the effect of the presence of metaconcrete aggregates in a slab where the mortar is allowed to fracture, we begin by visualizing the stress distribution a small time after the arrival of the blast wave. The difference in stress wave propagation between a purely mortar slab and a metaconcrete slab allows us to assess any changes in behavior between the two cases.

(a) Homogeneous material

(b) 1 mm silicone coated lead aggregates

(c) 1 mm nylon coated lead aggregates
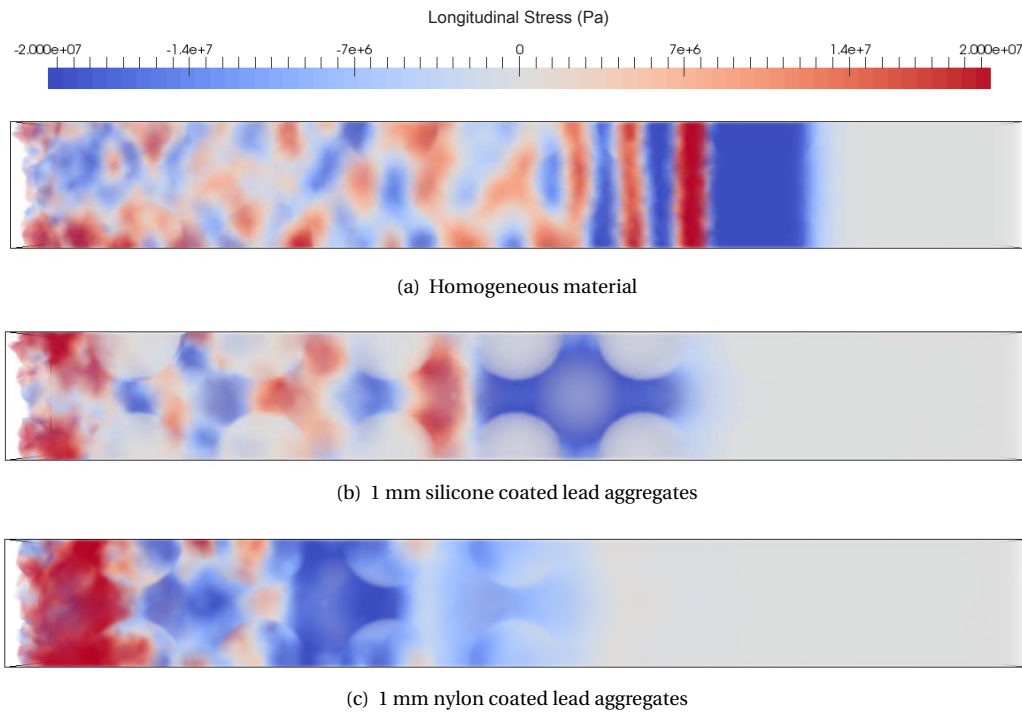
Figure 5.2: Volume rendering of the longitudinal stress distribution at $t = 0.05$ ms in an (a) homogeneous mortar slab (maximum 130 MPa compression, 60 MPa tension), (b) metaconcrete slab with 1 mm silicone coated inclusions (maximum 110 MPa compression, 140 MPa tension), and (c) metaconcrete slab with 1 mm nylon coated inclusions (maximum 130 MPa compression, 120 MPa tension) for $\lambda = 0.05$ and $G_c = 70$ N/m. Blue indicates compressive stress, red indicates tensile stress, and the black outline represents the reference slab configuration. Note that the colorbar is truncated in order to show the details of the stress pattern.

Figure 5.2 shows a volume rendering of the longitudinal Cauchy stress in a purely mortar slab alongside that for two metaconcrete slab configurations, one consisting of an array of 1 mm silicone coated inclusions and another consisting of an array of 1 mm nylon coated inclusions. The blast wave profile was calculated using an explosion yield factor of $\lambda = 0.05$ and a critical energy release rate of $G_c = 70$ N/m

is chosen for the mortar material. The distribution is plotted at $t = 0.05$ ms after the beginning of the simulation, thus capturing the first transition of the shock wave through the slab.

As in the elastic analyses of Chapter 4, we see that the propagation of the stress wave front in the metaconcrete slab is delayed in time when compared to that in the mortar slab. We see also that in the metaconcrete slab the stress is non uniform and distributed around the aggregates, concentrated mostly in the area near the exposed face. By comparison, the stress wave in the mortar slab is planar in configuration with more distinct bands of high compressive and tensile stress.

We note that the values of maximum tensile and compressive stress listed for each slab case are given as the maximum of the entire slab, including the aggregates. In the metaconcrete slab the largest stresses are located in the mortar and aggregates near the exposed face. In this case the metaconcrete aggregates shield the interior of the slab, which is shown by the intense colors observed at the front of the slab in Figure 5.2(b) and Figure 5.2(c). By contrast, in the homogeneous material the highest stresses are located where the shock wave has penetrated into the interior of the slab.

We also note the difference between the two metaconcrete slab configurations. Similar to what was observed in Chapter 4, the aggregates with 1 mm silicone coatings do not seem to capture the stress propagating through the slab, instead the stress is concentrated in the mortar material. By contrast, the stress is captured by the 1 mm nylon coated aggregates, indicating that resonance behavior is activated by the blast loading.

In addition, in both the metaconcrete and purely mortar slabs, material fractures only around the blast site. Missing eroded elements at the left end surface of the slab are evidenced in Figure 5.2, where the black outline indicates the original configuration of the slab. Details of the eroded surface for each slab case are shown in Figure 5.3, where the black outline again describes the original configuration. The images show that the outer layer of elements are missing due to the attainment of the failure criterion, resulting in a blasted surface that appears uneven and rough.

From the eroded surfaces it is clear that a greater amount of degradation is present when the coating elastic modulus is lower. This is seen when comparing the eroded surfaces for the 1 mm silicone coated aggregate case in Figure 5.3(b) to the 1 mm nylon coated aggregate case shown in Figure 5.3(c). The slab containing silicone coated aggregates displays significantly more erosion around the central portion of front slab surface, eroding to expose the entire front face of the first aggregate. The slab containing nylon coated aggregates also shows significant erosion, however the front aggregate in this case is only partially exposed. This effect can be attributed to a number of factors. The use of softer coatings could lead to a greater amount of mortar crushing due to vibration of the aggregate near the exposed face. The energy absorption properties due to the vibration of the aggregates could also lead to reduced erosion by removing energy from the mortar matrix. The elastic analyses of Chapter 4 showed that a blast wave profile can activate aggregates with higher coating elastic moduli and that performance of the slab can be improved when aggregates of this type are used. Thus, we see a similar effect when we consider a slab also

(a) Homogeneous material   (b) 1 mm silicone coated lead aggregates

(c) 1 mm nylon coated lead aggregates
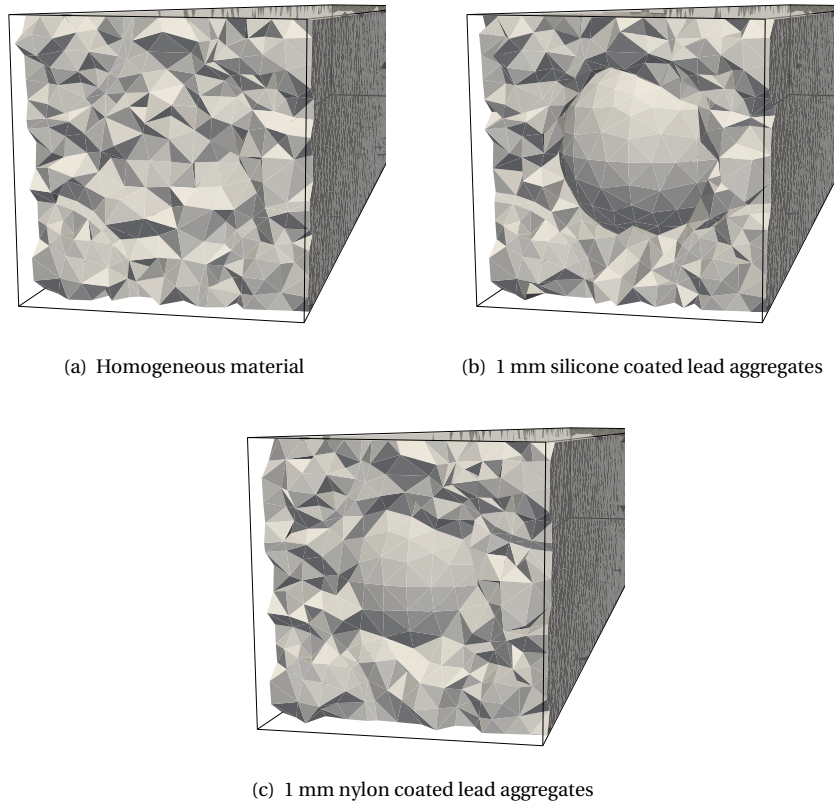
Figure 5.3: Eroded surface of an (a) homogeneous slab, (b) metaconcrete slab with 1 mm silicone coated aggregates, and (c) metaconcrete slab with 1 mm nylon coated aggregates for an explosion yield $\lambda = 0.05$ and a mortar critical energy release rate $G_c = 70$ N/m. The black outline represents the reference slab configuration.

undergoing fracture behavior. Not only is the stress higher in the aggregates when a stiffer coating material is used, as seen in Figure 5.2, the fracturing around the exposed face is also reduced. This indicates that there is some activation of the aggregates and that improved performance may be gained when resonance within the aggregates is utilized. This effect will be explored further in later sections by considering the energy and stress distribution in slabs with various aggregate geometry and material configurations.

Both metaconcrete slabs also show more erosion than the equivalent homogeneous mortar slab, as seen in Figure 5.3(a). The metaconcrete slabs exhibit more erosion around the exposed face due to the presence of the heavy aggregates. Each aggregate has a mass that is between 2.1 and 3.7 times the mass of the equivalent volume of mortar. When the slab undergoes fracture, the heavy aggregates cause additional crushing of the mortar material. This local comminution of the mortar acts as a second energy absorption mechanism, in addition to the absorption that results from resonance within the aggregates. This effect stops the wave from penetrating deep into the slab and causes the the damage to remain localized near

the exposed surface. We explore this effect further in the following section by considering the amount of fracture energy within the slab.

5.2.2 Fracture Energy

Previous studies of purely elastic metaconcrete slabs under blast loading have shown that enhanced performance can be achieved through mechanical energy attenuation and stress reduction. In the presence of fracture, the balance of energy requires us to also account for the fracture energy, which is the dissipation induced by the formation of fracture surfaces. Fracture energy is therefore one of the key parameters to assess the performance of metaconcrete when fracture damage is considered. We recall that within the eigenerosion scheme, based on Griffith's energy criterion, the fracture energy corresponds to the measure of the fracture surface defined by the ε-neighborhood construction multiplied by the critical energy release rate G_c.

The two primary input parameters for the control of the extension and depth of damage in our slab models are the explosion yield factor λ, and the critical energy release rate G_c. We summarize how these parameters affect the amount of energy dissipated during fracture by plotting fracture energy surfaces for two of the slab cases considered above: a homogeneous mortar slab and a metaconcrete slab containing a periodic array of 1 mm nylon coated inclusions. Figure 5.4 displays the results for $\lambda = 0.01 - 0.10$ and $G_c = 60 - 80$ N/m, plotting the energy that has been dissipated through fracturing of the mortar matrix at the end of the calculation.
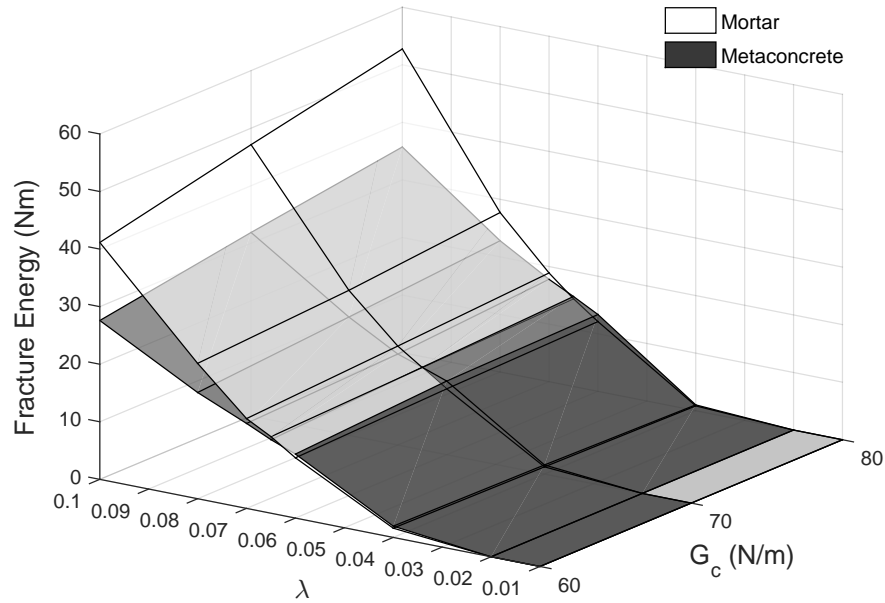
Figure 5.4: Fracture energy plotted against explosion yield factor, λ, and critical energy release rate, G_c, for a homogeneous mortar slab and a metaconcrete slab containing 1 mm nlyon coated inclusions.

The fracture energy computed during the analysis indicates the amount of energy the has been dissipated in forming the fracture surfaces. Each parameter axis, i.e., in the direction of either λ or G_c, indicates different behavior. An increase in fracture energy with higher yield indicates a greater depth of erosion within the slab, i.e., more mortar material is eroded. An increase in fracture energy with energy release rate G_c indicates that more energy is required to fracture the material when erosion occurs. This means that a larger amount of energy is required to produce the same amount of fracture, thus an increase in fracture energy along this axis does not necessarily mean a greater amount of erosion.

Figure 5.4 reveals three distinct patterns of behavior. Below $\lambda = 0.02$ the fracture energy is equal to zero and there is no erosion of the slab, i.e., the slab behaves in a purely elastic manner. Above $\lambda = 0.02$ the slab begins to exhibit fracture, and between $\lambda = 0.02$ and $\lambda = 0.065$ the metaconcrete fracture energy surface lies slightly above that for the equivalent homogeneous mortar slab. This is more evident for yield factors closer to $\lambda = 0.065$. This difference indicates that the metaconcrete slab exhibits slightly more erosion than the homogeneous mortar slab for this range of explosion yields. This correlates with what was seen in Figure 5.3, where erosion in the metaconcrete slab was more extensive than that observed in the equivalent mortar slab. In the explosion yield range between 0.02 and 0.065 it is likely that energy absorption from mortar crushing due to the presence of the heavy metaconcrete aggregates contributes to the difference between the two slabs, resulting in a higher fracture energy due to the erosion of elements around the exposed surface. We also note that a higher input energy may be present in the metaconcrete case, due to larger movement of the exterior slab surface caused by the lower moduli materials used in the aggregates.

Above $\lambda = 0.065$ the behavior transitions and the fracture energy for the homogeneous mortar slab becomes significantly larger than that for the metaconcrete slab. At these higher values of explosion yield the volume of mortar corresponding to the aggregate position in the metaconcrete slab erodes, resulting in a much greater fracture energy. In the metaconcrete slab the aggregates at the front behave like a protective barrier preventing high stresses from reaching the interior of the slab, since the aggregate materials are not eroded during the computation. This causes only the mortar surrounding the aggregate to be eroded and results in a smaller fracture energy than in the metaconcrete slab.

We also see that, for higher yield values, as the critical energy release rate increases there is a linear increase in the fracture energy. This is more pronounced for the mortar slab, which has the highest fracture energy at the maximum values of λ and G_c investigated. This behavior is due to the fact that the depth of the damaged material layer, and thus the equivalent fracture surface, depends mainly on the yield of the explosion; the increment of the fracture energy with G_c for a fixed λ is indeed almost linear.

The effect of the parameters λ and G_c can be further examined by considering the eroded surfaces for different points on the fracture energy surfaces in Figure 5.4. Figure 5.5 shows the amount of fracture near the exposed face for both the mortar and metaconcrete slab considered in Figure 5.4 for three cases: $G_c = 60$ N/m and $\lambda = 0.04$, $G_c = 60$ N/m and $\lambda = 0.10$, and $G_c = 80$ N/m and $\lambda = 0.04$. These combinations

(a) Mortar, $G_c = 60$ N/m, $\lambda = 0.04$

(b) Metaconcrete, $G_c = 60$ N/m, $\lambda = 0.04$

(c) Mortar, $G_c = 60$ N/m, $\lambda = 0.10$

(d) Metaconcrete, $G_c = 60$ N/m, $\lambda = 0.10$

(e) Mortar, $G_c = 80$ N/m, $\lambda = 0.10$

(f) Metaconcrete, $G_c = 80$ N/m, $\lambda = 0.10$
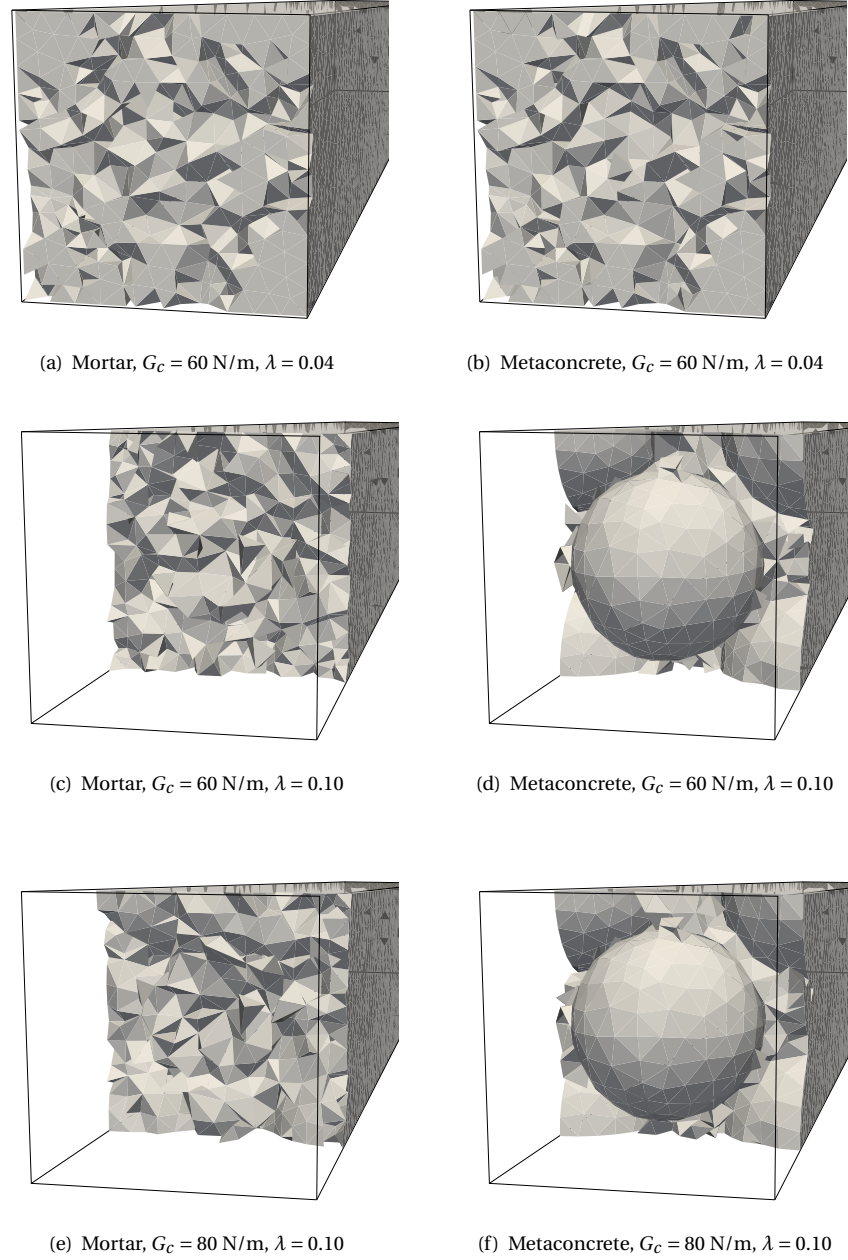
Figure 5.5: Eroded surface of a homogeneous slab and metaconcrete slab containing 1 mm nylon coated inclusions for different combinations of λ and G_c. The black outline represents the reference slab configuration.

of parameters cover the three main patterns of behavior observed in fracture energy contour plot.

Figure 5.5(a) and Figure 5.5(b) show similar results to that observed in Figure 5.3, however displaying less erosion due to the smaller explosion yield factor. We see that the metaconcrete slab shows slightly more fracture than the equivalent homogeneous mortar slab, accounting for the slightly larger fracture

energy for the metaconcrete case. However at this level of explosion yield only the very front surface of the slab is fractured.

Figure 5.5(c) and Figure 5.5(d) show that increasing the explosion yield factor greatly increases the amount of erosion observed around the exposed face. In this case the mortar in the metaconcrete slab is eroded around the aggregates, revealing almost the entire first aggregate surface. The mortar slab erodes to a similar depth, however in this case a greater amount of mortar is eroded, equivalent to the volume of the aggregates.

Figure 5.5(e) and Figure 5.5(f) show the eroded surfaces for the same yield factor, however this time the material constant G_c is increased to 80 N/m. In this case we observe less erosion when the critical energy release rate is increased, since more energy is required to fracture the material.

The shape of the fracture energy plot and the eroded configuration of the slabs considered here imply that there is a difference in behavior due to the presence of resonant aggregates. The difference in fracture energy may be due to a number of factors including mortar crushing at the exposed surface and resonant absorption. Metaconcrete aggregates have been shown to transfer energy away from the mortar in the previous elastic analyses. In the fracture case, the resonant properties of the inclusions may help to trap some of the mechanical energy, diminishing the elastic energy density in the mortar where fracture is occurring, and, as a direct consequence, reducing the stress in the mortar matrix of the slab. This effect will be explored further in the next section.

5.2.3   Parametric analysis of aggregate configurations

The different aggregate geometry and material configurations each produce a unique metaconcrete aggregate resonant frequency. Different combinations of aggregate properties have been shown to change slab behavior in the study of both transmission characteristics and the blast wave loading of slabs with elastic constituents. To compare the performance of each aggregate configuration when fracture processes are present, we conduct a parametric study of the energy and stress distribution within the slab, considering the configurations presented in Section 2.1.1 of Chapter 2. For all calculations we use a blast wave generated by an explosion yield factor of $\lambda = 0.05$ and a mortar critical energy release rate of $G_c = 70$ N/m.

5.2.3.1   Aggregate energy

Figure 5.6 presents the amount of mechanical energy trapped in the slab aggregates as a fraction of the total mechanical energy in the slab, where the energies are averaged over the duration of the calculation. The trapped energy is plotted for each coating stiffness and aggregate geometry. The aggregate energy indicates the amount of energy absorbed by the metaconcrete aggregates and, in a similar way to the energy calculations of Chapter 4, reveals how the amount of energy trapped inside the aggregates changes

as the coating configuration is varied.
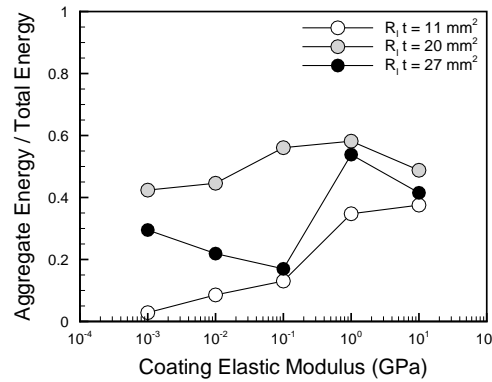
Figure 5.6: Fraction of the total mechanical energy captured by the aggregates for various coating moduli and geometries.

For all three aggregate geometry configurations we observe a similar trend, where the energy absorbed by aggregates with higher coating elastic moduli is greater than that for aggregates with softer coatings. This is the same effect as was seen in the elastic analyses of Chapter 4 and also correlates with the stress patterns observed in the longitudinal stress distributions shown in Figure 5.2. Other factors may also come into play when fracture is included. When the mortar matrix material erodes the aggregate surface can be exposed and in this case the aggregates may be subject to more direct and higher stresses. This may account for the difference between the three coating geometries, since each configuration will have a different amount of erosion.

5.2.3.2 Maximum longitudinal stress

To further characterize how metaconcrete aggregates help to reduce the effect of the propagating shock wave, we consider the maximum longitudinal Cauchy stress in the mortar matrix of the slab. We take into account only the stress present in the second-half of the slab, farthest away from the blast site. This allows us to look at only the intact portion of the slab, avoiding the high stresses associated with the elements undergoing fracture. Figure 5.7 presents the maximum longitudinal Cauchy stress for a variety of metaconcrete slabs, expressed as a percentage of the maximum stress in an equivalent homogeneous mortar slab. Both longitudinal tensile and compressive stresses are shown.

Both the tensile stresses in Figure 5.7(a) and compressive stresses in Figure 5.7(b) reveal the same trend, with a decrease in value as the modulus of the compliant coating is increased. Slabs containing aggregates with the softest coating material, i.e. the silicone coated aggregates, display stresses that range from 59% to 95% of that found in the homogeneous mortar slab, which is the highest maximum stress observed for all of aggregate coating materials. We also see that coatings with the two highest elastic
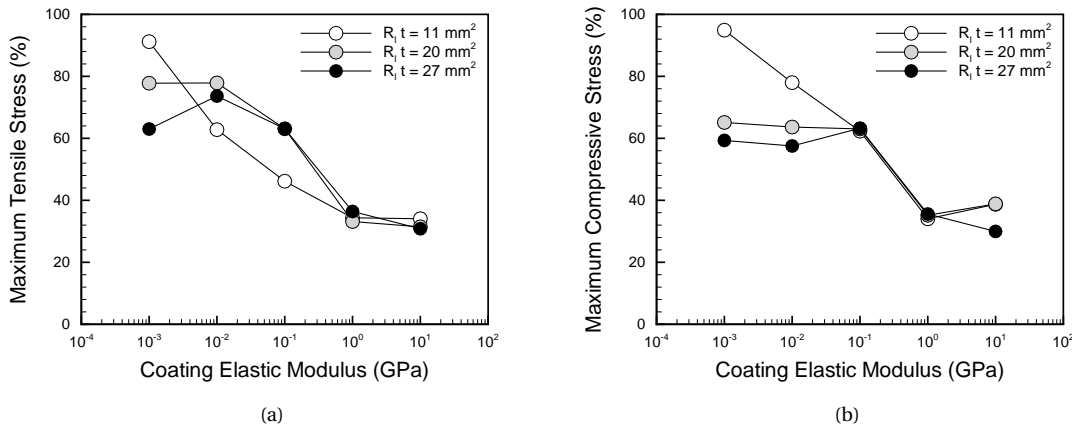
Figure 5.7: Maximum longitudinal Cauchy stress in the second-half of the metaconcrete slab expressed as a percentage of maximum longitudinal Cauchy stress in an equivalent homogeneous mortar slab; (a) maximum tensile stress, (b) maximum compressive stress.

moduli display the most significant improvement over the equivalent mortar slab. For the nylon and urea formaldehyde coated aggregates, the tensile stress ranges between 31-36% of the mortar value and the compressive stress attains 30-39% of the maximum homogeneous mortar slab stress. This improvement indicates that performance enhancements can be achieved by incorporating resonant aggregates, significantly reducing the stress load on the mortar matrix by capturing energy within the aggregates.

The geometry of the aggregates also causes different behavior, particularly for the lower coating elastic moduli. The aggregates with a 3 mm coating thickness seem display slightly smaller stress values when coating moduli is very low, such as for the silicone coated aggregates. However, changing the geometry has a less significant effect when the aggregates within the slab are fully activated by the blast loading, shown by the smaller difference between aggregate geometry cases for coatings with higher stiffness. In fact, the percentage of maximum mortar stress attained by each geometry configuration is very similar for all three coating thicknesses when nylon or urea formaldehyde coating materials are used.

The maximum longitudinal stress for every aggregate configuration also shows improvement over the equivalent mortar slab, where each combination considered produces a mortar matrix stress that is lower than that obtained for the homogeneous slab. This indicates that including the aggregates causes significantly less stress to propagate into the end section of the slab. The aggregates can act like a shield to the interior while also absorbing stress away from the mortar matrix.

5.2.4   High yield explosions

To further characterize the fracture behavior of metaconcrete, we now consider loading cases that are more extreme in magnitude by analyzing the behavior of metaconcrete under the action of very high

yield explosions. In this case we now assume that fracture of the aggregate core and coating materials may occur during the blast event. Lead is a ductile material thus has a much higher critical energy release rate than concrete, but still may fracture when exposed directly to the explosion pressure as the mortar matrix erodes. We therefore assume a critical energy release rate of $G_c = 10,000$ N/m for the lead core material. We again consider only the metaconcrete slab case where 1 mm nylon coated aggregates are used and we assume a value of $G_c = 1,000$ N/m for the coating material. A $G_c = 80$ N/m is chosen for the mortar matrix. We consider a range of very high explosion yield factors, taking values between $\lambda = 0.1$, the highest assumed in the analyses above, and $\lambda = 0.5$. This will indicate how the slab may behave under a catastrophic event, where a large amount of the slab is fractured and eroded.

(a) Homogeneous material   (b) Metaconcrete
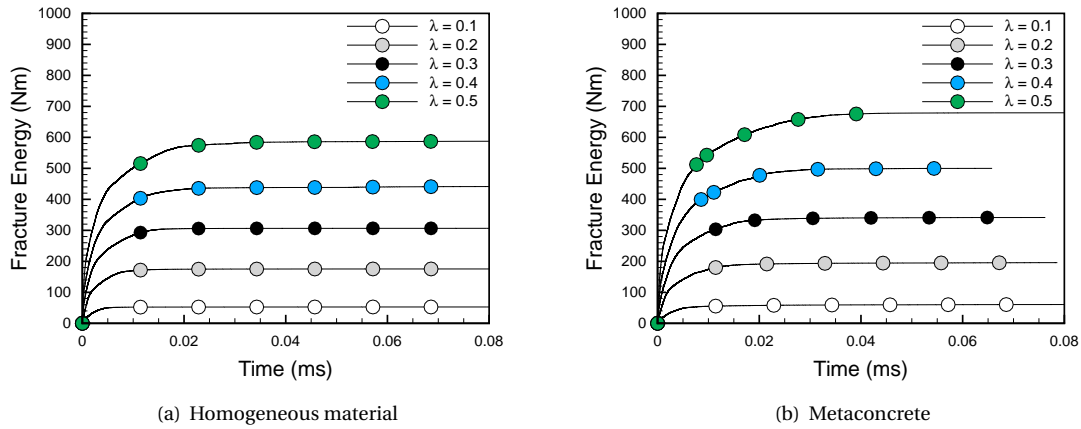
Figure 5.8: Fracture energy as a function of time plotted for (a) a homogeneous mortar slab, and (b) a metaconcrete slab with eroding 1 mm nlyon coated inclusions for a range of high yield factor explosions. The critical energy release rate is $G_c = 80$ N/m for the mortar matrix, $G_c = 1,000$ N/m for the coating, and $G_c = 10,000$ N/m for the lead core material.

To investigate this case we begin by plotting the fracture energy as a function of time for each of the explosion yield factors considered. Figure 5.8 shows the results for both the metaconcrete slab and an equivalent homogeneous mortar slab. As the explosion yield factor is increased, the fracture energy in the slab becomes larger. This indicates that a significant amount of energy is required in order to fracture the slab, an effect that can now be attributed to the fracture of both the mortar matrix and the aggregate materials themselves. The fracture energy for the metaconcrete slab is also larger than that obtained for the mortar slab at the same yield, particularly for the higher yield explosions such as that given by $\lambda = 0.5$. This again shows that more energy is dissipated through fracturing of the metaconcrete slab, indicating that metaconcrete effectively behaves as a tougher material.

Figures 5.9-5.10 visualize the behavior of a metaconcrete slab alongside a homogeneous mortar slab at 0.06 ms after the start of the calculations for each of the explosion yield factors presented in Figure 5.8. For each case there is a significantly greater depth of erosion in the mortar slab when compared with the

(a) $\lambda = 0.1$

(b) $\lambda = 0.2$

(c) $\lambda = 0.3$

(d) $\lambda = 0.4$

(e) $\lambda = 0.5$
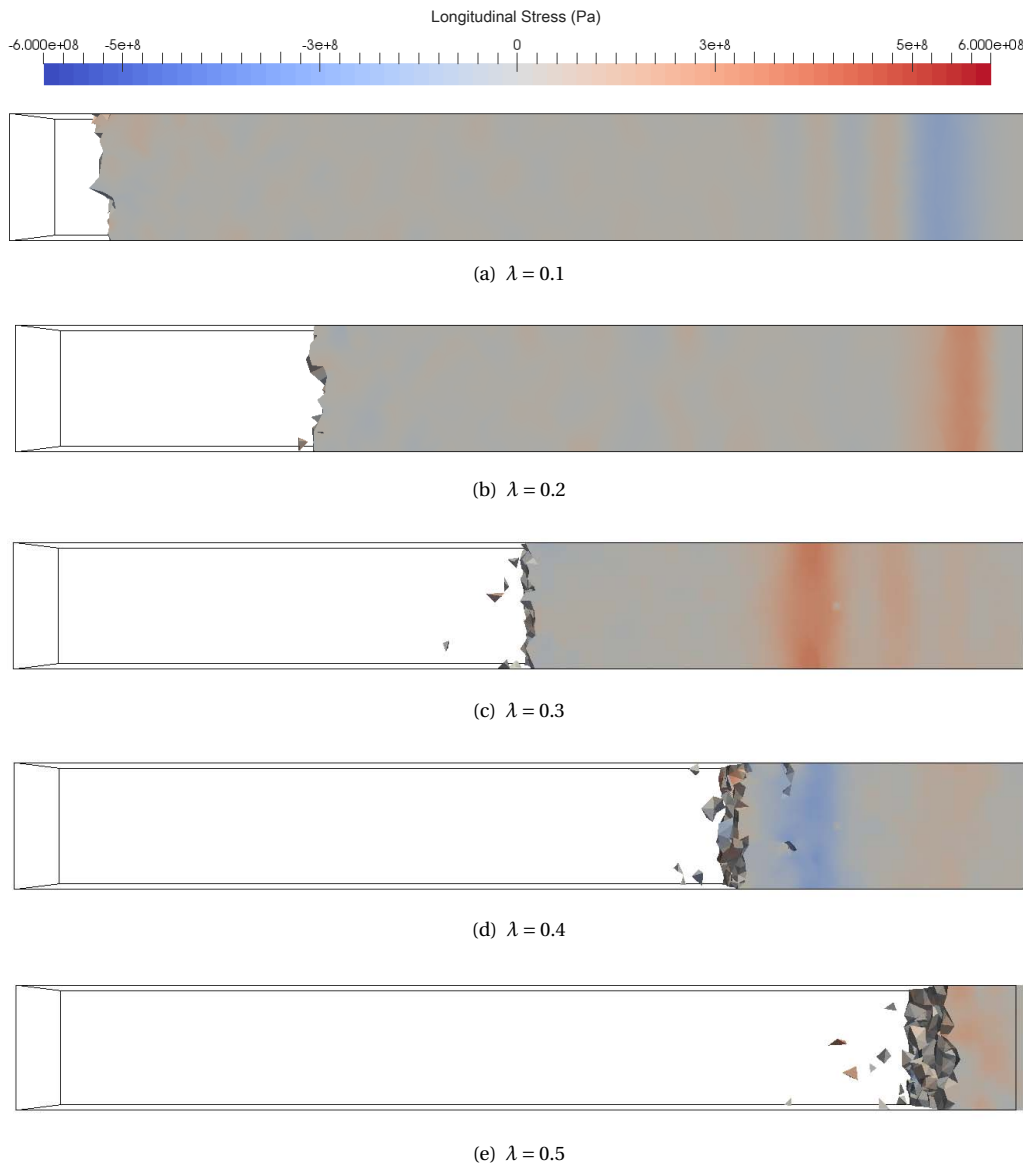
Figure 5.9: Longitudinal stress distribution at $t = 0.06$ ms in a homogeneous mortar slab for a range of high yield explosions with yield factors between $\lambda = 0.1$ and $\lambda = 0.5$. The critical energy release rate for the mortar matrix is given by $G_c = 80$ N/m. Blue indicates compressive stress, red indicates tensile stress, and the colorbar ranges in scale between 600 MPa compression to 600 MPa tension. The black outline represents the reference slab configuration.

metaconcrete slab, particularly for the cases where a higher explosion yield factor is used. In the homogeneous material the stress wave has also propagated into the end of the slab, whereas in the metaconcrete slab no stress wave is observed. In fact, in Figure 5.9(b) and Figure 5.9(c) the stress wave is on its return transition through the slab, indicated by the reflected tensile wave, and in Figure 5.9(d) and Figure 5.9(e) the slab has eroded so significantly that there have been multiple reflections of the shock wave inside the slab. In the metaconcrete slab, by contrast, the stress is concentrated in the still intact aggregates near the

front of the slab. This effect indicates that the aggregates near the exposed surface act like protective barrier in high yield explosions, shielding the interior from the stress wave and concentrating erosion around the surface exposed to the blast wave.
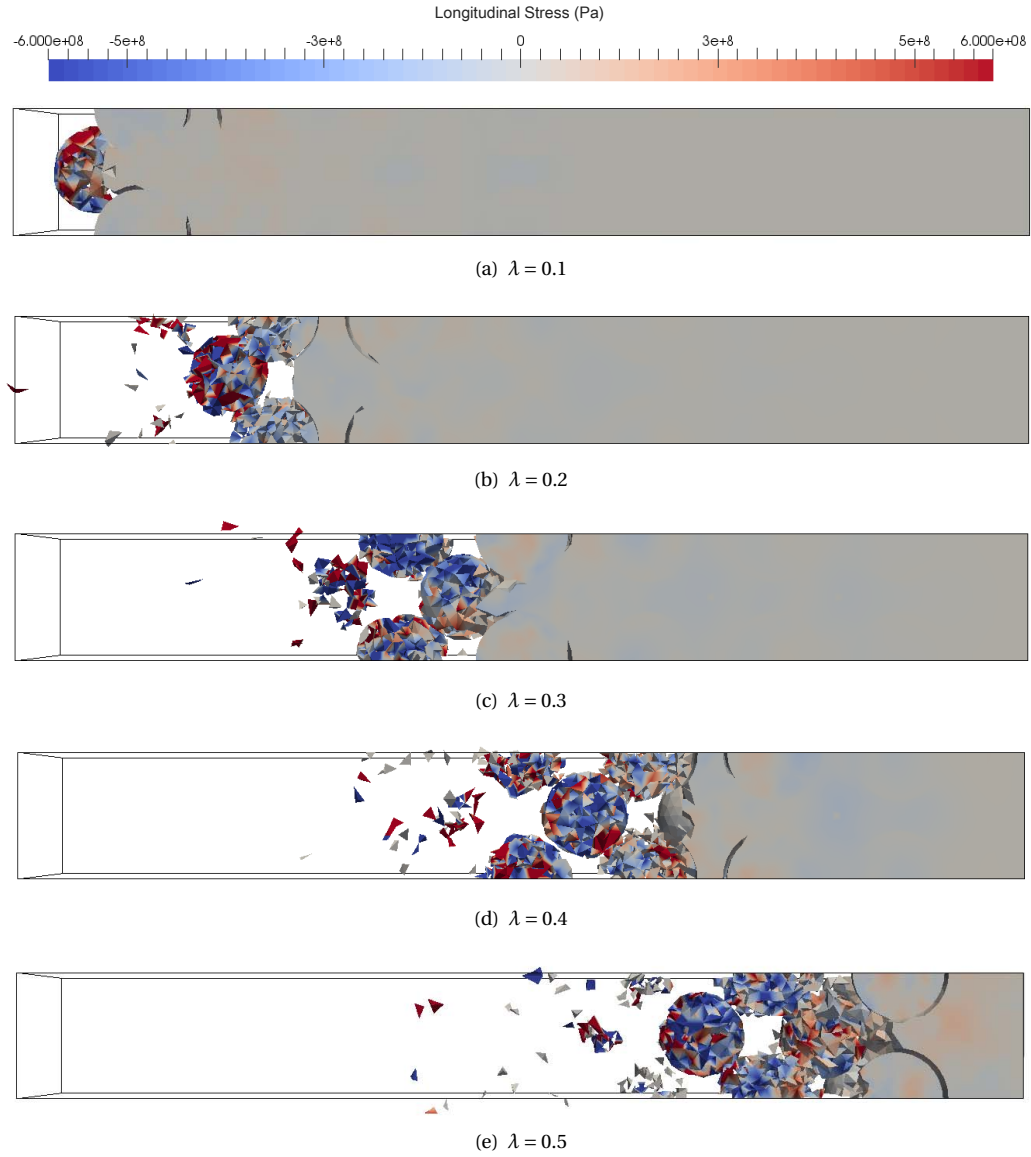
Figure 5.10: Longitudinal stress distribution at $t = 0.06$ ms in a metaconcrete slab with 1 mm nylon coated inclusions for a range of high yield explosions with yield factors between $\lambda = 0.1$ and $\lambda = 0.5$. The critical energy release rate is given by $G_c = 80$ N/m for the mortar matrix, $G_c = 1,000$ N/m for the aggregate coating, and $G_c = 10,000$ N/m for the aggregate lead core material. Using the same color scale as in Figure 5.9, blue indicates compressive stress and red indicates tensile stress. The black outline represents the reference slab configuration.

5.3   Summary

We present an investigation into the behavior of metaconcrete slabs undergoing fracture when subjected to a blast wave loading. Studies previously conducted on slabs with purely elastic constituents indicate that there is a reduction in mortar stress and a general improvement in slab performance when metaconcrete aggregates with relatively stiff coatings are present in the slab. To more accurately model the brittle behavior of mortar under dynamic loading, we extend the elastic models examined previously to include the fracture properties of the mortar matrix. Fracture is modeled through an eigenerosion scheme, which is based on the more general eigenfracture approach. The attainment of fracture within the slab is evaluated through an energy–based criterion, and elements satisfying the failure criterion are eroded, and therefore excluded from the finite element mesh so that they no longer have load bearing capacity. This results in an eroded volume that propagates from the surface of the slab exposed to the blast wave.

We test the models with a blast loading caused by the ignition of an explosive charge of yield factor λ. We see that this parameter, along with the critical energy release rate of the mortar material, G_c, impact the amount of energy released during fracture, implying a change in the depth and size of the fracture surface. Plotting the longitudinal stress distribution of both a homogeneous mortar and metaconcrete slab for the same λ and G_c, we see that the shock wave induced by the blast loading is delayed by the presence of the metaconcrete aggregates. The stress distribution observed when fracture processes are present is similar to that seen in the case of purely elastic metaconcrete constituents, where trapping of the stress wave occurs within the aggregates at the front of the slab near the exposed face. This correlates with the slab energy distribution, which is investigated for a number of aggregate material and geometry configurations. The amount of energy that is trapped by the metaconcrete aggregates increases when attenuation behavior of the aggregates is activated by the blast loading. Similarly, the magnitude of the maximum stress in the slab mortar matrix was found to be significantly improved when metaconcrete aggregates were incorporated into the slab structure.

These results, combined with those found for the transmission and elastic behavior of metaconcrete, imply that tuning the aggregates to the frequency input of an applied dynamic loading will aid in mitigating the high stresses caused by a propagating shock wave.

Chapter 6

Concluding remarks and further directions

This thesis introduced and developed a new concept for a modified concrete which is designed for dynamic loading applications. Recently, the field of metamaterials science has grown extensively, with new materials being developed for a wide range of applications in electromagnetics, acoustics, and elastodynamics. Metamaterials consist of a designed internal structure, that is engineered to produce unusual properties when interacting with an applied wave or loading. Influenced by the use of locally resonant inclusions in acoustic metamaterials, we propose a new type of concrete that contains resonant aggregates which provide enhanced performance in the presence of dynamic loading. We have named this new composite *metaconcrete*.

Metaconcrete is a new type of engineered metamaterial where the standard stone and gravel aggregates of regular concrete are replaced by designed inclusions that resonate at chosen frequencies. The aggregates have a bi-material layered structure, consisting of a heavy metal core coated with a compliant outer material. The aggregates are designed so that resonance may be activated by an applied loading at designed frequencies, allowing for a transfer of energy between the aggregates and the mortar matrix. The activation of resonance leads to what as known as 'negative effective mass', which has been demonstrated by theoretical studies of one–dimensional bars and spring–mass systems.

In the present study we have undertaken a numerical analysis to determine the response of a metaconcrete slab made of uniform and regularly arranged aggregates. The inclusions are spherical and their arrangement was chosen in order to produce a packed configuration with very little separation between the aggregates. We consider a number of different aggregate geometry and coating material configurations, and derive tuning equations which can be used to determine a recommended activation frequency for each aggregate combination.

We begin the numerical analyses by considering a one–dimensional idealization of a metaconcrete slab, investigating the band gap behavior and transmission characteristics for four different aggregate material and geometry configurations. The results reveal that band gaps of different sizes and frequency location can be generated when locally resonant behavior is present in the system. These band gaps correspond with the resonant frequency of the particular aggregate configuration and also the frequency

band across which a reduction is observed in wave amplitude transmission.

To further investigate the frequency-dependent nature of metaconcrete, we consider the transmission of energy through a three–dimensional finite element slab model. Transmission coefficients for the system are computed based on the amount of energy that reaches the far end of the slab, where the average energy absorbed by the last aggregate was compared to that of all the aggregates. The results reveal a dip in the transmission coefficient near the rigid body translation resonant frequency of the inclusion, which corresponds with the behavior observed from the one–dimensional model. Within the dip frequency range, the magnitude of energy transmission is greatly reduced when compared to that observed in a homogeneous mortar slab. This improvement in performance over a slab with no resonant aggregates suggests frequency ranges that provide the most beneficial behavior for each aggregate configuration. The study of energy transmission also suggests that a nylon coating is the best choice for an overall improvement in the behavior of metaconcrete with elastic constituents.

The three–dimensional metaconcrete slab model is then tested with a blast loading profile generated by a explosion of known size and duration. The numerical results show that, under dynamic excitation, the slab containing an array of metaconcrete aggregates behaves in a rather different way to an equivalent homogeneous slab with the effective properties of concrete. The most prominent effect is the reduction in the amount of energy transmitted across the system and, as a result, the reduction of stress within the brittle phase, i. e., the mortar. The results show that performance of the slab is heavily influenced by the elastic modulus of the compliant coating. Changing the coating modulus alters the resonant frequency of the aggregate. Coatings with higher stiffness, and a thus a higher resonant frequency, were found to provide the most significant absorption of mechanical energy and the greatest reduction in mortar stress. The results indicate that aggregates with coatings corresponding to the two highest elastic moduli, i.e., nylon and urea formaldehyde, provide the most beneficial attenuation of the applied blast loading.

Mortar is a brittle material that will suffer from weakening and fracture under the action of a blast wave loading. To more accurately model the brittle behavior of mortar we therefore extend the elastic models examined previously to include the fracture properties of the mortar matrix. Fracture is modeled through an eigenerosion scheme, which is based on the more general eigenfracture approach. The attainment of fracture within the slab is evaluated through an energy–based criterion, and elements satisfying the failure criterion are eroded, and therefore excluded from the finite element mesh so that they no longer have load bearing capacity. This results in an eroded volume that propagates from the surface of the slab exposed to the blast wave. We find that the incorporation of metaconcrete aggregates into a slab design modifies the behavior of a mortar slab, reducing the effect of a blast loading when the slab is also undergoing erosion and fracture. When the aggregates within a metaconcrete slab are activated, there is a reduction in the amount of energy and stress that reaches the far end of the slab. Similar to the previous elastic analyses, the use of aggregates with higher coating elastic moduli led to the greatest performance enhancement for the particular blast profile chosen, with these aggregates demonstrating the highest absorbed energy

and lowest mortar stress values. Therefore, tuning the aggregates to the frequency input of an applied dynamic loading will aid in mitigating the high stresses caused by a propagating shock wave.

Metaconcrete could be a useful alternative to traditional concrete materials for a multitude of applications where protection from blast and impact is required. Some possible structural applications include wall panels, exterior walls, and barriers for explosive blast shielding structures, along with impact protection slabs and shields. Further examples are presented Appendix C, along with a discussion of some of the more practical design considerations for metaconcrete. Another potential application is the use of metaconcrete with lower frequency seismic waves, which could include seismic shielding slabs or tuned damping foundations. The same principles could be applied to armored vehicles, where the mortar material could simply be replaced with an alternative matrix material suitable for the particular purpose

There are many potential areas for further investigation of metaconcrete and its behavior. The models considered so far only utilize periodic arrays of metaconcrete aggregates. If the aggregates were to be mixed into mortar in the same way as the stone and gravel aggregates of regular concrete, then an exactly periodic array of aggregates would not easily be achieved. The practical implementation of metaconcrete for structural purposes will therefore require further investigation of metaconcrete slabs with non–periodic aggregate arrangements. The numerical comparison of different slab aggregate configurations would also be of interest. Calculations showing the full set of slab behavior for not only a homogeneous mortar slab but also a gravel aggregate slab and a slab containing purely lead aggregates could provide very interesting design indications. Further, different layered aggregate sizes and materials may need to be considered for loading conditions other than the blast wave profile primarily investigated here. The use of alternative aggregate geometries, materials, and arrangements therefore offers an area open for potential investigation.

To further characterize the real–life behavior of metaconcrete, other material characteristics could be incorporated into the model. The models used thus far also do not consider any viscous effects and the high loss tangent of the lead core material could also be considered in future studies. Similarly, a thorough experimental investigation of metaconcrete properties and dynamic behavior would provide a wealth of information useful for the practical implementation of metaconcrete. Experimental validation of the numerical results would provide further insight into the resonant behavior of the aggregates and the effect this has on the performance of the overall material. An experiment could be designed to test the resonant properties of a single aggregate, comparing the resonant frequency to that found in an equivalent numerical investigation. Further, a full scale sample of a metaconcrete slab could be fabricated with an array of internal aggregates. The transmission of wave amplitude or energy through a metaconcrete specimen could be measured by testing the specimen with an applied loading over a range of known forcing frequencies. This experimental evaluation of transmission behavior would allow for comparison with the attenuation observed in the numerical calculations so far investigated.

The investigation presented here indicates that metaconcrete is capable of improving performance

under dynamic loading when compared with conventional concrete. The use of metaconcrete provides the potential for the absorption of energy and the mitigation of the high stresses associated with shock and impact loading. The studies presented provide an understanding of the theoretical development and design of metaconcrete for use as an alternative construction material for for blast wave, seismic, impact, and shielding applications.

Appendix A

Neo-Hookean material model

A neo-Hookean material model, extended to the compressible range, is used for all of the numerical meta-concrete slab analyses. The model is described by the following stored strain energy function (Bonet and Wood, 2008):

$$\Psi(\mathbf{C}) = \frac{\lambda}{2} (\ln J)^2 - \mu \ln J + \frac{\mu}{2} (I_1 - 3), \tag{A.1}$$

where $\mathbf{C}$ is the right Cauchy-Green deformation tensor, which can be expressed in terms of the deformation gradient $\mathbf{F}$ as $\mathbf{C} = \mathbf{F}^T \mathbf{F}$, J represents the Jacobian, i.e., $J = \det \mathbf{F}$, I_1 is the first invariant of $\mathbf{C}$, i.e., $I_1 = \operatorname{tr} \mathbf{C}$, and λ and μ are the material coefficients representing the Lamé modulus and shear modulus, respectively. These material coefficients are the familiar material parameters found in linear elastic analyses.

From Eq. A.1 we can derive the following expressions. The first Piola-Kirchhoff stress tensor is given by

$$\mathbf{P} = \frac{\partial \Psi}{\partial J} \frac{\partial J}{\partial \mathbf{F}} + \frac{\partial \Psi}{\partial I_1} \frac{\partial I_1}{\partial \mathbf{F}} = (\lambda \ln J - \mu) \mathbf{F}^{-T} + \mu \mathbf{F}. \tag{A.2}$$

The Kirchhoff stress tensor is

$$\tau = \mathbf{P} \mathbf{F}^T = (\lambda \ln J - \mu) \mathbf{F}^{-T} \mathbf{F}^T + \mu \mathbf{F} \mathbf{F}^T = (\lambda \ln J - \mu) \mathbf{I} + \mu \mathbf{b}, \tag{A.3}$$

where $\mathbf{b} = \mathbf{F} \mathbf{F}^T$ is the left Cauchy-Green tensor. The second Piola–Kirchhoff stress tensor is

$$\mathbf{S} = 2 \frac{\partial \Psi}{\partial I_1} \mathbf{I} + 4 \frac{\partial \Psi}{\partial I_2} \mathbf{C} + 2 J^2 \frac{\partial \Psi}{\partial I_3} \mathbf{C}^{-1} = \mu(\mathbf{I} - \mathbf{C}^{-1}) + \lambda(\ln J) \mathbf{C}^{-1}, \tag{A.4}$$

where $I_2 = \operatorname{tr} \mathbf{C} \mathbf{C}$ and $I_3 = \det \mathbf{C} = J^2$ are the second and third invariants of $\mathbf{C}$, respectively. Finally, the Cauchy stresses can be obtained in terms of the left Cauchy-Green tensor,

$$\sigma = J^{-1} \mathbf{F} \mathbf{S} \mathbf{F}^{-T} = 2 J^{-1} \frac{\partial \Psi}{\partial I_1} \mathbf{b} + 4 J^{-1} \frac{\partial \Psi}{\partial I_2} \mathbf{b}^2 + 2 J \frac{\partial \Psi}{\partial I_3} \mathbf{I} = \frac{\mu}{J} (\mathbf{b} - \mathbf{I}) + \frac{\lambda}{J} (\ln J) \mathbf{I}. \tag{A.5}$$

The compressible neo-Hookean potential used here represents an isotropic hyperelastic material model. When the deformation in the material is small, i.e., in the case of small strains, the standard linear elastic behavior, or Hooke's law, is recovered (Bonet and Wood, 2008). Thus, since we have only small deforma-

tion in our analyses, this material model is used for all the constituents of the metaconcrete slab.

Appendix B

Modeling the blast pressure history
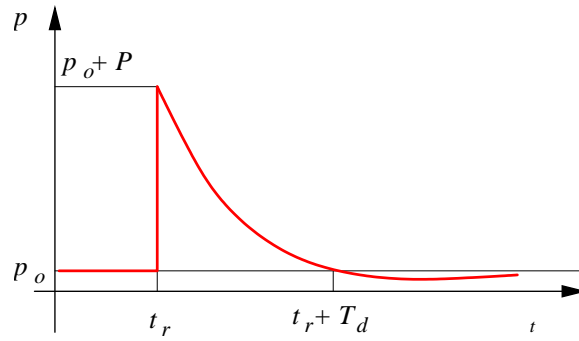
Figure B.1: Typical pressure-time curves for an explosive blast wave.

The blast wave is modeled as follows. An explosion in air of pressure p_0 produces an overpressure $p(t)$ in the surrounding atmosphere. This is called the blast wave. The blast wave is formed when the atmosphere surrounding the explosion is forcibly pushed back, for example, by the gases produced from a conventional chemical explosive. At a fixed, reasonable distance r from the center of the explosion, all overpressure histories due to any blast show a similar configuration, see Figure B.1. In particular, the shock velocities are uniquely related to the overpressure ratios, and thus the peak overpressure uniquely defines the time required for the shock front to travel out to various distances and the decay time to reach the original pressure p_0. It follows that the shock pressure front reaches the position r at time $t = t_r$, where t_r is defined as the arrival time. Thus, the air pressure at the observer's location jumps to the initial overpressure $p_0 + P$. The overpressure immediately begins to decay, following a pressure-time relation described by the following quasi-exponential relation, known as the modified Friedlander equation:

$$p(t) = p_0 + P(1-\tau)\exp(-b\tau) \qquad \tau = \frac{t - t_r}{T_d} \qquad t > t_r, \tag{B.1}$$

where T_d is the duration of the positive overpressure phase and b is a decay parameter. Blast waves of the type shown in Figure B.1 are therefore characterized by three independent parameters, i.e., the initial peak overpressure P, the duration of the blast wave T_d, and the rate of decay of the overpressure, dictated by decay parameter b.

The characteristics of blast waves caused by explosions have been obtained using both experimental and analytical means. Values for the parameters of a blast shock wave generated in a nominal standard atmosphere by a one ton spherical charge of TNT[1] are tabulated in Kinney (1962). To find the description of any explosion using these standardized tables, a simple scaling principle can be applied by considering two similarly proportioned objects, i.e., the ratio of the volume of to two spheres. By geometry, this ratio is proportional to the third power of the ratio of the diameters. Similarly mass and energy, which also vary with volume, can also follow the third power rule. Applying this scaling principle, two explosions in atmosphere can be expected to give identical blast wave intensities at distances which are proportional to the cube root of the respective energy release. That is, to produce a given blast intensity at twice a given distance requires eight times the explosive energy release.

Utilizing the scaling principles described above, we can define the explosive energy release by the yield factor λ,

$$\lambda = \left(\frac{W}{W_{\text{ref}}} \right)^{1/3} ,$$ (B.2)

where W is the energy released by the current explosion in air and W_{ref} is the energy released by the reference explosion. A similar scaled or equivalent distance r_s can be computed using the following scaling law:

$$r_s = \frac{f_d}{\lambda} r ,$$ (B.3)

where r is the actual distance to the shock front, and f_d is the transmission factor for atmospheric density given by

$$f_d = \left(\frac{\rho}{\rho_0} \right)^{1/3} .$$ (B.4)

Using this scaling law, the distance at which a given shock intensity is produced by a reference explosion may be scaled up (or down) to provide a corresponding distance for other explosions. Similarly, a scaled time t_s can be derived:

$$t_s = \frac{f_d f_a}{\lambda} t_r ,$$ (B.5)

where f_a represents the transmission factor for the speed of sound and is given by

$$f_a = \frac{a}{a_{\text{ref}}} .$$ (B.6)

The general procedure for computing the the overpressure $p(t)$ is therefore as follows. Once the location of the ignition point, (x_e, y_e, z_e) has been established, the distance of each surface point to the explosion ignition location can be computed as:

$$r = \sqrt{(x - x_e)^2 + (y - y_e)^2 + (z - z_e)^2} .$$ (B.7)

---

[1] A gram of TNT releases 4200-4602 J upon explosion. This was arbitrarily standardized by setting 1 gram TNT = 4184 J and thus a one tonne TNT reference explosion releases 4.184×10^9 J.

It is also necessary to identify the energy release rate of the explosion W, the air pressure p_0, the sound speed a_0, and the temperature T_0 for the given situation. Once the initial parameters have been established, Eqs. B.2, B.4, and B.6 can be used to compute the yield factor, density transmission factor, and speed of sound transmission factor, respectively. Following this, the scaled distance can be computed using Eq. B.3. These values can then be used to obtain the corresponding overpressure ratio P_r, scaled arrival time t_s, and scaled time duration T_{ds}, by interpolation using Table B.2. The overpressure P can then be computed from

$$P = P_r \, p_0 \tag{B.8}$$

and the characteristic times can be evaluated using

$$t_r = \frac{\lambda}{f_d f_a} t_s \qquad T_d = \frac{\lambda}{f_d f_a} T_{ds} \quad . \tag{B.9}$$

Once the time from explosion ignition equals the arrival time, the Fridlander equation, Eq. B.1, can be used to evaluate the actual pressure value. These computations have been implemented in the finite element code used in the present calculations. Further details and examples of this operative procedure to compute the scaled parameters can be found in Kinney (1962). Alternative explanations of air blast theory and blast scaling can be found in, e.g., Baker (1973).

r	p / p$_0$	t	T$_d$	b	M
[m]		[ms]	[ms]		
1.524	970.000	0.06	14.8	100.0	28.800
3.048	115.000	0.30	14.5	50.0	9.960
4.572	35.000	0.85	14.0	10.0	5.560
6.096	16.000	1.71	13.3	5.0	3.820
7.620	9.400	2.91	12.4	3.3	3.010
9.144	5.800	4.50	11.4	2.4	2.440
10.668	3.900	6.30	10.7	1.8	2.080
12.192	2.800	8.50	10.8	1.5	1.840
13.716	2.100	10.80	11.7	1.2	1.670
15.240	1.650	13.30	12.8	1.1	1.550
16.764	1.350	16.00	14.1	1.0	1.470
18.288	1.130	18.90	15.0	0.9	1.400
19.812	0.960	22.00	15.6	0.9	1.350
21.336	0.830	25.20	16.1	0.9	1.308
22.860	0.730	28.50	16.6	0.9	1.275
24.384	0.650	31.80	17.1	0.9	1.248
25.908	0.580	35.40	17.6	0.9	1.224
27.432	0.520	39.20	18.0	0.9	1.202
28.956	0.470	43.10	18.4	0.9	1.184
30.480	0.430	47.00	18.8	0.9	1.170
32.004	0.400	50.90	19.2	0.9	1.159
33.528	0.370	54.80	19.6	1.0	1.149
35.052	0.350	58.70	19.9	1.0	1.140
36.576	0.330	62.60	20.2	1.0	1.133
38.100	0.310	66.50	20.5	1.0	1.126
39.624	0.292	70.40	20.8	1.0	1.119
41.148	0.275	74.30	21.1	1.0	1.112
42.672	0.259	78.30	21.4	1.0	1.106
44.196	0.244	82.30	21.7	1.1	1.100
45.720	0.230	86.30	22.0	1.1	1.094
47.244	0.218	90.30	22.2	1.1	1.089
48.768	0.208	94.30	22.4	1.1	1.085
50.292	0.200	98.40	22.6	1.1	1.082
51.816	0.192	102.50	22.8	1.1	1.079
53.340	0.185	106.60	23.0	1.1	1.076
54.864	0.178	110.70	23.2	1.1	1.073
56.388	0.171	114.80	23.4	1.2	1.071
57.912	0.164	118.90	23.5	1.2	1.068
59.436	0.157	123.00	23.6	1.2	1.065
60.960	0.151	127.10	23.8	1.2	1.062
62.484	0.146	131.20	23.9	1.2	1.060
64.008	0.141	135.40	24.1	1.2	1.058
65.532	0.136	139.60	24.2	1.2	1.056
67.056	0.131	143.80	24.3	1.3	1.054
68.580	0.127	148.00	24.4	1.3	1.053
70.104	0.123	152.20	24.5	1.3	1.051
71.628	0.120	156.40	24.6	1.3	1.050
73.152	0.116	160.60	24.6	1.4	1.048
74.676	0.113	164.80	24.7	1.4	1.047
76.200	0.110	169.00	24.7	1.4	1.046

Figure B.2: Reference explosion. Point source, yield 1 tonne, standard atmosphere (Kinney, 1962).

Appendix C

Fabrication and testing of metaconcrete

The numerical analyses of metaconcrete behavior presented in the previous chapters indicate that the inclusion of engineered aggregates can enhance the performance of a concrete slab through the absorption of energy within the aggregates and a reduction in the stress present in the mortar matrix. This chapter provides an outline of some of the practical considerations concerning the design and fabrication of metaconcrete and metaconcrete aggregates for use in structures and systems under dynamic loading. We also present a summary of an experimental test that is currently being developed for assessing the energy trapping behavior of metaconcrete.

C.1 Practical design considerations and the fabrication of metaconcrete aggregates

As briefly introduced in Chapter 2, standard concrete is a composite material used in many structural applications. Standard concrete generally consists of two primary constituents; a binding medium, such as a portland cement paste, and an inert filler material or aggregate, which is generally a graded assortment of stone, gravel, and sand fragments (Troxell et al., 1956; Mehta, 1986). The proportions of the principal components are controlled by the need for a workable and placeable wet material, the desire for a hardened mass that possesses the strength and durability required of the purpose, and the cost of the final product (Troxell et al., 1956).

Roughly one–quarter of the concrete volume is filled with cement, water, and air voids. The cement–water paste is the active component of the material, providing strength to the concrete in its final hardened state. Concrete hardens, or 'cures', from a workable mix to a solid structural material through a process called hydration (Troxell et al., 1956; McMillan and Tuthill, 1973). This chemical reaction occurs when water reacts with the hydraulic cement, bonding the components together. Proper curing of regular concrete to design strength therefore requires the surface to be continually moist, and it takes approximately 28 days to fully cure concrete so that the chemical reaction is complete (Troxell et al., 1956).

The other three–quarters of the concrete volume is made up of the aggregate material. The aggregates serve a number of functions including providing a relatively cheap inert filler material, resisting the action of applied loads, and reducing the effect of any volume changes resulting from the hardening process

or changes in the moisture content of the cement-water paste. The properties and material character of the aggregates result in different concrete properties, changing the workability of the freshly mixed material and affecting the strength and durability of the final hardened material. Natural coarse aggregates may consist of gravel or crushed stone; however, other materials can also be used, such as iron blast–furnace slag, fly ash, cinders, burned clay, shale, or other artificial lightweight aggregates (Troxell et al., 1956; Mehta, 1986).

In order to create an effective metconcrete, we therefore need a composite material consisting of meta-concrete aggregates suspended in an matrix material that will act as a binder and that will also have the ability to transmit the applied loading. The matrix material could consist of a mortar-like paste, using a portland cement and water mix combined with a fine sand aggregate.

(a)   (b)
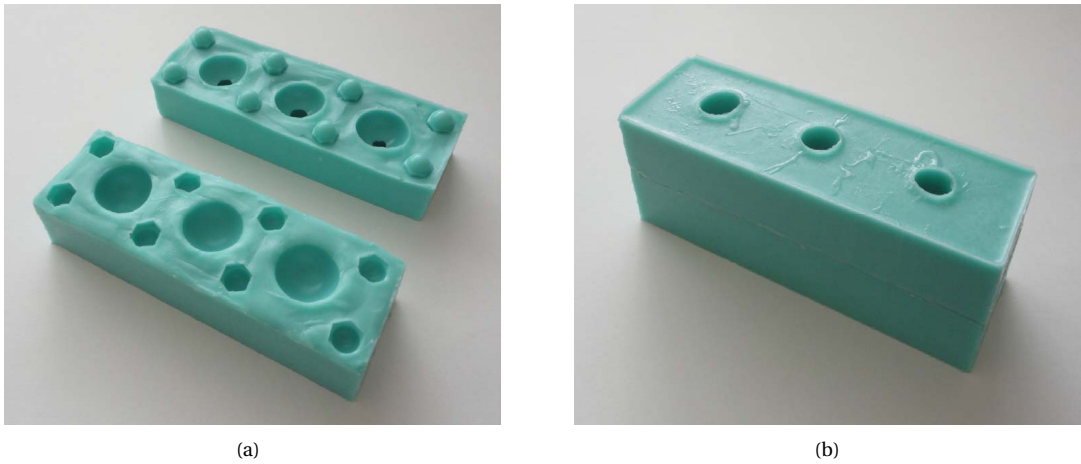
Figure C.1: Mold used to cast three 24 mm diameter aggregates; (a) inside of casting mold, (b) closed mold.

To test the manufacturability of metaconcrete we fabricate prototype metaconcrete aggregates using a casting method. We specifically look at the aggregates investigated in the numerical simulations, and fabricate prototype aggregates with the dimensions given by Configuration C described in Chapter 2. We use a silicone rubber mold made specifically for the purpose, shown in Figure C.1. The flexible mold material allows for easy release of the casted aggregates, maintaining its shape after every use by exhibiting high tear resistance and low long term shrinkage which allows for many repeated castings.

To create the metaconcrete aggregate prototype we use a platinum–cure silicone rubber material for the coating layer, the properties for which are given in Table C.1, layered over a spherical lead core. As indicated by the transmission analyses of Chapter 3, this softer coating will provide a band gap at a lower frequency and is therefore suitable for lower frequency applied loadings. We choose a fast cure translucent rubber, which allows the aggregate to be easily cast in two stages. First a 3 mm deep section of coating

Table C.1: Material properties of the silicone rubber aggregate coating.

Property	Value
Mixed viscosity (cps)	11,000
Specific gravity (g/cm^3)	1.08
Specific volume (m^3/kg)	0.000925
Shore A hardness	20
Tensile strength (MPa)	2.896
100% Modulus (MPa)	0.324
Elongation at break (%)	470

material is poured into the mold. This is allowed to cure until it can suspend the weight of the core, after which the spherical core is placed in the center of the mold, the mold is closed, and the rest of the coating is cast. This method creates an aggregate with a 3 mm silicone rubber coating covering a 18 mm diameter lead sphere. The cast aggregate along with a cross section are shown in Figure C.2.

(a)   (b)
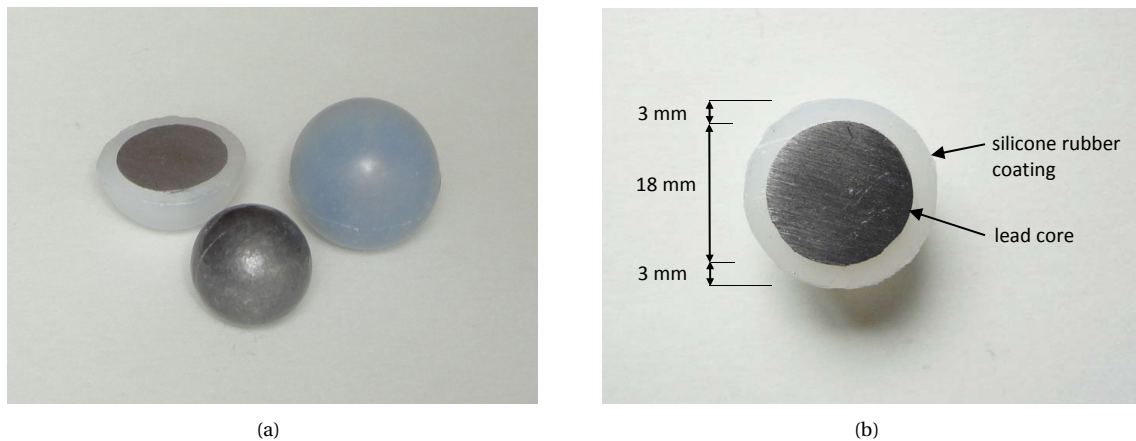
Figure C.2: Metaconcrete aggregate of configuration type C with a silicone rubber compliant coating: (a) cast aggregate shown alongside a lead core and an aggregate that has been cut in half, (b) cross section of an aggregate showing the dimensions of the core and coating.

The numerical simulations considered metaconcrete slabs with 27-50% aggregates by volume. This equates to between 37,000-69,500 24 mm diameter aggregates per cubic meter of metaconcrete material. To cast metaconcrete for construction purposes, and to generate the energy absorption properties desired, a very large number of aggregates would therefore be required. The casting method proposed here could be used, or adapted, to manufacture the high volume of aggregates necessary with relative ease. It would be possible to create molds for casting a larger number of aggregates and also to alter the mold so that the aggregates could be cast in a single step. Specific molds could also be made to cast aggregates of different sizes and coating materials, based on the required properties of the aggregate as recommended

by a tuning assessment.

In the numerical simulations, a periodic array of aggregates was used to test the properties and performance of metaconcrete. In the practical implementation of metaconcrete, a similar periodic structure could be created using a grid or truss stucture to suspend the aggregates in the correct arrangement so that the mortar can be poured around them. Alternatively, the aggregates could simply be mixed into the mortar in the same way as the stone and gravel aggregates of regular concrete. A periodic arrangement of aggregates in this case would not be possible, however, manufacturing metaconcrete in this way would allow it to be mixed and poured as an alternative to standard concrete for the specific case where resistance to dynamic excitation or impact is also required. In fact, in the study of acoustic crystals with locally resonant inclusions, Mei et al. (2013) suggested that the periodicity of resonant inclusions may not effect the band gap behavior and transmission attenuation properties of the material. It is therefore possible that an exactly periodic array of aggregates is not necessary to achieve the favorable behavior seen in the numerical simulations of metaconcrete slabs. Although non–periodic arrangements of metaconcrete aggregates have not yet been studied, this is certainly an area of future investigation that will aid in the practical implementation of metaconcrete for construction.

A metaconcrete material consisting of the cast aggregates described above mixed into a sand–cement paste could be poured and cast for use in many impact and blast protection applications. The wall panels discussed in Chapter 1 utilized either standard or fiber reinforced concrete to absorb energy and reduce the effect of blast loading. Metaconcrete could provide an alternative to these materials. Being specifically designed to absorb energy and reduce mortar stress, metaconcrete would greatly enhance the performance of a blast or impact shielding panel. Metaconcrete could be poured or cast into a standard wall panel, or it could replace the fiber reinforced layer used in a layered composite panel, such as those proposed by Christian and Chye (2014). It may also be possible to use metaconcrete as a grout for the infill of masonry walls that could be utilized in shielding or blast protection structures. Another possibility would be to use a fiber reinforced cement matrix with the metacocncrete aggregates, thus combining the advantageous properties of both materials.

Since it is possible for metaconcrete to be cast in place, it would also be viable to use metaconcrete in combination with steel reinforced concrete sections. This would allow metaconcrete to be used for structural purposes with the additional ability to provide protection from dynamic loading. In this case, the size of the aggregate would need to be designed so that it is smaller than, and does not interfere with, the reinforcing spacing.

Another important consideration is the amount of fracture and spalling of the concrete surface allowed for the particular application being considered. Flying concrete fragments pose a significant safety risk to building occupants and facilities. In the analysis of fracture behavior in Chapter 5 when lower explosion yields are used the damage in the metaconcrete slab is limited to the volume near the front exposed face and the aggregate are able and slow the propagation of the stress wave. This therefore im-

plies that even with damage around the front section of the slab, the aggregates still perform well and can absorb a significant fraction of the mechanical energy. Thus, for the practical implementation of meta-concrete, it would be possible to use a protective coating on the front surface of the slab for larger yield events. This would prevent excessive spalling and any catastrophic damage to the exterior of the slab, enabling the metaconcrete section to maintain its structure while still performing its energy absorbing function. This light protective barrier could be a carbon fiber reinforced polymer layer or a polyurethane coating such as those discussed in Malvar et al. (2007), or a glass fiber reinforced coating such as those successfully used by Garfield et al. (2011) in the investigation of wall panels under blast loading.

Other practical design considerations should also be evaluated before any large–scale manufacturing of metaconcrete. The use of lead for the heavy core material poses a pollution issue, and may not be suitable for certain applications. Other materials with high density or metal alternatives may be appropriate. In some cases, it may also be necessary to consider the use of a protective casing for the aggregate, e.g., steel or plastic, that will prevent any degradation of the coating or shape change of the aggregate when mixed, poured, and stressed under self-weight or static loading conditions. The durability, compressive strength, static properties, and the level of adhesion between the aggregates and the matrix are other factors that should also be considered.

C.2   A non–destructive experimental test

Metaconcrete has been shown to provide a beneficial transfer of energy and a reduction in mortar stress when subjected to a blast wave profile in the elastic regime. In order to verify the energy trapping observed in the numerical simulations, we design a simple experiment to non–destructively test a metaconcrete specimen. The experiment intends to activate resonance and the energy trapping properties of the meta-concrete aggregates by generating a loading between a striker bar and a metaconcrete specimen. The geometry and elastic modulus of the coating material determine the resonant frequency of the aggregate and thus the theoretical required wave frequency for energy absorption.

The experiment consists of a striker bar impacting on a cylindrical metaconcrete specimen. The specimen is initially at rest and the system uses the pendulum arrangement shown in Figure C.3. The striker bar is raised to a height h_1 and then released from stationary so that it reaches the specimen with a velocity v_1^-, where the superscript indicates velocity before impact. The specimen then swings to a maximum height h_2 and the striker to a height h_3, both of which are measured using a video camera. Therefore, the known quantities are the mass of the striker and the specimen, m_1 and m_2, respectively, and the experimentally measured heights h_1, h_2, and h_3. From this information, we compute the amount of energy absorbed by the metaconcrete aggregates E_a, along with the efficiency of the metaconcrete sample, which is based on a comparison of this result with the total input energy. Using an energy balance, the energy
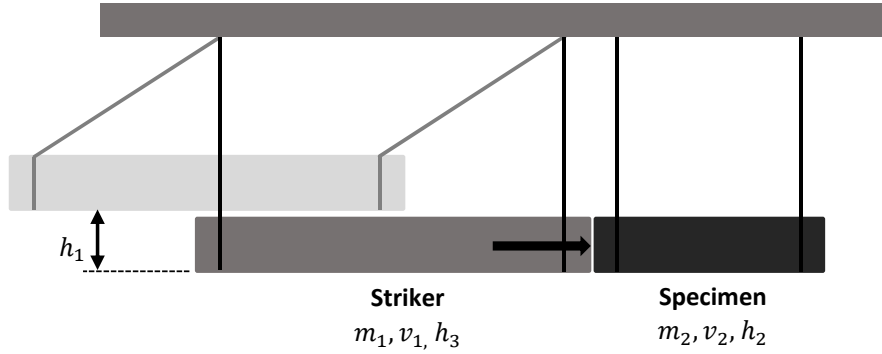
Figure C.3: Impact test pendulum experiment showing the striker bar, released from height h_1, impacting the specimen.

absorbed by the metaconcrete aggregates is given by

$$E_a = m_1 g(h_1 - h_3) - m_2 g h_2. \tag{C.1}$$

The efficiency can be expressed as the fraction of the supplied energy that is trapped within the metaconcrete aggregates. The supplied energy is given by the total potential energy of the striker before release, thus the efficiency is

$$\text{Efficiency} = \frac{E_a}{g h_1 m_1}. \tag{C.2}$$

We can therefore compare the efficiency of a metaconcrete specimen to that of a regular mortar specimen by completing identical tests on the two samples. Any difference between the two results can be attributed to the presence of resonant aggregates within the metaconcrete specimen and this will allow us to approximate the amount of energy trapped by the metaconcrete aggregates.

A metaconcrete sample can be cast by arranging the aggregates shown in Figure C.2 in a cement–sand paste that forms the mortar matrix. A sample excluding the aggregates can also be cast and used as a comparison. For the particular experiment shown in Figure C.3 we use a 4"x6" standard concrete testing cylinder to create both mortar and metaconcrete specimens. An example of a cast specimen is shown in Figure C.4.

The experimental arrangement displaying the hanging test specimen and the striker bar in the release position is shown in Figure C.5. The release mechanism for the striker bar is designed so that consistent release heights can be obtained. A small diameter rope with a very low static elongation ratio is used to suspend the striker bar. The rope is set at a fixed length so that the same release height can be achieved on repeated runs. The rope is suspended from a pin which is quickly removed to initiate release and thus the beginning of the experimental run. In this particular experiment a PVC striker bar was used to impact the

Figure C.4: An example of a 4"x6" cylindrical test specimen.

specimen, with a length specified by the resonant frequency of the aggregate configuration considered.
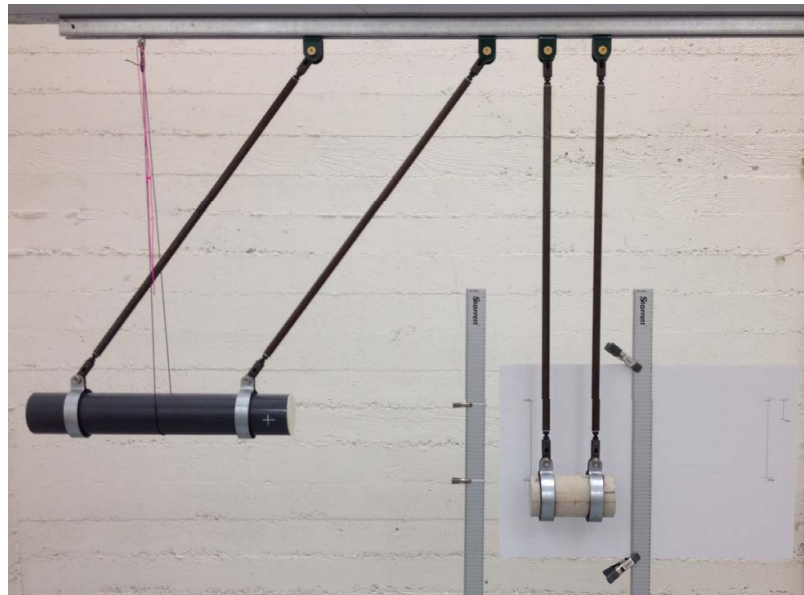
Figure C.5: The experimental setup showing the release position of the striker bar and the rope and pin mechanism.

Still images from test runs of the experiment are shown in Figure C.6. Figure C.6(a) shows that initially at–rest test confgiuration and Figure C.6(b) shows the maximum swing height after impact for a striker release height of 30 cm. Heights are measured from the images by finding the distance between the marked points on the specimen or striker at both the rest position and maximum height after impact, using a
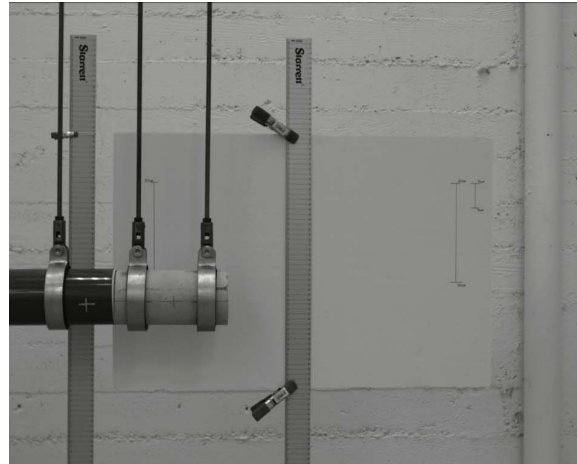
(a)
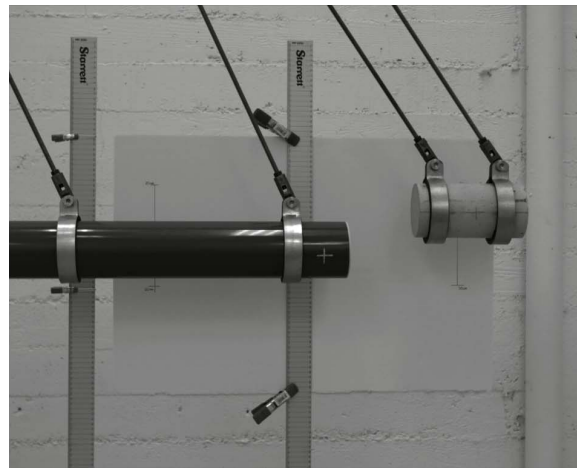
(b)

Figure C.6: Still images captured from an experiment test run using a metaconcrete specimen and a striker bar with a release height of 30 cm: (a) initial at–rest configuration, (b) maximum specimen height after impact.

calibration ratio along with the number of image pixels to compute vertical heights in centimeters.

Work on this experimental program is currently ongoing and it is hoped that further investigation will lead to a greater depth of understanding which will aid in the design and practical implementation of metaconcrete systems.

Bibliography

Abaqus/Standard 6.12-2. Dassault Systémes Simulia Corp, Providence, RI, 2012.

L. Ambrosio and V. M. Tortorelli. On the approximation of free discontinuity problems. *Bollettino dell'Unione Matematica Italiana B*, 7:105–123, 1992.

American Concrete Institute. *ACI Education Bulletin E1-07, Aggregates for Concrete*. Developed by ACI Committee E-701. American Concrete Institute, Farmington Hills, MI, 2007.

A. Andreone, A. Cusano, A. Cutolo, and V. Galdi. *Selected topics in photonic crystals and metamaterials*. World Scientific, Singapore, 2011.

W. E. Baker. *Explosions in Air*. University of Texas Press, Austin, 1973.

B. Banerjee. *An introduction to metamaterials and waves in composites*. CRC Press, Taylor & Francis Group, Boca Raton, 2011.

J. P. Barrett and S. A. Cummer. Roadmap to electrically self-tuning metamaterials: Design and experimental validation. In *2014 International Conference on Electromagnetics in Advanced Applications (ICEAA)*, pages 341–342, 2014.

T. Belytschko and J. I. Lin. A three-dimensional impact-penetration algorithm with erosion. *Computers & Structures*, 25(1):95–104, 1987.

J. Bonet and R. D. Wood. *Nonlinear Continuum Mechanics for Finite Element Analysis*. Cambridge University Press, New York, 2nd edition, 2008.

T. Børvik, O. S. Hopperstad, and K. O. Pedersen. Quasi-brittle fracture during structural impact of AA7075-T651 aluminium plates. *International Journal of Impact Engineering*, 37(5):537–551, 2010.

B. Bourdin, G. A. Francfort, and J. J. Marigo. Numerical experiments in revisited brittle fracture. *Journal of the Mechanics and Physics of Solids*, 48(4):797–826, 2000.

A. Braides and G. Dal Maso. Non-local approximation of the mumford-shah functional. *Calculus of Variations and Partial Differential Equations*, 5(4):293–322, 1997.

S. Brûlé, E. H. Javelaud, S. Enoch, and S. Guenneau. Experiments on seismic metamaterials: Molding surface waves. *Physical Review Letters*, 112(13):133901, 2014.

D. Caballero, J. Sánchez-Dehesa, C. Rubio, R. Mártinez-Sala, J. V. Sánchez-Pérez, F. Meseguer, and J. Llinares. Large two-dimensional sonic band gaps. *Physical Review E*, 60(6):R6316–R6319, 1999.

F. Cervera, L. Sanchis, R. Martínez-Sala, C. Rubio, F. Meseguer, C. López, D. Caballero, and J. Sánchez-Dehesa. Refractive acoustic devices for airborne sound. *Physical Review Letters*, 88(2):023902, 2002.

A. Cho. Voilà! cloak of invisibility unveiled. *Science*, 314(5798):403–403, 2006.

A. Christian and G. O. K. Chye. Performance of fiber reinforced high-strength concrete with steel sandwich composite system as blast mitigation panel. *Procedia Engineering*, 95(0):150–157, 2014.

G. Colonnetti. Su certi stati di coazione elastica che non dipendono da azioni esterne. *Rendiconti della R. Accademia dei Lincei, Giugno*, pages 43–47, 1917.

R. V. Craster and S. Guenneau. *Acoustic Metamaterials: Negative Refraction, Imaging, Lensing, and Cloaking*. Springer Series in Materials Science. Springer Netherlands, Dordrecht, 2013.

M. Dubois, M. Farhat, E. Bossy, S. Enoch, S. Guenneau, and P. Sebbah. Flat lens for pulse focusing of elastic waves in thin plates. *Applied Physics Letters*, 103(7):071915, 2013.

E. N. Economou and M. Sigalas. *Spectral gaps for classical waves in periodic structures*. Photonic Band Gaps and Localization, ed. by C. M. Soukoulis. Springer, New York, 1993.

E. N. Economou and M. Sigalas. Stop bands for elastic waves in periodic composite materials. *The Journal of the Acoustical Society of America*, 95(4):1734–1740, 1994.

M. Farhat, S. Enoch, S. Guenneau, and A. B. Movchan. Broadband cylindrical acoustic cloak for linear surface waves in a fluid. *Physical Review Letters*, 101(13):134501, 2008.

M. Farhat, S. Guenneau, and S. Enoch. Ultrabroadband elastic cloaking in thin plates. *Physical Review Letters*, 103(2):024301, 2009.

M. Farhat, S. Guenneau, and S. Enoch. Broadband cloaking of bending waves via homogenization of multiply perforated radially symmetric and isotropic thin elastic plates. *Physical Review B*, 85(2):020301, 2012.

S. Foteinopoulou, E. N. Economou, and C. M. Soukoulis. Refraction in media with a negative refractive index. *Physical Review Letters*, 90(10):107402, 2003.

G. A. Francfort and J.-J. Marigo. Revisiting brittle fracture as an energy minimization problem. *Journal of the Mechanics and Physics of Solids*, 46:1319–1342, 1998.

T. T. Garfield, W. D. Richins, T. K. Larson, C. P. Pantelides, and J. E. Blakeley. Performance of RC and FRC wall panels reinforced with mild steel and GFRP composites in blast events. *Procedia Engineering*, 10 (0):3534–3539, 2011.

M. Gharghi, C. Gladden, T. Zentgraf, Y. Liu, X. Yin, J. Valentine, and X. Zhang. A carpet cloak for visible light. *Nano Letters*, 11(7):2825–2828, 2011.

C. Goffaux and J. Sánchez-Dehesa. Two-dimensional phononic crystals studied using a variational method: Application to lattices of locally resonant materials. *Physical Review B*, 67(14):144301, 2003.

C. Goffaux and J. P. Vigneron. Theoretical study of a tunable phononic band gap system. *Physical Review B*, 64(7):075118, 2001.

C. Goffaux, J. Sánchez-Dehesa, A. L. Yeyati, P. Lambin, A. Khelif, J. O. Vasseur, and B. Djafari-Rouhani. Evidence of fano-like interference phenomena in locally resonant materials. *Physical Review Letters*, 88 (22):225502, 2002.

A. A. Griffith. The phenomena of rupture and flow in solids. *Philosophical Transactions of the Royal Society of London. Series A*, 221:163–198, 1921.

S. Guenneau, C. Amra, and D. Veynante. Transformation thermodynamics: cloaking and concentrating heat flux. *Optics Express*, 20(7):8207–8218, 2012.

E. Hecht. *Optics*. Addison-Wesley, Reading, MA, 4th edition, 2002.

M. Hirsekorn. Small-size sonic crystals with strong attenuation bands in the audible frequency range. *Applied Physics Letters*, 84(17):3364–3366, 2004.

K. M. Ho, C. T. Chan, and C. M. Soukoulis. Existence of a photonic gap in periodic dielectric structures. *Physical Review Letters*, 65(25):3152–3155, 1990.

K. M. Ho, C. T. Chan, C. M. Soukoulis, R. Biswas, and M. Sigalas. Photonic band gaps in three dimensions: New layer-by-layer periodic structures. *Solid State Communications*, 89(5):413–416, 1994.

H. H. Huang and C. T. Sun. Wave attenuation mechanism in an acoustic metamaterial with negative effective mass density. *New Journal of Physics*, 11(1):013003, 2009.

H. H. Huang, C. T. Sun, and G. L. Huang. On the negative effective mass density in acoustic metamaterials. *International Journal of Engineering Science*, 47(4):610–617, 2009.

J. S. Jensen. Phononic band gaps and vibrations in one- and two-dimensional mass-spring structures. *Journal of Sound and Vibration*, 266(5):1053–1078, 2003.

J. D. Joannopoulos, S. G. Johnson, J. N. Winn, and R. D. Meade. *Photonic crystals: molding the flow of light*. Princeton University Press, Princeton, 2nd edition, 2008.

S. John. Strong localization of photons in certain disordered dielectric superlattices. *Physical Review Letters*, 58(23):2486–2489, 1987.

G. R. Johnson and R. A. Stryk. Eroding interface and improved tetrahedral element algorithms for high-velocity impact computations in three dimensions. *International journal of impact engineering*, 5(1):411–421, 1987.

S. G. Johnson and J. D. Joannopoulos. Three-dimensionally periodic dielectric layered structure with omnidirectional photonic band gap. *Applied Physics Letters*, 77:3490, 2000.

M. Kafesaki and E. N. Economou. Interpretation of the band-structure results for elastic and acoustic waves by analogy with the lcao approac. *Physical Review B*, 52(18):13317–13331, 1995.

M. Kafesaki and E. N. Economou. Multiple-scattering theory for three-dimensional periodic acoustic composites. *Physical Review B*, 60(17):11993–12001, 1999.

M. Kafesaki, M. M. Sigalas, and E. N. Economou. Elastic wave band gaps in 3-d periodic polymer matrix composites. *Solid State Communications*, 96(5):285–289, 1995.

M. Kafesaki, R. S. Penciu, and E. N. Economou. Air bubbles in water: a strongly multiple scattering medium for acoustic waves. *Physical Review Letters*, 84(26):6050–6053, 2000a.

M. Kafesaki, M. M. Sigalas, and N. García. Frequency modulation in the transmittivity of wave guides in elastic-wave band-gap materials. *Physical Review Letters*, 85(19):4044–4047, 2000b.

G. F. Kinney. *Explosive Shocks in Air*. The MacMillan Company, New York, 1962.

A. D. Klironomos and E. N. Economou. Elastic wave band gaps and single scattering. *Solid State Communications*, 105(5):327–332, 1998.

T. Krauthammer. *Modern Protective Structures*. CRC Press, Boca Raton, FL, 2008.

N. Kundtz and D. R. Smith. Extreme-angle broadband metamaterial lens. *Nature Materials*, 9(2):129–132, 2010.

M. S. Kushwaha, P. Halevi, L. Dobrzynski, and B. Djafari-Rouhani. Acoustic band structure of periodic elastic composites. *Physical Review Letters*, 71(13):2022–2025, 1993.

M. S. Kushwaha, P. Halevi, G. Martĩņnez, L. Dobrzynski, and B. Djafari-Rouhani. Theory of acoustic band structure of periodic elastic composites. *Physical Review B*, 49(4):2313–2322, 1994.

N. Landy and D. R. Smith. A full-parameter unidirectional metamaterial cloak for microwaves. *Nat Mater*, 12(1):25–28, 2013.

U. Leonhardt. Optical conformal mapping. *Science*, 312(5781):1777–1780, 2006.

B. Li, A. Pandolfi, and M. Ortiz. Material-point erosion simulation of dynamic fragmentation of metals. *Mechanics of Materials*, 80, Part B:288–297, 2015.

S. Y. Lin, J. G. Fleming, D. L. Hetherington, B. K. Smith, R. Biswas, K. M. Ho, M. M. Sigalas, W. Zubrzycki, S. R. Kurtz, and J. Bur. A three-dimensional photonic crystal operating at infrared wavelengths. *Nature*, 394(6690):251–253, 1998.

A. P. Liu, R. Zhu, X. N. Liu, G. K. Hu, and G. L. Huang. Multi-displacement microstructure continuum modeling of anisotropic elastic metamaterials. *Wave Motion*, 49(3):411–426, 2012.

X. N. Liu, G. K. Hu, G. L. Huang, and C. T. Sun. An elastic metamaterial with simultaneously negative mass density and bulk modulus. *Applied Physics Letters*, 98(25):251907, 2011.

Z. Liu, C. T. Chan, P. Sheng, A. L. Goertzen, and J. H. Page. Elastic wave scattering by periodic structures of spherical objects: Theory and experiment. *Physical Review B*, 62(4):2446–2457, 2000a.

Z. Liu, X. Zhang, Y. Mao, Y. Y. Zhu, Z. Yang, C. T. Chan, and P. Sheng. Locally resonant sonic materials. *Science*, 289(5485):1734–1736, 2000b.

Z. Liu, C. T. Chan, and P. Sheng. Three-component elastic wave band-gap material. *Physical Review B*, 65 (16):165116, 2002.

Z. Liu, C. T. Chan, and P. Sheng. Analytic model of phononic crystals with local resonances. *Physical Review B*, 71(1):014103, 2005.

C. Luo, S. G. Johnson, J. D. Joannopoulos, and J. B. Pendry. All-angle negative refraction without negative effective index. *Physical Review B*, 65(20):201104, 2002.

C. Luo, S. G. Johnson, J. D. Joannopoulos, and J. B. Pendry. Subwavelength imaging in photonic crystals. *Physical Review B*, 68(4):045115, 2003.

L. Malvar, J. Crawford, and K. Morrill. Use of composites to resist blast. *Journal of Composites for Construction*, 11(6):601–610, 2007.

L. Mao, S. Barnett, D. Begg, G. Schleyer, and G. Wight. Numerical simulation of ultra high performance fibre reinforced concrete panel subjected to blast loading. *International Journal of Impact Engineering*, 64(0):91–100, 2014.

R. Mártinez-Sala, J. Sancho, J. V. Sánchez, V. Gómez, J. Llinares, and F. Meseguer. Sound attenuation by sculpture. *Nature*, 378:241, 1995.

S. L. McCall, P. M. Platzman, R. Dalichaouch, D. Smith, and S. Schultz. Microwave propagation in two-dimensional dielectric lattices. *Physical Review Letters*, 67(15):2017–2020, 1991.

F. R. McMillan and L. H. Tuthill. *Concrete primer*. American Concrete Institute, Detroit, 1973.

P. K. Mehta. *Concrete: structure, properties, and materials*. Prentice-Hall, New Jersey, 1986.

J. Mei, Z. Liu, W. Wen, and P. Sheng. Effective mass density of fluid-solid composites. *Physical Review Letters*, 96(2):024301, 2006.

J. Mei, G. Ma, M. Yang, J. Yang, and P. Sheng. *Dynamic Mass Density and Acoustic Metamaterials*, volume 173 of *Springer Series in Solid-State Sciences*, book section 5, pages 159–199. Springer Berlin Heidelberg, 2013.

G. W. Milton. New metamaterials with macroscopic behavior outside that of continuum elastodynamics. *New Journal of Physics*, 9(10):359, 2007.

G. W. Milton and J. R. Willis. On modifications of newton's second law and linear continuum elastodynamics. *Proceedings of the Royal Society A*, 463(2079):855–880, 2007.

G. W. Milton, M. Briane, and J. R. Willis. On cloaking for elasticity and physical equations with a transformation invariant form. *New Journal of Physics*, 8(10):248, 2006.

T. Miyashita. Sonic crystals and sonic wave-guides. *Measurement Science and Technology*, 16(5):R47, 2005.

F. R. Montero de Espinosa, E. Jiménez, and M. Torres. Ultrasonic band gap in a periodic two-dimensional composite. *Physical Review Letters*, 80(6):1208–1211, 1998.

C. Naito, R. Dinan, and B. Bewick. Use of precast concrete walls for blast protection of steel stud construction. *Journal of Performance of Constructed Facilities*, 25(5):454–463, 2011.

M. Negri. A finite element approximation of the griffithâĂŹs model in fracture mechanics. *Numerische Mathematik*, 95(4):653–687, 2003.

M. Negri. A non-local approximation of free discontinuity problems in sbv and sbd. *Calculus of Variations and Partial Differential Equations*, 25(1):33–62, 2006.

A. Norris and F. A. Amirkulova. Active elastodynamic cloaking. *Mathematics and Mechanics of Solids*, 19 (6):603–625, 2014.

A. Norris, F. A. Amirkulova, and W. J. Parnell. Source amplitudes for active exterior cloaking. *Inverse Problems*, 28(10):105002, 2012.

M. Ortiz and A. E. Giannakopoulos. Crack propagation in monolithic ceramics under mixed mode loading. *International Journal of Fracture*, 44(4):233–258, 1990.

A. Pandolfi and M. Ortiz. An eigenerosion approach to brittle fracture. *International Journal for Numerical Methods in Engineering*, 92:694–714, 2012.

A. Pandolfi, B. Li, and M. Ortiz. Modeling fracture by material-point erosion. *International Journal of Fracture*, 184(1/2):3–16, 2013.

C. P. Pantelides, T. T. Garfield, W. D. Richins, T. K. Larson, and J. E. Blakeley. Reinforced concrete and fiber reinforced concrete panels subjected to blast detonations and post-blast static tests. *Engineering Structures*, 76(0):24–33, 2014.

J. B. Pendry. Negative refraction makes a perfect lens. *Physical Review Letters*, 85(18):3966–3969, 2000.

J. B. Pendry. Metamaterials and the control of electromagnetic fields. In *Conference on Coherence and Quantum Optics*, OSA Technical Digest (CD), page CMB2. Optical Society of America, 2007.

J. B. Pendry, A. J. Holden, D. J. Robbins, and W. J. Stewart. Magnetism from conductors and enhanced nonlinear phenomena. *Microwave Theory and Techniques, IEEE Transactions on*, 47(11):2075–2084, 1999.

J. B. Pendry, D. Schurig, and D. R. Smith. Controlling electromagnetic fields. *Science*, 312(5781):1780–1782, 2006.

M. Plihal and A. A. Maradudin. Photonic band structure of two-dimensional systems: The triangular lattice. *Physical Review B*, 44(16):8565–8571, 1991.

B.-I. Popa and S. A. Cummer. Non-reciprocal and highly nonlinear active acoustic metamaterials. *Nat Commun*, 5, 2014.

J. V. Sánchez-Pérez, D. Caballero, R. Mártinez-Sala, C. Rubio, J. Sánchez-Dehesa, F. Meseguer, J. Llinares, and F. Gálvez. Sound attenuation by a two-dimensional array of rigid cylinders. *Physical Review Letters*, 80(24):5325–5328, 1998.

R. Schittny, M. Kadic, S. Guenneau, and M. Wegener. Experiments on transformation thermodynamics: Molding the flow of heat. *Physical Review Letters*, 110(19):195901, 2013.

B. Schmidt, F. Fraternali, and M. Ortiz. Eigenfracture: an eigendeformation approach to variational fracture. *SIAM Multiscale Modeling and Simulation*, 7:1237–1266, 2009.

D. Schurig, J. J. Mock, B. J. Justice, S. A. Cummer, J. B. Pendry, A. F. Starr, and D. R. Smith. Metamaterial electromagnetic cloak at microwave frequencies. *Science*, 314(5801):977–980, 2006.

R. A. Shelby, D. R. Smith, S. C. Nemat-Nasser, and S. Schultz. Microwave transmission through a two-dimensional, isotropic, left-handed metamaterial. *Applied Physics Letters*, 78(4):489–491, 2001a.

R. A. Shelby, D. R. Smith, and S. Schultz. Experimental verification of a negative index of refraction. *Science*, 292(5514):77–79, 2001b.

P. Sheng, X. X. Zhang, Z. Liu, and C. T. Chan. Locally resonant sonic materials. *Physica B: Condensed Matter*, 338(1-4):201–205, 2003.

P. Sheng, J. Mei, Z. Liu, and W. Wen. Dynamic mass density and acoustic metamaterials. *Physica B: Condensed Matter*, 394(2):256–261, 2007.

M. Sigalas and E. N. Economou. Band structure of elastic waves in two dimensional systems. *Solid State Communications*, 86(3):141–143, 1993.

M. Sigalas, C. M. Soukoulis, E. N. Economou, C. T. Chan, and K. M. Ho. Photonic band gaps and defects in two dimensions: Studies of the transmission coefficient. *Physical Review B*, 48(19):14121–14126, 1993.

M. M. Sigalas and E. N. Economou. Elastic and acoustic wave band structure. *Journal of Sound and Vibration*, 158(2):377–382, 1992.

M. M. Sigalas and N. García. Theoretical study of three dimensional elastic band gaps with the finite-difference time-domain method. *Journal of Applied Physics*, 87(6):3122–3125, 2000.

M. M. Sigalas, E. N. Economou, and M. Kafesaki. Spectral gaps for electromagnetic and scalar waves: Possible explanation for certain differences. *Physical Review B*, 50(5):3393–3396, 1994.

D. R. Smith, S. L. McCall, P. M. Platzman, R. Dalichaouch, N. Kroll, and S. Schultz. Photonic band structure and defects in one and two dimensions. *Journal of the Optical Society of America B*, 10(2):314–321, 1993.

D. R. Smith, S. Schultz, N. Kroll, M. Sigalas, K. M. Ho, and C. M. Soukoulis. Experimental and theoretical results for a twoâĂŘdimensional metal photonic bandâĂŘgap cavity. *Applied Physics Letters*, 65(5):645–647, 1994.

D. R. Smith, W. J. Padilla, D. C. Vier, S. C. Nemat-Nasser, and S. Schultz. Composite medium with simultaneously negative permeability and permittivity. *Physical Review Letters*, 84(18):4184–4187, 2000.

C. M. Soukoulis and M. Wegener. Past achievements and future challenges in the development of three-dimensional photonic metamaterials. *Nat Photon*, 5(9):523–530, 2011.

H. S. Sözüer and J. P. Dowling. Photonic band calculations for woodpile structures. *Journal of Modern Optics*, 41(2):231–239, 1994.

H. S. Sözüer, J. W. Haus, and R. Inguva. Photonic bands: Convergence problems with the plane-wave method. *Physical Review B*, 45(24):13962–13972, 1992.

N. Stenger, M. Wilhelm, and M. Wegener. Experiments on elastic cloaking in thin plates. *Physical Review Letters*, 108(1):014301, 2012.

Y. Tanaka, Y. Tomoyasu, and S.-i. Tamura. Band structure of acoustic waves in phononic lattices: Two-dimensional composites with large acoustic mismatch. *Physical Review B*, 62(11):7387–7392, 2000.

M. Torres, F. R. Montero de Espinosa, and J. L. Aragón. Ultrasonic wedges for elastic wave bending and splitting without requiring a full band gap. *Physical Review Letters*, 86(19):4282–4285, 2001.

G. E. Troxell, H. E. Davis, and J. W. Kelly. *Composition and properties of concrete*. McGraw-Hill, New York, 1956.

J. O. Vasseur, P. A. Deymier, G. Frantziskonis, G. Hong, B. Djafari-Rouhani, and L. Dobrzynski. Experimental evidence for the existence of absolute acoustic band gaps in two-dimensional periodic composite media. *Journal of Physics: Condensed Matter*, 10(27):6051, 1998.

J. O. Vasseur, P. A. Deymier, B. Chenni, B. Djafari-Rouhani, L. Dobrzynski, and D. Prevost. Experimental and theoretical evidence for the existence of absolute acoustic band gaps in two-dimensional solid phononic crystals. *Physical Review Letters*, 86(14):3012–3015, 2001.

V. G. Veselago. The electrodynamics of substances with simultaneously negative values of ϵ and μ. *Soviet Physics Uspekhi*, 10(4):509, 1968.

P. R. Villeneuve and M. Piché. Photonic band gaps in two-dimensional square and hexagonal lattices. *Physical Review B*, 46(8):4969–4972, 1992.

R. M. Walser. Metamaterials: What are they? what are they good for? *Bulletin of the American Physical Society*, 45:1005, 2000.

G. Wang, J. Wen, Y. Liu, and X. Wen. Lumped-mass method for the study of band structure in two-dimensional phononic crystals. *Physical Review B*, 69(18):184302, 2004a.

G. Wang, X. Wen, J. Wen, L. Shao, and Y. Liu. Two-dimensional locally resonant phononic crystals with binary structures. *Physical Review Letters*, 93(15):154302, 2004b.

G. Wang, X. Wen, J. Wen, and Y. Liu. Quasi-one-dimensional periodic structure with locally resonant band gaps. *Journal of Applied Mechanics*, 73(1):167–170, 2006.

M. Wegener. Metamaterials beyond optics. *Science*, 342(6161):939–940, 2013.

Y. Xiao, J. Wen, and X. Wen. Longitudinal wave band gaps in metamaterial-based elastic rods containing multi-degree-of-freedom resonators. *New Journal of Physics*, 14(3):033042, 2012.

E. Yablonovitch. Inhibited spontaneous emission in solid-state physics and electronics. *Physical Review Letters*, 58(20):2059–2062, 1987.

E. Yablonovitch, T. J. Gmitter, and K. M. Leung. Photonic band structure: The face-centered-cubic case employing nonspherical atoms. *Physical Review Letters*, 67(17):2295–2298, 1991.

Y. Yao, X. Zhou, and G. Hu. Experimental study on negative effective mass in a 1D mass-spring system. *New Journal of Physics*, 10(4):043020, 2008.

P. Yeh. *Optical waves in layered media*. Wiley, Hoboken, NJ, 2005.

Y. Yuan, B.-I. Popa, and S. A. Cummer. Zero loss magnetic metamaterials using powered active unit cells. *Optics Express*, 17(18):16135–16143, 2009.

R. Zhu, H. H. Huang, G. L. Huang, and C. T. Sun. Microstructure continuum modeling of an elastic meta-material. *International Journal of Engineering Science*, 49(12):1477–1485, 2011.